The Aharonov–Bohm effect and resonant scattering in graphene

**Dissertation zur Erlangung des
naturwissenschaftlichen Doktorgrades der
Bayerischen Julius-Maximilians-Universität Würzburg**

vorgelegt von

Jörg Alexander Jürgen Schelter

aus Fürth

Würzburg 2012

Eingereicht am: ....

bei der Fakultät für Physik und Astronomie

1. Gutachter: ....

2. Gutachter: ....

3. Gutachter: ....

der Dissertation

1. Prüfer: ....

2. Prüfer: ....

3. Prüfer: ....

4. Prüfer: ....

im Promotionskolloquium

Tag des Promotionskolloquiums: ....

Doktorurkunde ausgehändigt am: ....

Für meine Eltern und Tanja

Zusammenfassung

In dieser Arbeit werden die elektronischen Transporteigenschaften von Graphen-basierten mesoskopischen Festkörpersystemen mittels numerischer und analytischer Methoden untersucht. Im Besonderen wird analysiert, wie Konzepte von Quanteninterferenz und Unordnung, die eine wesentliche Rolle für mesoskopische Systeme spielen, durch die einzigartigen elektronischen und Transporteigenschaften von Graphen beeinflusst werden. Wir betrachten den berühmten Aharonov-Bohm-Effekt in ringförmigen Transportgeometrien, geben einen Überblick über die Entwicklung dieses Themas in den letzten Jahren und befassen uns mit den charakteristischen Merkmalen, die fundamentale Phänomene wie Klein-Tunneln und gerichtete Andreev-Reflexion, welche spezifisch für Graphen sind, in den Magnetooszillationen der elektrischen Leitfähigkeit aufweisen. Dazu führen wir eine Variante der Methode der rekursiven Greenschen Funktionen ein, die ein effizientes numerisches Verfahren zur Berechnung von Transportobservablen in effektiv nicht-wechselwirkenden, offenen Quantensystemen im Rahmen eines „tight binding"-Modells darstellt. Diese Methode wird desweiteren zur Erforschung eines speziellen Typs von Unordnung herangezogen, nämlich kurzreichweitiger, resonanter Streuzentren wie stark gebundene Adatome oder Moleküle, die als Fehlstellen in der Graphen-Gitterstruktur modelliert werden können. Diese numerische Analyse der elektrischen Leitfähigkeit bei Anwesenheit resonanter Streuzentren in Graphen führt zu einer nicht-trivialen Klassifizierung von Fremdatom-Gitterplätzen innerhalb des Graphen-Gitters und wird durch eine unabhängige analytische Behandlung im Rahmen der Dirac-Gleichung bekräftigt. Die vorliegende Arbeit enthält weiterhin eine formale Einführung in das Thema des Nichtgleichgewichts-Quantentransports, wie es für die Entwicklung der genannten numerischen Methode dienlich ist, eine allgemeine Einführung in die Physik von Graphen mit Fokus auf die speziellen Aspekte, die in dieser Arbeit untersucht werden, sowie eine abschließende Darstellung, in der die erhaltenen Ergebnisse zusammengefasst und offene Fragen sowie mögliche zukünftige Entwicklungen hervorgehoben werden.

Summary

In this thesis, the electronic transport properties of mesoscopic condensed matter systems based on graphene are investigated by means of numerical as well as analytical methods. In particular, it is analyzed how the concepts of quantum interference and disorder, which are essential to mesoscopic devices in general, are affected by the unique electronic and transport properties of the graphene material system. We consider the famous Aharonov–Bohm effect in ring-shaped transport geometries, and, besides providing an overview over the recent developments on the subject, we study the signatures of fundamental phenomena such as Klein tunneling and specular Andreev reflection, which are specific to graphene, in the magnetoconductance oscillations. To this end, we introduce and utilize a variant of the well-known recursive Green's function technique, which is an efficient numerical method for the calculation of transport observables in effectively non-interacting open quantum systems in the framework of a tight binding model. This technique is also applied to study the effects of a specific kind of disorder, namely short-range resonant scatterers, such as strongly bound adatoms or molecules, that can be modeled as vacancies in the graphene lattice. This numerical analysis of the conductance in the presence of resonant scatterers in graphene leads to a non-trivial classification of impurity sites in the graphene lattice and is further substantiated by an independent analytical treatment in the framework of the Dirac equation. The present thesis further contains a formal introduction to the topic of non-equilibrium quantum transport as appropriate for the development of the numerical technique mentioned above, a general introduction to the physics of graphene with a focus on the particular phenomena investigated in this work, and a conclusion where the obtained results are summarized and open questions as well as potential future developments are highlighted.

Contents

Contents

Introduction

It is nowadays a well-known fact that the ongoing miniaturization of information and computer technology, which over the past decades followed a deterministic development given by the famous Moore's law [Moo65], is limited by quantum effects. These effects come into play when the device size becomes comparable to the quantum mechanical phase-coherence length—typically on the sub-micrometer- or nanoscale—in which case quantization phenomena and quantum corrections to classical expressions for electron transport in such devices become dominant and the ohmic behavior breaks down. The scale of the phase-coherence length thus defines an intermediate regime between the macroscopic and microscopic worlds, where the laws of physics are fully governed by classical and quantum dynamics, respectively. Consequently, the study of condensed matter at this length scale is commonly referred to as mesoscopic[1] physics [Dat05, Bee91].

The field of mesoscopic physics became active during the 1980s with the fabrication of the first devices that allowed for experiments at the mesoscopic scale. While some of the initial experiments utilized conventional metallic conductors, semiconductor heterostructures such as GaAs−AlGaAs have soon proved to be the material system of choice, and the field developed rapidly with the first commercial applications of semiconductor devices in 1990 [Dat05].

The phase-coherent character of electronic transport at the mesoscale gives rise to interference of electron wavefunctions, leading to quantum corrections to the conductance. Fundamental consequences of quantum interference include:

- weak localization, i.e., enhanced backscattering of electrons and thus a decrease in conductance of order e^2/h due to constructive interference of time-reversed scattering paths as long as time-reversal symmetry is preserved,

- the Aharonov–Bohm effect [Aha59], i.e., conductance oscillations as a function of the magnetic flux enclosed by different electron trajectories in ring-like geometries, and

- universal conductance fluctuations, i.e., reproducible conductance fluctuations of order e^2/h as a function of magnetic field or electron density and thus as a function of the Fermi wavelength.

It is also worth highlighting that since in the last case, the conductance fluctuates due to changes in the relative phases of different electron paths, leading to changes of the interference pattern, the corresponding quantum correction also depends on the particular microscopic distribution of impurities, representing scattering centers, whereas the classical conductance only depends on the impurity density [Dat05].

---

[1]from Ancient Greek mésos, "middle"

1

In 2004, the field of mesoscopic physics was impacted by the discovery of a novel material system exhibiting unique and intriguing transport properties. In Manchester, the group around Andre Geim and Konstantin Novoselov for the first time successfully isolated a single one-atom-thick layer of graphite called graphene [Nov04]. This perfectly two-dimensional material, which had been theoretically known for nearly 60 years [Wal47], shows surprising properties strongly resembling those of massless relativistic particles described by the Dirac equation, in contrast to electrons in conventional metal or semiconductor structures that can be described as massive, non-relativistic particles in terms of a Schrödinger equation with a renormalized (or effective) mass. The behavior as massless Dirac fermions leads to a variety of pseudorelativistic phenomena: The electronic excitations show a linear dispersion forming a so-called Dirac cone and carry a novel degree of freedom called pseudospin—due to its resemblance to the real electron spin—which is intimately connected to the fact that the primitive unit cell contains two (identical) carbon atoms, giving rise to a two-fold sublattice structure (see Fig. 3.1) [CN09]. Further, the direction of this pseudospin is either parallel or antiparallel to the momentum of the low-energy excitations, which thus exhibit a chiral[2] nature, leading, for instance, to the phenomenon of Klein tunneling through regions of different doping [Kle29, Kat06b, Che06]. The spinor structure of the low-energy excitations is further extended by a two-fold orbital degeneracy due to the presence of two Dirac cones, one in each of the two inequivalent "valleys" of the full energy spectrum (see Fig. 3.2), giving rise to an additional isospin degree of freedom. In analogy to spintronics, which is concerned with the utilization of the intrinsic electron spin for quantum information purposes, the field of "valleytronics" developed, which is concerned with the utilization of the valley isospin [Ryc07, Nov11, Akh08a].

For their work on graphene, Geim and Novoselov received the Nobel prize for physics in 2010. At present, there is still ongoing progress in investigating graphene physics for a better understanding of the fundamental properties and the development of possible applications in quantum information theory. This thesis and the original published work referenced herein constitute a contribution to this purpose. We consider fundamental graphene-specific aspects and phenomena in the context of mesoscopic device implementations and the corresponding paradigms of quantum interference effects as well as the effects of disorder, which strongly affect and determine the properties of electronic transport in mesoscopic systems. To this end, in the first part of this thesis, we present a general theory for the description of quantum transport and the explicit calculation of observables such as the conductance. More specifically, since transport processes are non-equilibrium many-body phenomena by definition, we introduce a non-equilibrium field-theoretic formalism as the language of choice in Chapter 1. For the case of (effectively) non-interacting systems, which we consider throughout this work, this formal treatment of the quantum transport problem reduces to the more descriptive language in terms of the scattering matrix, or S-matrix, see, e.g., Ref. [Dat05]. Further, since the device geometries of interest rarely allow for a fully analytical treatment, in Chapter 2, we introduce a computational scheme for the numerical calculation of transport observables in a tight binding model[3] for generic lattice structures. In the second part of this thesis, we apply this scheme to the particular case

---

[2] In the context of graphene, the terms "helicity" and "chirality" are often used interchangeably [CN09].

[3] See Section 2.5.1 of Ref. [Wim09a] for a list of references for different tight binding representations.

of the graphene lattice and investigate the specific electronic transport properties of this material in quantum interference device geometries as well as in the presence of impurities. More specifically, after a general introduction to the physics of graphene in Chapter 3, in Chapter 4, we investigate the magnetoconductance of graphene ring structures into which either Klein tunneling [Kle29, Kat06b, Che06] (by means of a side gate electrode potential) or Andreev reflection [And64, Bee06] (by means of a superconducting contact) is introduced—two phenomena, which are known to be closely related in graphene [Bee08b]. In both cases, the magnetoconductance shows clear Aharonov–Bohm oscillations [Aha59] with signatures specific to the peculiar electronic properties of graphene. We also provide a review of recent developments on the topic of the Aharonov–Bohm effect in graphene and highlight unresolved issues. In Chapter 5, we turn to graphene-specific effects of disorder, concentrating on resonant scatterers, i.e., strongly bound adatoms or molecules that effectively behave as vacancies in the graphene lattice. Since graphene exhibits a pseudospin structure in form of the sublattice degree of freedom, in addition to the real electron spin, it is natural to assume that transport properties are susceptible not only to the impurity density but also to an imbalance in the distribution of such impurities over the two sublattices. However, we will show that transport properties also show an additional dependence on a more subtle structural scheme, exhibiting three inequivalent sites per sublattice, which is not evident from the real space lattice or pseudospin structure, but rather originates from an interference between the two valleys and thus from the isospin structure. In Chapter 6, we conclude our work by providing a summary as well as an outlook towards potential future developments of the field.

Part I

Theoretical framework for quantum transport

Chapter 1

Non-equilibrium Green's function formalism of quantum transport

In this chapter, where we follow in parts the presentation given in Refs. [Ram07, Wim09a], we will outline the general theory of non-equilibrium quantum dynamics in the modern formulation pioneered by Schwinger [Sch61], Kadanoff and Baym [Kad62], as well as Keldysh [Kel65] and Craig [Cra68].

Due to its many-body nature, the problem of quantum transport is best formulated in second quantization. We will therefore shortly summarize the basic expressions in this language, as far as they are needed for the theory that follows; a detailed treatment can be found in standard textbooks on quantum theory, such as Ref. [Nol05]. To this end, we will choose the lattice description—i.e., representations in a discrete basis set—rather than the more familiar continuum description since we will implement the resulting transport equations numerically in a tight binding model.

We will then introduce the central element of the Keldysh formalism, namely the closed-time [Sch61] or (Schwinger–)Keldysh contour [Ram07, Wim09a], which distinguishes this specific formulation from more traditional approaches and which we will refer to simply as the Keldysh contour. The theory describing the non-equilibrium situation of quantum transport will turn out to have the form of a perturbation theory, which will be treated numerically exact to all orders and which is conveniently described in terms of Green's functions, or "propagators" as they are commonly called. In this non-equilibrium Green's function (NEGF) formalism, the core of perturbation theory—the Dyson equation—will relate the non-equilibrium properties to equilibrium Green's functions, which are intimately connected with the observables of interest in steady state situations.

In the following, we will restrict ourselves to quadratic Hamiltonians, i.e., Hamiltonians that are quadratic in field operators, describing either non-interacting systems or interactions that are taken into account as effective potentials in a mean-field approximation, such as the Hartree(–Fock) approximations to the Coulomb interaction. At a later stage, we will shortly outline the extensions to the formalism that arise when interactions are generically included.

1.1 Basic definitions

Consider a quantum system that is prepared at time $t = t_0$ in a state described by a density matrix $\rho(t_0) \equiv \rho_0$. Let further be t_0 the reference time where Schrödinger, Heisenberg, and

interaction pictures coincide. Let our system be described by a quadratic Hamiltonian

$$\mathcal{H}(t) \equiv \mathcal{H}_0 + \mathcal{H}'(t)$$

with a time-independent part

$$\mathcal{H}_0 \equiv \sum_{i,j} (H_0)_{ij} \psi^\dagger(i)\psi(j), \quad \hat{H}_0 = \sum_{i,j} (H_0)_{ij} |i\rangle\langle j|, \quad (H_0)_{ij} \equiv \langle i|\hat{H}_0|j\rangle, \qquad (1.1)$$

and a time-dependent part

$$\mathcal{H}'(t) \equiv \sum_{i,j} V_{ij}(t) \psi^\dagger(i)\psi(j), \quad \hat{V}(t) = \sum_{i,j} V_{ij}(t) |i\rangle\langle j|, \quad V_{ij}(t) \equiv \langle i|\hat{V}(t)|j\rangle, \qquad (1.2)$$

written in second quantized form with corresponding single particle operators $\hat{H}_0$ and $\hat{V}(t)$ according to the usual prescription for the construction of many-body operators. The fermionic field operator $\psi^\dagger(i)$ describes the creation of a particle in a state $|i\rangle$ of some discrete basis set of single particle states $\{|i\rangle\}$ that we will concretize at a later stage. The expansion coefficient of the single-particle operators $\hat{H}$ and $\hat{V}(t)$ in this basis constitute elements $(H_0)_{ij}$ and $V_{ij}(t)$ of matrices H_0 and $V(t)$, respectively, as indicated above. Later, $\mathcal{H}'(t)$ will be interpreted as a perturbation to the unperturbed system described by $\mathcal{H}_0$.

In order to use a compact notation, we define

$$\mathcal{U}_{\mathcal{X}}(t,t') \equiv \mathcal{T}\exp\left(-\frac{\mathrm{i}}{\hbar}\int_{t'}^{t} \mathcal{X}(\tilde{t})\,\mathrm{d}\tilde{t}\right)$$

for some possibly time-dependent operator $\mathcal{X}(t)$, where the exponential is defined via the series expansion and $\mathcal{T}$ denotes the usual time ordering operator that orders expressions according to their time argument with later times to the left. We remind the reader that, according to the usual convention, each interchange of fermionic field operators under this operation generates an additional minus sign. Similarly, the anti-time ordering operator $\widetilde{\mathcal{T}}$ orders expressions with later times to the right.

For some operator $\mathcal{O}(t)$ in the Schrödinger picture, which may exhibit an explicit dependence on time, we further define

$$\mathcal{O}_{\mathcal{X}}(t) \equiv \mathcal{U}_{\mathcal{X}}^\dagger(t,t_0)\mathcal{O}(t)\mathcal{U}_{\mathcal{X}}(t,t_0).$$

Then, $\mathcal{O}_{\mathcal{H}}(t)$ is the operator in the Heisenberg picture, where the time evolution of operators is governed by $\mathcal{H}(t)$, and, for the expectation value, we have

$$\langle\mathcal{O}(t)\rangle \equiv \mathrm{tr}(\rho(t)\mathcal{O}(t)) = \mathrm{tr}(\rho_0\mathcal{O}_{\mathcal{H}}(t)) \equiv \langle\mathcal{O}_{\mathcal{H}}(t)\rangle.$$

Similarly, $\mathcal{O}_{\mathcal{H}_0}(t)$ is the operator in the interaction picture, where time evolution of operators is governed by $\mathcal{H}_0$ and $\mathcal{H}'(t)$ is interpreted as perturbation.

Since we will make excessive use of field operators in the interaction picture, we introduce the shorthand notation

$$c_i(t) \equiv \psi_{\mathcal{H}_0}(i,t).$$

Utilizing the fermionic anti-commutation relations, we obtain the equation of motion for the field operator,

$$
\begin{aligned}
i\hbar\frac{\mathrm{d}}{\mathrm{d}t}c_i(t) &= [c_i(t), \mathcal{H}_0] \\
&= \mathcal{U}_{\mathcal{H}_0}^\dagger(t, t_0) \sum_{k,j} (H_0)_{kj} \Big(\underbrace{\psi(i)\psi^\dagger(k)}_{\delta_{ik} - \psi^\dagger(k)\psi(i)} \psi(j) - \psi^\dagger(k) \underbrace{\psi(j)\psi(i)}_{-\psi(i)\psi(j)} \Big) \mathcal{U}_{\mathcal{H}_0}(t, t_0) \\
&= \sum_j (H_0)_{ij} c_j(t).
\end{aligned}
\tag{1.3}
$$

It is easily verified that the solution to this equation is given by

$$
c_i(t) = \sum_\alpha (\varphi_\alpha)_i \mathrm{e}^{-iE_\alpha(t-t_0)/\hbar} a_\alpha,
\tag{1.4}
$$

where $(\varphi_\alpha)_i \equiv \langle i|\varphi_\alpha\rangle$ and $|\varphi_\alpha\rangle$ and E_α denote eigenstates and eigenvalues of $\hat{H}_0$, respectively,

$$
\hat{H}_0|\varphi_\alpha\rangle = E_\alpha|\varphi_\alpha\rangle,
$$

and a_α denote the corresponding field operators that diagonalize $\mathcal{H}_0$,

$$
\mathcal{H}_0 = \sum_\alpha E_\alpha a_\alpha^\dagger a_\alpha.
$$

In the following, we assume $\mathcal{H}'(t \leq t_0) = 0$ so that the system is in thermal equilibrium at $t = t_0$ and the corresponding grand canonical equilibrium density matrix ρ_0 is governed by $\mathcal{H}_0$,[1]

$$
\rho_0 = \frac{1}{Z} \mathrm{e}^{-\beta(\mathcal{H}_0 - \mu\mathcal{N})},
\tag{1.5}
$$

where $\beta \equiv (k_B T)^{-1}$ is the inverse temperature, μ is the chemical potential, $\mathcal{N} \equiv \sum_i \psi^\dagger(i)\psi(i)$ is the number operator, and the partition function is given by

$$
Z = \mathrm{tr}\, \mathrm{e}^{-\beta(\mathcal{H}_0 - \mu\mathcal{N})}.
$$

If $\mathcal{H}_0$ describes a set of independent subsystems, as will be the case later on,

$$
\mathcal{H}_0 = \mathcal{H}_{S_1,0} \otimes \mathbf{1}_{S_2} \otimes \mathbf{1}_{S_3} \otimes \ldots + \mathbf{1}_{S_1} \otimes \mathcal{H}_{S_2,0} \otimes \mathbf{1}_{S_3} \otimes \ldots + \ldots,
$$

the density matrix at $t = t_0$ is the direct product of the individual density matrices, describing the individual thermal equilibrium state of each subsystem, i.e.,

$$
\rho_0 = \rho_{S_1,0} \otimes \rho_{S_2,0} \otimes \rho_{S_3,0} \otimes \cdots
$$

We will now introduce the formalism that allows us to express the non-equilibrium situation

---

[1] Note that this assumption does not pose a limitation for practical purposes, since thermal equilibrium is the only meaningful condition accessible for preparation of a system consisting of a huge number of particles.
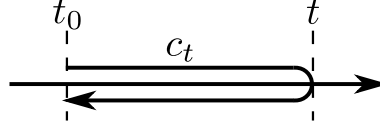
Figure 1.1: The closed time contour c_t, starting at t_0, running through t, and going back to t_0. The contour is set off from the real time axis for clarity only; this must not be understood as (infinitesimal) shift into the complex plane.

described by $\mathcal{H}(t)$ in terms of the equilibrium state at $t = t_0$ (described by $\mathcal{H}_0$) in form of a perturbation theory.

1.2 Keldysh contour and Dyson equation

Interpreting $\mathcal{H}'(t)$ as a perturbation, we first note that an operator in the Heisenberg picture can be expressed in the interaction picture as

$$\mathcal{T}_{c_t} \exp\left(-\frac{\mathrm{i}}{\hbar} \int_{c_t} \mathcal{H}'_{\mathcal{H}_0}(\tilde{\tau}) \, \mathrm{d}\tilde{\tau}\right) \mathcal{O}_{\mathcal{H}_0}(\tau)$$

$$= \left(\tilde{\mathcal{T}} \exp\left(-\frac{\mathrm{i}}{\hbar} \int_t^{t_0} \mathcal{H}'_{\mathcal{H}_0}(\tilde{t}) \, \mathrm{d}\tilde{t}\right)\right) \mathcal{O}_{\mathcal{H}_0}(t) \left(\mathcal{T} \exp\left(-\frac{\mathrm{i}}{\hbar} \int_{t_0}^t \mathcal{H}'_{\mathcal{H}_0}(\tilde{t}) \, \mathrm{d}\tilde{t}\right)\right)$$

$$= \mathcal{U}^{\dagger}_{\mathcal{H}'_{\mathcal{H}_0}}(t, t_0) \mathcal{U}^{\dagger}_{\mathcal{H}_0}(t, t_0) \mathcal{O}(t) \mathcal{U}_{\mathcal{H}_0}(t, t_0) \mathcal{U}_{\mathcal{H}'_{\mathcal{H}_0}}(t, t_0)$$

$$= \mathcal{O}_{\mathcal{H}}(t), \tag{1.6}$$

where $\mathcal{T}_{c_t}$ denotes time ordering along the contour c_t shown in Fig. 1.1, τ is the time lying on the contour c_t that corresponds to t (see the following remark), and in the last step, we used Dyson's formula [Ram07],

$$\underbrace{\mathcal{T} \exp\left(-\frac{\mathrm{i}}{\hbar} \int_{t_0}^t \mathcal{H}'_{\mathcal{H}_0}(\tilde{t}) \, \mathrm{d}\tilde{t}\right)}_{\mathcal{U}_{\mathcal{H}'_{\mathcal{H}_0}}(t,t_0)} = \underbrace{\exp\left(\frac{\mathrm{i}}{\hbar} \mathcal{H}_0 \times (t - t_0)\right)}_{\mathcal{U}^{\dagger}_{\mathcal{H}_0}(t,t_0)} \underbrace{\mathcal{T} \exp\left(-\frac{\mathrm{i}}{\hbar} \int_{t_0}^t \mathcal{H}(\tilde{t}) \, \mathrm{d}\tilde{t}\right)}_{\mathcal{U}_{\mathcal{H}}(t,t_0)},$$

which can easily be verified by direct differentiation—applying $(\mathrm{i}\hbar\partial_t - \mathcal{H}'_{\mathcal{H}_0}(t))$ from the left on both sides gives zero—and noting that both sides fulfill the same initial condition at $t = t_0$ trivially.

One remark concerning notation: We denote times on a contour in general by the Greek letter τ. In addition, $t^{\rightarrow}$ denotes a time on the forward part of a contour, whereas $t^{\leftarrow}$ denotes a time on the backward part of a contour. "Contour times" that lie at the turning point are (unambiguously) identified with corresponding "standard times", $\tau = t^{\rightarrow} = t^{\leftarrow} = t$. So, strictly speaking, in the first line of Eq. (1.6), the argument t of the operator $\mathcal{O}$, which is a standard time, has been identified with the turning point of the contour under the contour time ordering operation. As shown in the first step of Eq. (1.6), the contour time ordering operation orders expressions according to contour times and then projects all contour times onto corresponding standard times. In addition, note that contour time has nothing to do
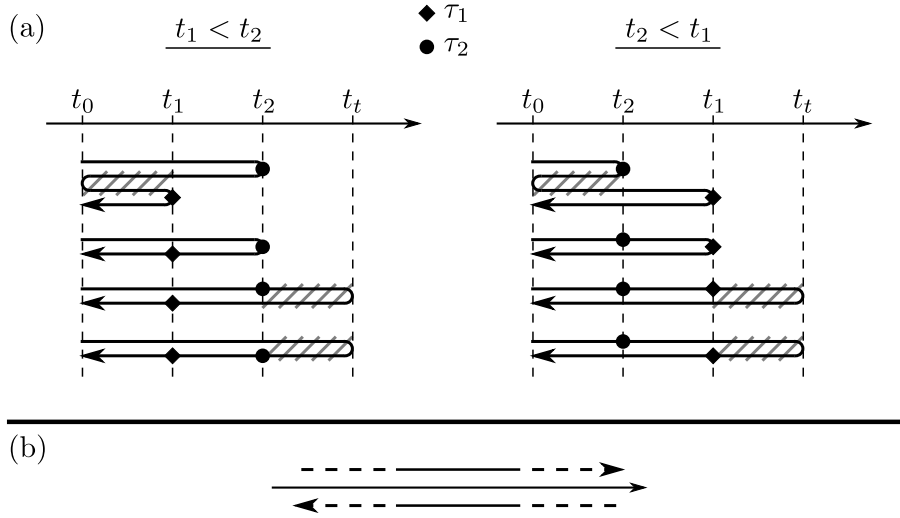
Figure 1.2: (a) Sets of contours c that are equivalent with respect to Eq. (1.7) due to cancellation of hatched parts as explained in the text, shown for the cases $t_1 < t_2$ and $t_2 < t_1$, respectively. Contour times $\tau_{1,2}$ correspond to standard times $t_{1,2}$. (b) The Keldysh contour C, which is obtained by taking the limits $t_0 \to -\infty$ and $t_t \to \infty$.

with imaginary time; times on the contour in Fig. 1.1 must not be understood as being (infinitesimally) shifted away from the real time axis into the complex plane.[2]

Since observables will be expressed through correlation functions, i.e., expectation values of products of field operators, we also infer the corresponding expression for products of operators,

$$\mathcal{O}_{\mathcal{H}}(t_1)\mathcal{O}_{\mathcal{H}}(t_2) = \mathcal{T}_c \exp\left(-\frac{\mathrm{i}}{\hbar}\int_c \mathcal{H}'_{\mathcal{H}_0}(\tilde{\tau})\,\mathrm{d}\tilde{\tau}\right)\mathcal{O}_{\mathcal{H}_0}(\tau_1)\mathcal{O}_{\mathcal{H}_0}(\tau_2), \tag{1.7}$$

where c denotes any of the contours shown in Fig. 1.2(a). All of these contours are equivalent with respect to Eq. (1.7) since hatched parts in Fig. 1.2(a) correspond to terms that are of the form

$$\mathcal{U}^{\dagger}_{\mathcal{H}'_{\mathcal{H}_0}}(t,t')\mathcal{U}_{\mathcal{H}'_{\mathcal{H}_0}}(t,t') = \mathcal{U}_{\mathcal{H}'_{\mathcal{H}_0}}(t,t')\mathcal{U}^{\dagger}_{\mathcal{H}'_{\mathcal{H}_0}}(t,t') = \mathbf{1}$$

and therefore cancel. We thus consider in the following the generic contour by taking the limits $t_t \to \infty$ and $t_0 \to -\infty$, the latter being justified by the fact that we will only be interested in steady state properties.[3] This contour C, depicted in Fig. 1.2(b), is called "Keldysh contour".

We now define the central object of the perturbation theory, namely the contour-ordered Green's function, which is a correlation function of quantum fields and from which observables

---

[2] We therefore also use the term "standard time" rather than "real time".

[3] A strict definition of the steady state, that implies translational invariance in time, will be given in Section 1.6.

will be derived:

$$
\begin{aligned}
G_{ij}(\tau, \tau') &\equiv -\frac{\mathrm{i}}{\hbar} \Big\langle \mathcal{T}_C \psi_{\mathcal{H}}(i, \tau) \psi_{\mathcal{H}}^\dagger(j, \tau') \Big\rangle \\
&= -\frac{\mathrm{i}}{\hbar} \operatorname{tr} \left(\rho_0 \mathcal{T}_C \exp\left(-\frac{\mathrm{i}}{\hbar} \int_C \sum_{k,l} V_{kl}(\tilde{\tau}) c_k^\dagger(\tilde{\tau}) c_l(\tilde{\tau}) \, \mathrm{d}\tilde{\tau} \right) c_i(\tau) c_j^\dagger(\tau') \right) \\
&\equiv \sum_{n=0}^{\infty} G_{ij}^{(n)}(\tau, \tau'),
\end{aligned}
\tag{1.8}
$$

where we employed Eq. (1.7) and the sum refers to the series expansion of the exponential.

Wick's theorem

In order to evaluate Eq. (1.8), we may employ Wick's theorem in the variant applicable to finite temperatures,[4] which provides a prescription how expectation values of strings of field operators, which appear by expanding the exponential, can be expressed through products of expectation values of pairs of field operators. For a general proof of the theorem, we refer the reader to Ref. [Ram07].

The contribution $G_{ij}^{(n)}(\tau, \tau')$ to Eq. (1.8) due to the n-th order term of the series expansion of the exponential contains a quadratically weighted trace[5] of a contour time ordered string of field operators,

$$
\operatorname{tr}\left(\rho_0 \mathcal{T}_C \, c_i(\tau) c_{k_1}^\dagger(\tilde{\tau}_1) \, c_{l_1}(\tilde{\tau}_1) c_{k_2}^\dagger(\tilde{\tau}_2) \ldots c_{l_{n-1}}(\tilde{\tau}_{n-1}) c_{k_n}^\dagger(\tilde{\tau}_n) \, c_{l_n}(\tilde{\tau}_n) c_j^\dagger(\tau') \right),
\tag{1.9}
$$

where we have permuted the field operators under the contour time ordering operation without an additional minus sign, since the number of transpositions is even. Wick's theorem is the statement that such an expression can be rewritten by partitioning the string of field operators into pairs, writing down the product of the expectation values of these pairs, and summing these products over all possibilities of pair formation. One way of choosing pairs is already indicated in Eq. (1.9), giving rise to the product

$$
\begin{aligned}
&\operatorname{tr}\left(\rho_0 \mathcal{T}_C c_i(\tau) c_{k_1}^\dagger(\tilde{\tau}_1) \right) \operatorname{tr}\left(\rho_0 \mathcal{T}_C c_{l_1}(\tilde{\tau}_1) c_{k_2}^\dagger(\tilde{\tau}_2) \right) \ldots \\
&\quad \times \operatorname{tr}\left(\rho_0 \mathcal{T}_C c_{l_{n-1}}(\tilde{\tau}_{n-1}) c_{k_n}^\dagger(\tilde{\tau}_n) \right) \operatorname{tr}\left(\rho_0 \mathcal{T}_C c_{l_n}(\tilde{\tau}_n) c_j^\dagger(\tau') \right) \\
&= (\mathrm{i}\hbar)^{n+1} G_{ik_1}^{(0)}(\tau, \tilde{\tau}_1) G_{l_1 k_2}^{(0)}(\tilde{\tau}_1, \tilde{\tau}_2) \ldots G_{l_{n-1} k_n}^{(0)}(\tilde{\tau}_{n-1}, \tilde{\tau}_n) G_{l_n j}^{(0)}(\tilde{\tau}_n, \tau'),
\end{aligned}
$$

according to Wick's theorem. Due to integration over internal contour times, there are $n!$ equivalent terms of this form, canceling the prefactor $1/n!$ that originates from the expansion of the exponential. Combinations in which two annihilation operators or two creation operators are paired obviously do not contribute since such operators change the number

---

[4] In the original formulation [Wic50], Wick's theorem refers to an operator identity valid at zero temperature, i.e., in a ground state formalism.

[5] A quadratically weighted trace is an expectation value with respect to a density matrix of the form (1.5) governed by a quadratic Hamiltonian.

of particles. Combinations allowing for a factorization of the n integrations contained in $G_{ij}^{(n)}(\tau, \tau')$ do not contribute either since integrals of the form

$$\int \ldots \int G_{l_1 k_2}^{(0)}(\tilde{\tau}_1, \tilde{\tau}_2) G_{l_2 k_3}^{(0)}(\tilde{\tau}_2, \tilde{\tau}_3) \ldots G_{l_m k_1}^{(0)}(\tilde{\tau}_m, \tilde{\tau}_1) \, \mathrm{d}\tilde{\tau}_1 \ldots \mathrm{d}\tilde{\tau}_m, \qquad m \leq n,$$

clearly vanish.[6] We therefore have

$$G_{ij}^{(n)}(\tau, \tau') = \int \ldots \int \sum_{k_1 \ldots k_n} \sum_{l_1 \ldots l_n} G_{ik_1}^{(0)}(\tau, \tilde{\tau}_1) V_{k_1 l_1}(\tilde{\tau}_1) G_{l_1 k_2}^{(0)}(\tilde{\tau}_1, \tilde{\tau}_2) V_{k_2 l_2}(\tilde{\tau}_2) \ldots$$

$$\times V_{k_n l_n}(\tilde{\tau}_n) G_{l_n j}^{(0)}(\tilde{\tau}_n, \tau') \, \mathrm{d}\tilde{\tau}_1 \ldots \mathrm{d}\tilde{\tau}_n$$

$$= \int \ldots \int \left(G^{(0)}(\tau, \tilde{\tau}_1) V(\tilde{\tau}_1) G^{(0)}(\tilde{\tau}_1, \tilde{\tau}_2) V(\tilde{\tau}_2) \ldots V(\tilde{\tau}_n) G^{(0)}(\tilde{\tau}_n, \tau') \right)_{ij} \, \mathrm{d}\tilde{\tau}_1 \ldots \mathrm{d}\tilde{\tau}_n,$$

where we introduced the matrix $G^{(0)}(\tau, \tau')$ with elements $(G^{(0)}(\tau, \tau'))_{ij} \equiv G_{ij}^{(0)}(\tau, \tau')$ and identified the sums with corresponding matrix products. Condensing the notation even more[7] by implying integration over internal contour times, we arrive at the Dyson equation,[8]

$$G = \sum_{n=0}^{\infty} G^{(n)} = G^{(0)} + G^{(0)} V G^{(0)} + G^{(0)} V G^{(0)} V G^{(0)} + \ldots$$

$$= G^{(0)} + G^{(0)} V G$$

$$= G^{(0)} + G V G^{(0)}, \tag{1.10}$$

where we introduced matrices G and $G^{(n)}$ analogous to $G^{(0)}$. The non-equilibrium situation can thus be described in terms of an infinite series of products involving the corresponding equilibrium Green's function of the unperturbed system and the perturbation Hamiltonian. Commonly, this expression is evaluated approximately by taking the elements of the series expansion into account only up to a certain order n. In our work, we will treat the Dyson equation exactly, taking all orders into account. In the following, we will describe how this is achieved for open quantum systems, where particles are allowed to be injected into and extracted from the system and where corresponding transport observables are of interest.

1.3 Effective description of open quantum systems

The systems considered in this work have the generic structure shown in Fig. 1.3. A central scattering region S is connected to a number of leads L_l, $l \in \{1, \ldots, N_L\}$, through which particles are able to enter and leave the scattering region. To accommodate the open character of the system, the leads are assumed to extend to infinity and the system Green's

---

[6] This is easily verified by noting that contributions of forward and backward parts of the contour cancel when integrating along the rightmost contour time variable, i.e., the one corresponding to the largest standard time variable. Also see the last pair of equivalent contours in Fig. 1.2(a).

[7] In analogy, one may think of a matrix structure in contour time with V being diagonal in contour time, $V(\tau_n, \tau_m) = V(\tau_n) \delta(\tau_n - \tau_m)$.

[8] We will encounter more variants of the Dyson equation in the following. In all these cases, the last equality of Eq. (1.10), which is obvious by iteration, holds correspondingly.
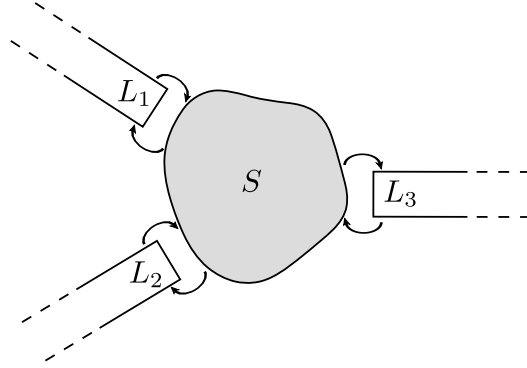
Figure 1.3: Sketch of a typical transport setup consisting of a central scattering region S and a number of leads L_l, $l \in \{1, \ldots, N_L\}$, with $N_L = 3$ in this case. The leads are assumed to extend to infinity. In the non-equilibrium situation, lead L_l is coupled to the scattering region via a coupling term V_{SL_l} (and the hermitian conjugate $V_{L_l S} = V_{SL_l}^\dagger$) as indicated by the arrows.

function G—as well as $G^{(0)}$—is therefore given by a matrix of infinite size. A direct numerical evaluation of Eq. (1.10) is thus not possible. To remedy this, we will introduce an effective description of the scatterer, which again has the form of the Dyson equation but where the hermitian perturbation Hamiltonian is amended by a so-called self-energy, which is in general non-hermitian, describing the effects of in- and outflow of particles through the leads.

Let us first substantiate how the states $|i\rangle$ of our discrete basis are composed. Since we deal with a translationally non-invariant system, the basis states are conveniently characterized by position degrees of freedom, rather than momentum degrees of freedom. In addition, the particles may have internal degrees of freedom, such as spin. Thus, a basis state $|i\rangle \equiv |\mathbf{x}_i, s_i, \ldots\rangle$ describes a particle at position[9] $\mathbf{x}_i$ with spin s_i and possibly additional degrees of freedom.

In the following, we will make extensive use of matrices acting on subspaces corresponding to individual subsystems, i.e., individual parts of the full generic setup as shown in Fig. 1.3. We therefore introduce the following notation: Let $|i_A\rangle$ and $|j_B\rangle$ describe states in subsystems A and B, respectively. A generic single-particle operator $\hat{X}_{AB}$ connecting the two subsystems can then be written as

$$\hat{X}_{AB} \equiv \sum_{ij} |i_A\rangle\langle i_A|\hat{X}|j_B\rangle\langle j_B|$$

and the corresponding matrix X_{AB} is given by the matrix elements

$$(X_{AB})_{ij} \equiv \langle i_A|\hat{X}|j_B\rangle.$$

For the special case $A = B$, we further define $\hat{X}_A \equiv \hat{X}_{AA}$ and $X_A \equiv X_{AA}$.

The matrix Green's function components that describe the scattering region are then

---

[9] Note that by choosing a discrete basis in position representation, the particles described by such basis states are assumed to be located (with some orbital wavefunction) on the sites of a lattice—as they naturally are in condensed matter systems—rather than at some position in continuous space.

obtained from Eq. (1.10) as

$$G_S = G_S^{(0)} + G_S^{(0)}(V_S + \Sigma)G_S, \tag{1.11}$$

with the so-called self-energy of the leads,

$$\Sigma \equiv \sum_L V_{SL} G_L^{(0)} V_{LS}, \tag{1.12}$$

where S labels the subsystem of the scattering region and L labels the subsystem of one particular lead. Note that $G_{SL}^{(0)} = G_{LS}^{(0)} = \mathbf{0}$ for any of the leads since in the initial thermal equilibrium state leads and scatterer are all disconnected from each other and therefore they are independent subsystems at $t = t_0$. Thus, we also can infer

$$G_{LS} = G_L^{(0)} \left(V_{LS} G_S + \sum_{L'} V_{LL'} G_{L'S} \right),$$

$$G_{SL} = \left(G_S V_{SL} + \sum_{L'} G_{SL'} V_{L'L} \right) G_L^{(0)}. \tag{1.13}$$

Since the number of lattice sites in the scattering region is finite, Eq. (1.11) is a matrix equation of finite-dimensional matrices—in contrast to Eq. (1.10)—in the form of a Dyson equation describing the scattering region, where the effect of the leads is captured in the self-energy Σ.

At first sight, it may seem that the evaluation of the self-energy is numerically not possible since it contains products with the infinite-dimensional matrices $G_L^{(0)}$. However, in practice only a few matrix elements in V_{SL} and V_{LS} are non-zero and therefore only a finite number of matrix elements of $G_L^{(0)}$ is involved in the matrix product, so that the calculation of Σ becomes feasible. We will discuss the explicit calculation of the self-energy in Section 2.1; in the next section, we will see how Eq. (1.11) can be expressed in standard time variables. A Fourier transform will then relate time and energy domains, which will allow for the calculation of steady state observables.

1.4 Transition from contour time to standard time

The mapping from contour times to standard times is not bijective since there are always two contour times—one on each branch of the contour—that correspond to the same standard time. We therefore introduce the lesser and greater Green's functions as

$$G^<(t_1, t_2) \equiv G(t_1^{\rightarrow}, t_2^{\leftarrow}),$$
$$G^>(t_1, t_2) \equiv G(t_1^{\leftarrow}, t_2^{\rightarrow}),$$

respectively, where $t_i^{\rightarrow}$ ($t_i^{\leftarrow}$) is a contour time lying on the forward (backward) part of the contour, corresponding to standard time t_i. The names are inspired by the fact that—by definition—the contour time associated with the first argument of the lesser (greater) Green's function is ensured to be earlier (later) than the contour time associated with the second

argument, $t_1^{\rightarrow} \overset{C}{<} t_2^{\leftarrow}$ $(t_1^{\leftarrow} \overset{C}{>} t_2^{\rightarrow})$, irrespective of the numerical values, since these times lie on different branches of the contour. We further define the retarded and advanced Green's functions as

$$
\begin{aligned}
G^r(t_1, t_2) &\equiv \quad \Theta(t_1 - t_2)(G^>(t_1, t_2) - G^<(t_1, t_2)), \\
G^a(t_1, t_2) &\equiv -\Theta(t_2 - t_1)(G^>(t_1, t_2) - G^<(t_1, t_2)) = (G^r(t_2, t_1))^\dagger,
\end{aligned}
$$

respectively, which are non-zero only if $t_1 > t_2$ and $t_1 < t_2$, respectively. In addition, we note the identities

$$
\begin{aligned}
G(t_1^{\rightarrow}, t_2^{\rightarrow}) &= G^<(t_1, t_2) + G^r(t_1, t_2) = G^>(t_1, t_2) + G^a(t_1, t_2), \\
G(t_1^{\leftarrow}, t_2^{\leftarrow}) &= G^<(t_1, t_2) - G^a(t_1, t_2) = G^>(t_1, t_2) - G^r(t_1, t_2),
\end{aligned}
\tag{1.14}
$$

which are easily verified using the property of the contour-ordered Green's function that it does not depend on whether the rightmost contour time is lying on the forward or backward branch of the contour,

$$
G(t_1^{\rightarrow}, t_2^{\rightarrow}) = \begin{cases} G(t_1^{\leftarrow}, t_2^{\rightarrow}) \\ G(t_1^{\rightarrow}, t_2^{\leftarrow}) \end{cases} \quad \text{and} \quad G(t_1^{\leftarrow}, t_2^{\leftarrow}) = \begin{cases} G(t_1^{\rightarrow}, t_2^{\leftarrow}) & \text{if } t_1 > t_2, \\ G(t_1^{\leftarrow}, t_2^{\rightarrow}) & \text{if } t_1 < t_2, \end{cases}
$$

see Fig. 1.2(a). Using Eq. (1.14), an expression of the form

$$
\gamma_{AB}(\tau_1, \tau_2) \equiv \int_C G_A(\tau_1, \tau) V_{AB}(\tau) G_B(\tau, \tau_2) \, \mathrm{d}\tau,
$$

appearing in Eqs. (1.10) and (1.11), can then be rewritten in standard time as

$$
\begin{aligned}
\gamma_{AB}^{\lessgtr}(t_1, t_2) &\equiv \gamma_{AB}(t_1^{\overrightarrow{\rightleftarrows}}, t_2^{\overleftarrow{\rightleftarrows}}) = \int_C G_A(t_1^{\overrightarrow{\rightleftarrows}}, \tau) V_{AB}(\tau) G_B(\tau, t_2^{\overleftarrow{\rightleftarrows}}) \, \mathrm{d}\tau \\
&= \int_{-\infty}^{\infty} G_A(t_1^{\overrightarrow{\rightleftarrows}}, t^{\rightarrow}) V_{AB}(t) G_B(t^{\rightarrow}, t_2^{\overleftarrow{\rightleftarrows}}) \, \mathrm{d}t + \int_{\infty}^{-\infty} G_A(t_1^{\overrightarrow{\rightleftarrows}}, t^{\leftarrow}) V_{AB}(t) G_B(t^{\leftarrow}, t_2^{\overleftarrow{\rightleftarrows}}) \, \mathrm{d}t \\
&= \int_{-\infty}^{\infty} \left(G_A^r(t_1, t) V_{AB}(t) G_B^{\lessgtr}(t, t_2) + G_A^{\lessgtr}(t_1, t) V_{AB}(t) G_B^a(t, t_2) \right) \mathrm{d}t,
\end{aligned}
$$

or

$$
\gamma_{AB}^{\lessgtr} = G_A^r V_{AB} G_B^{\lessgtr} + G_A^{\lessgtr} V_{AB} G_B^a \tag{1.15}
$$

in compact notation.[10] Analogous, using

$$
G^r - G^a = G^> - G^<, \tag{1.16}
$$

---

[10] Here, integration is of course implied over standard time.

we find

$$
\begin{aligned}
\gamma_{AB}^{r,a}(t_1, t_2) &\equiv \pm\Theta(\pm(t_1 - t_2))(\gamma_{AB}^{>} - \gamma_{AB}^{<})|_{(t_1,t_2)} \\
&= \pm\Theta(\pm(t_1 - t_2))\Big(G_A^r V_{AB}(G_B^{>} - G_B^{<}) + (G_A^{>} - G_A^{<})V_{AB}G_B^a\Big)\Big|_{(t_1,t_2)} \\
&= \pm\Theta(\pm(t_1 - t_2))\Big(G_A^r V_{AB}G_B^r - G_A^a V_{AB}G_B^a\Big)\Big|_{(t_1,t_2)} \\
&= (G_A^{r,a} V_{AB}G_B^{r,a})|_{(t_1,t_2)}.
\end{aligned}
$$

These identities—sometimes called analytic continuation rules [Wim09a, Hau96] although they are not related to imaginary times at all—allow for the transition from contour time to standard time and were originally established by Langreth [Lan72, Dev76]. It is clear from the definition that the identities (1.14) also hold for γ_{AB}—see again Fig. 1.2(a). Therefore, we can apply the same rules to an expression of the form

$$
\gamma_{ABC}(\tau_1, \tau_2) \equiv \int_C \gamma_{AB}(\tau_1, \tau)V_{BC}(\tau)G_C(\tau, \tau_2) \, \mathrm{d}\tau
$$

and obtain

$$
\begin{aligned}
\gamma_{ABC}^{\lessgtr} &= G_A^r V_{AB}G_B^r V_{BC}G_C^{\lessgtr} + (G_A^r V_{AB}G_B^{\lessgtr} + G_A^{\lessgtr}V_{AB}G_B^a)V_{BC}G_C^a, \\
\gamma_{ABC}^{r,a} &= G_A^{r,a} V_{AB}G_B^{r,a} V_{BC}G_C^{r,a}.
\end{aligned}
$$

Application to the Dyson equation

The Langreth rules derived above can now be applied to Eq. (1.11) giving

$$
G_S^{r,a} = G_{S,0}^{r,a} + G_{S,0}^{r,a}(V_S + \Sigma^{r,a})G_S^{r,a} \tag{1.17}
$$

and

$$
G_S^{\lessgtr} = G_{S,0}^{\lessgtr} + G_{S,0}^r(V_S + \Sigma^r)G_S^{\lessgtr} + G_{S,0}^r \Sigma^{\lessgtr}G_S^a + G_{S,0}^{\lessgtr}(V_S + \Sigma^a)G_S^a, \tag{1.18}
$$

where we defined $G_{S,0} \equiv G_S^{(0)}$, $G_{L,0} \equiv G_L^{(0)}$, and

$$
\Sigma^{r,a,\lessgtr} \equiv \sum_L V_{SL}G_{L,0}^{r,a,\lessgtr}V_{LS}.
$$

From Eq. (1.17), we can infer the identity $\big(\mathbf{1} + G_S^r(V_S + \Sigma^r)\big)\big(\mathbf{1} - G_{S,0}^r(V_S + \Sigma^r)\big) = \mathbf{1}$, which can be substituted into Eq. (1.18):

$$
\begin{aligned}
G_S^{\lessgtr} &= \Big(\mathbf{1} + G_S^r(V_S + \Sigma^r)\Big)\Big(G_{S,0}^{\lessgtr} + G_{S,0}^r \Sigma^{\lessgtr}G_S^a + G_{S,0}^{\lessgtr}(V_S + \Sigma^a)G_S^a\Big) \\
&= \underbrace{\Big(\mathbf{1} + G_S^r(V_S + \Sigma^r)\Big)G_{S,0}^{\lessgtr}\Big(\mathbf{1} + (V_S + \Sigma^a)G_S^a\Big)}_{\equiv G_{\mathrm{cor}}^{\lessgtr}} + G_S^r \Sigma^{\lessgtr}G_S^a, \tag{1.19}
\end{aligned}
$$

where in the last step we again used Eq. (1.17). In the next section, we will calculate explicit expressions for Green's functions in thermal equilibrium. In the course of doing so, we will

also see that the contribution $G_{\text{cor}}^{\lessgtr}$ describes initial correlations that can often be neglected.

1.5 Equilibrium Green's functions

In this section, we consider the thermal equilibrium situation and restrict ourselves to a single isolated subsystem S_n that is fully described by $\mathcal{H}_{S_n,0}$ and $\rho_{S_n,0}$, suppressing the index $S_n \in \{S, L_1, \dots L_{N_L}\}$ for brevity in this section. Note that this system is characterized by translational invariance in time. We will first calculate explicit expressions for standard time Green's functions, which will enter into the definition of observables in the steady state. Then, we will derive the equations of motion, which allow for a discussion of the contribution $G_{\text{cor}}^{\lessgtr}$ to Eq. (1.19).

Energy-dependent Green's functions

Substituting the time evolution of the field operator, Eq. (1.4), into the definition of the retarded and advanced Green's functions, we obtain

$$
\begin{aligned}
(G_0^{r,a})_{ij}(t,t') &= \mp\frac{\mathrm{i}}{\hbar}\Theta(\pm(t-t'))\langle\{c_i(t), c_j^\dagger(t')\}\rangle \\
&= \mp\frac{\mathrm{i}}{\hbar}\Theta(\pm(t-t'))\sum_{\alpha,\beta}(\phi_\alpha^{(0)})_i(\phi_\beta^{(0)})_j^* e^{-\mathrm{i}(E_\alpha(t-t_0)-E_\beta(t'-t_0))/\hbar}\underbrace{\langle\{a_\alpha, a_\beta^\dagger\}\rangle}_{\delta_{\alpha\beta}} \\
&= \mp\frac{\mathrm{i}}{\hbar}\Theta(\pm(t-t'))\sum_{\alpha}(\phi_\alpha^{(0)})_i(\phi_\alpha^{(0)})_j^* e^{-\mathrm{i}E_\alpha(t-t')/\hbar}.
\end{aligned} \tag{1.20}
$$

In compact matrix notation, the single-particle time evolution operator emerges:

$$
G_0^{r,a}(t,t') = \mp\frac{\mathrm{i}}{\hbar}\Theta(\pm(t-t'))e^{-\mathrm{i}H_0(t-t')/\hbar} \equiv G_0^{r,a}(t-t'). \tag{1.21}
$$

The retarded (advanced) Green's function—or propagator—thus has a clear meaning: It propagates the system through time under the dynamics imposed by the single-particle Hamiltonian H_0; however, it is non-zero only if the propagation from t' to t is forward (backward) in time. Thus, up to the prefactor $\mp\mathrm{i}/\hbar$, $(G_0^{r,a})_{ij}(t,t')$ is the probability amplitude $\langle i,t|j,t'\rangle$ for being in state $|i\rangle$ at time t given that the system has been in state $|j\rangle$ at some earlier (later) time $t' < t$ ($t' > t$).

The retarded equilibrium Green's function is translationally invariant in time as it should be for any quantity in the case of an equilibrium situation. It is thus convenient to change from the time domain to the energy domain by means of a Fourier transform,[11]

$$
X(E) \equiv \int_{-\infty}^\infty e^{\mathrm{i}Et/\hbar}X(t)\,\mathrm{d}t, \quad X(t) = \frac{1}{2\pi\hbar}\int_{-\infty}^\infty e^{-\mathrm{i}Et/\hbar}X(E)\,\mathrm{d}E,
$$

---

[11] Since it will always be clear from the context, we will not introduce different symbols for (i) energy-dependent (Green's) functions, (ii) (Green's) functions that explicitly depend on two times, and (iii) (Green's) functions that depend on a single time (difference), for the sake of clarity.

for any quantity X. Using the integral representation of the Heaviside step function,

$$\Theta(t) = -\frac{1}{2\pi i} \int_{-\infty}^{\infty} e^{-i\tilde{E}t/\hbar} \frac{1}{\tilde{E} + i0^+} \, d\tilde{E},$$

where $i0^+$ denotes an infinitesimal shift along the positive imaginary axis into the complex plane, we obtain from Eq. (1.21):

$$G_0^{r,a}(E) = \pm\frac{1}{2\pi\hbar} \int_{-\infty}^{\infty} \underbrace{\int_{-\infty}^{\infty} e^{i(E-H_0\mp\tilde{E})t/\hbar} \, dt}_{2\pi\hbar\delta(E-H_0\mp\tilde{E})} \frac{1}{\tilde{E} + i0^+} \, d\tilde{E}$$

$$= (E - H_0 \pm i0^+)^{-1}. \tag{1.22}$$

Following Ref. [Kad62], the energy-dependent greater and lesser Green's functions can be expressed through the retarded and advanced Green's functions. To this end, we first note that, as mentioned above, also the greater and lesser Green's functions may only depend on time differences in thermal equilibrium, $(G_0^{\lessgtr})_{ij}(t,t') \equiv (G_0^{\lessgtr})_{ij}(t-t')$. We then have

$$(G_0^<)_{ij}(t) = (G_0^<)_{ij}(t,0)$$

$$= \frac{i}{\hbar}\frac{1}{Z} \text{tr} \left(\underbrace{e^{-\beta(\mathcal{H}_0-\mu\mathcal{N})} c_j^\dagger(0) \overbrace{e^{\beta(\mathcal{H}_0-\mu\mathcal{N})}}^{1} e^{-\beta(\mathcal{H}_0-\mu\mathcal{N})}}_{\exp(\beta\mu) c_j^\dagger(i\hbar\beta)} c_i(t) \right)$$

$$= -e^{\beta\mu}(G_0^>)_{ij}(t, i\hbar\beta)$$

$$= -e^{\beta\mu}(G_0^>)_{ij}(t - i\hbar\beta),$$

where we used $[\mathcal{H}_0, \mathcal{N}] = 0$, the relation

$$c_j^\dagger(0)e^{-\beta\mu\mathcal{N}} = e^{-\beta\mu(\mathcal{N}-1)} c_j^\dagger(0),$$

and the cyclic property of the trace. Switching to the energy domain, we obtain the detailed balancing condition [Ram07],

$$G_0^<(E) = -e^{\beta\mu} \int_{-\infty-i\hbar\beta}^{\infty-i\hbar\beta} e^{iE(\tilde{t}+i\hbar\beta)/\hbar} G_0^>(\tilde{t}) \, d\tilde{t}$$

$$= -e^{-\beta(E-\mu)} \int_{-\infty}^{\infty} e^{iE\tilde{t}/\hbar} G_0^>(\tilde{t}) \, d\tilde{t} = -e^{-\beta(E-\mu)} G_0^>(E),$$

where we substituted the integration variable by $\tilde{t} = t - i\hbar\beta$ and used the analyticity of the integrand [Kad62, Ram07]. Using Eq. (1.16), we arrive at the famous fluctuation-dissipation theorem [Wim09a, Sch08], in compact matrix notation:

$$G_0^{\lessgtr}(E) = \mp\frac{G_0^r(E) - G_0^a(E)}{1 + e^{\pm\beta(E-\mu)}}. \tag{1.23}$$

Equations of motion and initial correlations

Using the equation of motion for the field operator, Eq. (1.3), the equations of motion for the lesser and greater Green's functions read

$$\mathrm{i}\hbar\partial_t(G_0^{\lessgtr})_{ij}(t,t') = \begin{cases} -\langle c_j^\dagger(t')\partial_t c_i(t)\rangle \\ +\langle \partial_t c_i(t) c_j^\dagger(t')\rangle \end{cases}$$

$$= -\frac{\mathrm{i}}{\hbar}\sum_k (H_0)_{ik} \begin{cases} -\langle c_j^\dagger(t') c_k(t)\rangle \\ +\langle c_k(t) c_j^\dagger(t')\rangle \end{cases} = \sum_k (H_0)_{ik}(G_0^{\lessgtr})_{kj}(t,t').$$

Together with Eq. (1.21), we therefore find, in compact matrix notation:

$$(\mathrm{i}\hbar\partial_t - H_0)G_0^{r,a}(t,t') = \delta(t-t')\mathrm{e}^{-\mathrm{i}H_0(t-t')/\hbar} = \delta(t-t')\cdot\mathbf{1}, \tag{1.24}$$

$$(\mathrm{i}\hbar\partial_t - H_0)G_0^{\lessgtr}(t,t') = \mathbf{0}, \tag{1.25}$$

where in the last step in Eq. (1.24) we set $t = t'$ due to the delta function. Eq. (1.24) can now be used to rewrite the term $G_{\mathrm{cor}}^{\lessgtr}$ that appears in Eq. (1.19), again suppressing the index S for clarity:

$$G_{\mathrm{cor}}^{\lessgtr}(t,t') = \int\int\int \left(\mathbf{1} + G^r(V+\Sigma^r)\right)\Big|_{(t,t_1)}$$

$$\times \left(\underbrace{(\mathrm{i}\hbar\partial_{t_1} - H_0)G_0^r(t_1,t_2)}_{\delta(t_1-t_2)\cdot\mathbf{1}}\right)G_0^{\lessgtr}(t_2,t_3)\left(\mathbf{1}+(V+\Sigma^a)G^a\right)\Big|_{(t_3,t')} \mathrm{d}t_1\,\mathrm{d}t_2\,\mathrm{d}t_3.$$

Due to the equilibrium property $G_0^r(t_1,t_2) = G_0^r(t_1-t_2)$, we may replace $\partial_{t_1} \to -\partial_{t_2}$ in this expression; then, integrating by parts, we find

$$G_{\mathrm{cor}}^{\lessgtr}(t,t') = \int\int \left(\mathbf{1}+G^r(V+\Sigma^r)\right)\Big|_{(t,t_1)}$$

$$\times \left(-\mathrm{i}\hbar(G_0^r(t_1,\tilde{t})G_0^{\lessgtr}(\tilde{t},t_3))\Big|_{\tilde{t}=-\infty}^{\tilde{t}=\infty} + \int G_0^r(t_1,t_2)(\underbrace{(\mathrm{i}\hbar\partial_{t_2}-H_0)G_0^{\lessgtr}(t_2,t_3)}_{\mathbf{0}})\,\mathrm{d}t_2\right)$$

$$\times \left(\mathbf{1}+(V+\Sigma^a)G^a\right)\Big|_{(t_3,t')} \mathrm{d}t_1\,\mathrm{d}t_3,$$

where we used $[H_0, G_0^r] = 0$ and Eq. (1.25). We are thus left with a boundary term evaluated at times $\tilde{t} = \pm\infty$, which is often neglected due to the decay of initial correlations at $\tilde{t} = -\infty$ over time [Dav93], i.e., the escape of initially occupied states through the leads as a transient phenomenon. However, there may exist localized states that—if initially occupied—are not able to leave the scattering region through the leads if they do not couple to the existing energy channels. Of course, in non-interacting systems, such localized states do not interfere with the current-carrying scattering states and therefore the current is unaffected, justifying the negligence of the boundary term; this is the situation we will be interested in in the following chapters. We will therefore omit a further discussion of this issue, which would be necessary in the case of interacting systems or even for the calculation of observables like

the local density in non-interacting systems. For a more detailed treatment, we refer the reader to Section 2.5.3 of Ref. [Wim09a] and references therein. Anyway, in the present work, we are exclusively concerned with steady state properties, where such a term—depending explicitly on absolute times instead of time differences—cannot contribute *by definition* as we will discuss in the next section.

Closing remark

Note that in contrast to lesser and greater Green's functions, the retarded and advanced Green's functions are already fully characterized by the spectrum of H_0. Moreover, Eqs. (1.20) through (1.22) hold for any form of the density matrix ρ_0 and are therefore not restricted to a situation of thermal equilibrium.[12] In the next section, we will make use of this fact when we express the local density of states through retarded and advanced Green's functions in a steady state situation where the leads—which in general are characterized by different chemical potentials and/or temperatures—are coupled through the scattering region[13]—a system which is in general out of equilibrium.

1.6 Observables in steady state

In this section, we turn to the definition of observables in terms of Green's functions. As mentioned before, we will be exclusively interested in steady state situations, where observables do not depend on time at all and the related quantities are therefore characterized by translational invariance in time. More explicitly, our very definition of the steady state is the *dependence of Green's functions on time differences only*.[14] Then, it is convenient to work in the energy domain instead of the time domain since convolutions in the time domain, as encountered in the Dyson equation, are transformed into simple products in the energy domain:

$$
\int \tilde{G}_A(t_1 - \tilde{t}) V_{AB} \tilde{G}_B(\tilde{t} - t_2) \, \mathrm{d}\tilde{t}
$$

$$
= \frac{1}{(2\pi\hbar)^2} \int \int \tilde{G}_A(E) V_{AB} \tilde{G}_B(E') \mathrm{e}^{-\mathrm{i}(Et_1 - E't_2)/\hbar} \underbrace{\int \mathrm{e}^{\mathrm{i}(E-E')\tilde{t}/\hbar} \, \mathrm{d}\tilde{t}}_{2\pi\hbar\delta(E-E')} \, \mathrm{d}E \, \mathrm{d}E'
$$

$$
= \frac{1}{2\pi\hbar} \int \tilde{G}_A(E) V_{AB} \tilde{G}_B(E) \mathrm{e}^{-\mathrm{i}E(t_1 - t_2)/\hbar} \, \mathrm{d}E \equiv \tilde{\gamma}(t_1 - t_2),
$$

---

[12] The (contour-ordered) Green's function (1.8) can as well be defined for an arbitrary density matrix; the explicit form of the (grand) canonical density matrix first enters the theory in the application of Wick's theorem in order to derive the Dyson equation.

[13] The time-independent single particle Hamiltonian corresponding to this non-equilibrium steady state situation is then formally given by $H_0 + V_\infty$ instead of H_0 only, where $V_\infty = V(t \to \infty)$ is the saturation value of the perturbation.

[14] This definition conforms to Ref. [Wim09a] and is stricter than other definitions commonly encountered in the literature, e.g., in Ref. [Ram07], where by definition "the dependence on the initial state is lost, and the time dependence is governed by external forces" in the steady state.

and thus

$$\tilde{\gamma}(E) = \int \tilde{\gamma}(\tilde{t}) \mathrm{e}^{\mathrm{i}E\tilde{t}/\hbar} \, \mathrm{d}\tilde{t} = \tilde{G}_A(E) V_{AB} \tilde{G}_B(E).$$

Here, $\tilde{G}_A$ and $\tilde{G}_B$ denote Green's functions and V_{AB} denotes one of the perturbation contributions V_S, V_{LS}, or V_{SL}. Note that by our definition of the steady state, the details of the transient process when the coupling between leads and scattering region is turned on cannot play a role; if V_{AB} exhibited an explicit time dependence, the expression $\tilde{\gamma}(t_1, t_2) \neq \tilde{\gamma}(t_1 - t_2)$ would not have the form of a convolution and would explicitly depend on two times. Therefore, only the stationary value of the perturbation contributes in the steady state.[15] In the steady state, the Hamiltonian $\mathcal{H} = \mathcal{H}_0 + \mathcal{H}'$ of our open quantum system consisting of a scatterer S and a number of leads L_l is thus time-independent. For convenience, we also absorb V_S and V_L into $\mathcal{H}_0$, $(H_0)_S + V_S \to H_S$, $(H_0)_L + V_L \to H_L$, without loss of generality, so that

$$\mathcal{H}_0 = \sum_L \underbrace{\sum_{ij}(H_L)_{ij}\psi^\dagger(i_L)\psi(j_L)}_{\mathcal{H}_L} + \underbrace{\sum_{ij}(H_S)_{ij}\psi^\dagger(i_S)\psi(j_S)}_{\mathcal{H}_S},$$

$$\mathcal{H}' = \sum_L \Big(\underbrace{\sum_{ij}(H_{LS})_{ij}\psi^\dagger(i_L)\psi(j_S)}_{\mathcal{H}_{LS}} + \underbrace{\sum_{ij}(H_{SL})_{ij}\psi^\dagger(i_S)\psi(j_L)}_{\mathcal{H}_{SL}} \Big), \qquad (1.26)$$

where for consistency we defined $H_{LS} \equiv V_{LS}$, $H_{SL} \equiv V_{SL}$, and $H_{SL} = H_{LS}^\dagger$ since H is hermitian. Here, we also assumed $V_{LL'} = 0$ for $L \neq L'$, which is natural and always possible for a sensible definition of the leads.[16] $\mathcal{H}_0$ describes the equilibrium steady state situation, whereas $\mathcal{H}$ describes the non-equilibrium steady state situation.

Before calculating the current through this system, let us summarize the two central matrix equations for Green's functions in the steady state, namely the Dyson equation,

$$G_S^{r,a}(E) = G_{S,0}^{r,a}(E) + G_{S,0}^{r,a}(E)\Sigma^{r,a}(E)G_S^{r,a}(E) = (E - H_S - \Sigma^{r,a}(E) \pm \mathrm{i}0^+)^{-1}, \qquad (1.27)$$

and the so-called Keldysh equation [Wim09a, Hau96],

$$G_S^{\lessgtr}(E) = G_S^r(E)\Sigma^{\lessgtr}(E)G_S^a(E), \qquad (1.28)$$

where $\Sigma^{r,a,\lessgtr} \equiv \sum_l \Sigma_l^{r,a,\lessgtr}$ and

$$\Sigma_l^{r,a,\lessgtr}(E) \equiv H_{SL_l} G_{L_l,0}^{r,a,\lessgtr}(E) H_{L_lS}. \qquad (1.29)$$

---

[15] Formally, this corresponds to a sudden switching on of the perturbation, $V(t) = V_\infty \Theta(t - t_0)$.
[16] The design of the leads is discussed in Section 2.1.

Current

In general, the current in lead L_l can be defined as expectation value of the derivative of the charge Q_l with respect to time,[17]

$$
\begin{aligned}
I_l(t) &\equiv \left\langle \frac{\mathrm{d}}{\mathrm{d}t} Q_l \right\rangle \equiv -e \operatorname{tr}\left(\rho_0 \frac{\mathrm{d}}{\mathrm{d}t}(\mathcal{N}_l)_{\mathcal{H}}(t) \right) = \frac{\mathrm{i}e}{\hbar} \operatorname{tr}\left(\rho_0 [(\mathcal{N}_l)_{\mathcal{H}}(t), \mathcal{H}] \right) \\
&= \frac{\mathrm{i}e}{\hbar} \operatorname{tr}\left(\rho_0 \mathcal{U}_{\mathcal{H}}^{\dagger}(t, t_0)[\mathcal{N}_l, \mathcal{H}]\mathcal{U}_{\mathcal{H}}(t, t_0) \right) \\
&= \frac{\mathrm{i}e}{\hbar} \sum_{ij} \left((H_{L_l S})_{ij} \operatorname{tr}\left(\rho_0 \psi_{\mathcal{H}}^{\dagger}(i_{L_l}, t)\psi_{\mathcal{H}}(j_S, t) \right) - (H_{SL_l})_{ji} \operatorname{tr}\left(\rho_0 \psi_{\mathcal{H}}^{\dagger}(j_S, t)\psi_{\mathcal{H}}(i_{L_l}, t) \right) \right) \\
&= e \sum_{ij} \left((H_{L_l S})_{ij} (G_{SL_l}^{<})_{ji}(t, t) - (H_{SL_l})_{ji} (G_{L_l S}^{<})_{ij}(t, t) \right) \\
&= e \operatorname{tr}\left(H_{L_l S} G_{SL_l}^{<}(t-t) - H_{SL_l} G_{L_l S}^{<}(t-t) \right) \\
&= \frac{e}{h} \int \operatorname{tr}\left(H_{L_l S} G_{SL_l}^{<}(E) - H_{SL_l} G_{L_l S}^{<}(E) \right) \mathrm{d}E \equiv I_l,
\end{aligned}
\tag{1.30}
$$

where we made use of the anticommutation relations for the field operators, $(-e)$ is the quantum of charge, and $\mathcal{N}_l = \sum_i \psi^{\dagger}(i_{L_l})\psi(i_{L_l})$ is the number operator in the lead. Thus, as expected, the current is indeed independent of time in the steady state. Suppressing the dependence on energy E in the following, we may use Eqs. (1.13) and (1.15) as well as the cyclic property of the trace to rewrite Eq. (1.30):

$$
\begin{aligned}
I_l &= \frac{e}{h} \int \operatorname{tr}\left(\underbrace{H_{SL_l}(G_{L_l,0}^{a} - G_{L_l,0}^{r})H_{L_l S}}_{\Sigma_l^a - \Sigma_l^r} G_S^{<} + \underbrace{H_{SL_l} G_{L_l,0}^{<} H_{L_l S}}_{\Sigma_l^{<}}(G_S^r - G_S^a) \right) \mathrm{d}E \\
&= \frac{e}{h} \int \operatorname{tr}\left(\mathrm{i}\Gamma_l (G_S^{<} + f_l(E)\underbrace{(G_S^r - G_S^a)}_{G_S^{>} - G_S^{<}}) \right) \mathrm{d}E,
\end{aligned}
\tag{1.31}
$$

where we defined $\Gamma_l \equiv \mathrm{i}(\Sigma_l^r - \Sigma_l^a) = \mathrm{i}(\Sigma_l^{>} - \Sigma_l^{<})$, used Eq. (1.23), and introduced the Fermi–Dirac distribution

$$
f_l(E) \equiv \left(1 + \mathrm{e}^{\beta_l(E - \mu_l)} \right)^{-1}.
$$

Using the Keldysh equation (1.28), we finally obtain

$$
\begin{aligned}
I_l &= \frac{e}{h} \int \operatorname{tr}\left(\mathrm{i}\Gamma_l (G_S^r \sum_{l'} \underbrace{\mathrm{i}f_{l'}(E)\Gamma_{l'}}_{\Sigma_{l'}^{<}} G_S^a + f_l(E) G_S^r \underbrace{(\Sigma^{>} - \Sigma^{<})}_{-\mathrm{i}\sum_{l'} \Gamma_{l'}} G_S^a) \right) \mathrm{d}E \\
&= \frac{e}{\hbar} \int \sum_{l'} T_{ll'}(E)(f_l(E) - f_{l'}(E)) \, \mathrm{d}E,
\end{aligned}
\tag{1.32}
$$

---

[17] In order for the steady state to be well defined, the leads are always assumed to act as (or be connected to) charge carrier reservoirs (i.e., the "battery") that are infinitely large so that their respective chemical potential does not change under current flow.

where we defined the transmission function[18] [Dat05]

$$T_{ll'}(E) \equiv \mathrm{tr}(\Gamma_l G_S^r \Gamma_{l'} G_S^a). \tag{1.33}$$

From Eq. (1.32), it is evident that the net current is carried solely by states close to the Fermi energy within an energy window that is determined by the temperatures and chemical potentials of the respective leads.

With the voltage[19] $V_l \equiv -\mu_l/e$, we obtain for the differential conductance:

$$\frac{\mathrm{d}I_l}{\mathrm{d}V_{l'}} = \begin{cases} \dfrac{e^2}{h} \displaystyle\int \frac{\mathrm{d}f_{l'}(E)}{\mathrm{d}E} \sum_{\tilde{l} \neq l} T_{l\tilde{l}}(E)\,\mathrm{d}E & \text{if } l = l', \\[3ex] -\dfrac{e^2}{h} \displaystyle\int \frac{\mathrm{d}f_{l'}(E)}{\mathrm{d}E} T_{ll'}(E)\,\mathrm{d}E & \text{if } l \neq l'. \end{cases} \tag{1.34}$$

If the temperature in lead $L_{l'}$ is sufficiently low so that the transmission function is nearly constant over the then narrow energy range that contributes to the integral in Eq. (1.34), we may approximate

$$\frac{\mathrm{d}I_l}{\mathrm{d}V_{l'}} \approx \begin{cases} \dfrac{e^2}{h} \displaystyle\sum_{\tilde{l} \neq l} T_{l\tilde{l}}(\mu_{l'}) \int \frac{\mathrm{d}f_{l'}(E)}{\mathrm{d}E}\,\mathrm{d}E = -\dfrac{e^2}{h} \sum_{\tilde{l} \neq l} T_{l\tilde{l}}(\mu_{l'}) & \text{if } l = l', \\[3ex] -\dfrac{e^2}{h} T_{ll'}(\mu_{l'}) \displaystyle\int \frac{\mathrm{d}f_{l'}(E)}{\mathrm{d}E}\,\mathrm{d}E = \dfrac{e^2}{h} T_{ll'}(\mu_{l'}) & \text{if } l \neq l', \end{cases}$$

and note that the approximation becomes exact at zero temperature.

Moreover, in the regime of linear response that is characterized by low temperatures and low bias voltages $V_{ll'} \equiv V_l - V_{l'}$, we may employ the same approximation in Eq. (1.32):

$$I_l \approx \frac{e}{h} \sum_{l'} T_{ll'}(E_F) \underbrace{\int (f_l(E) - f_{l'}(E))\,\mathrm{d}E}_{\mu_l - \mu_{l'}} = \sum_{l'} G_{ll'}(V_{l'} - V_l),$$

with the Fermi energy $E_F \approx \mu_l \approx \mu_{l'}$ and the linear conductance

$$G_{ll'} \equiv \frac{e^2}{h} T_{ll'}(E_F).$$

In the following chapters of this thesis, we will focus on the calculation of the transmission function for various system types. Nevertheless, we conclude this section by summarizing additional quantities that can be expressed in terms of Green's functions and may in principle be calculated from the technique developed in the next chapter.

---

[18] This formula not only strongly resembles the Kubo formula for quantum conductance, but is also equivalent; see Ref. [Nik01] for details.

[19] For the remainder of this work, V denotes voltages and must not be confused with the perturbation component in the leads, which has already been absorbed into H in Eq. (1.26).

Spectral density and local density of states

The spectral density (or spectral weight function) $A(E)$ corresponding to the Hamiltonian H can be defined as

$$A(E) \equiv 2\pi\delta(E - H) = \mathrm{i}\left(\frac{1}{E - H + \mathrm{i}0^+} - \frac{1}{E - H - \mathrm{i}0^+}\right) = \mathrm{i}\big(G^r(E) - G^a(E)\big),$$

where we used the Sokhotsky–Weierstrass theorem,

$$\frac{1}{E \pm \mathrm{i}0^+} = \mathcal{P}\frac{1}{E} \mp \mathrm{i}\pi\delta(E),$$

where $\mathcal{P}$ is the Cauchy principal value integral. The spatially resolved density of states (DOS), also called local density of states (LDOS), is then given by the diagonal elements,

$$d_i(E) \equiv \underbrace{\sum_\alpha \delta(E - E_\alpha)\,|(\varphi_\alpha)_i|^2}_{\text{DOS}} = \frac{1}{2\pi}A_{ii}(E) = -\frac{1}{\pi}\operatorname{Im} G^r_{ii}(E), \tag{1.35}$$

where $H\varphi_\alpha = E_\alpha\varphi_\alpha$. Note that if $|i\rangle$ contains internal degrees of freedom, $d_i(E)$ not only is position-resolved but also resolves all these internal degrees of freedom.

Local density

In single particle quantum mechanics on a continuous basis, the probability density of a (spinless) particle in state $|\varphi\rangle$ is given as expectation value

$$|\varphi(\mathbf{x})|^2 = \langle\varphi|\mathbf{x}\rangle\langle\mathbf{x}|\varphi\rangle$$

of the single particle density operator $|\mathbf{x}\rangle\langle\mathbf{x}|$. In second quantization, the corresponding operator $\psi^\dagger(\mathbf{x})\psi(\mathbf{x})$ is obtained following the usual prescription (see Eqs. (1.1) and (1.2)) and its expectation value is thus simply given by a diagonal element of the lesser Green's function evaluated at equal times.

Analogously, we can define the spin density operator[20] for a particle with spin $s \in \{\uparrow, \downarrow\}$:

$$\hat{n}^\nu(\mathbf{x}_i) \equiv \sum_{ss'} \sigma^\nu_{ss'}|\mathbf{x}_i, s\rangle\langle\mathbf{x}_i, s'|,$$

where we identify $\uparrow$ with 1 and $\downarrow$ with 2 for matrix elements of the Pauli matrices σ^ν, $\nu \in \{0, x, y, z\}$ and $\sigma^0 = \mathbf{1}_{2\times 2}$, so that the local charge density is included via $\nu = 0$. The expectation value of the corresponding operator in second quantization is then given by

---

[20] Since we chose a discrete basis in position space rather than a continuum, we deal here with probabilities rather than probability densities. Nevertheless, we will continue to use the term "density" in the following. Furthermore, we omit any inconvenient normalization constants that originate from the transition from continuum to lattice space (see Appendix A of Ref. [Wim09a] for details).

$n^\nu(\mathbf{x}_i) = \int n^\nu(\mathbf{x}_i, E)\, \mathrm{d}E$, where

$$n^\nu(\mathbf{x}_i, E) \equiv -\frac{\mathrm{i}}{2\pi} \sum_{ss'} \sigma^\nu_{ss'} \langle \mathbf{x}_i, s' | \hat{G}^<(E) | \mathbf{x}_i, s \rangle$$

and we introduced the operator $\hat{G}^<(E)$ corresponding to the matrix $G^<(E)$ along the lines of Eqs. (1.1) and (1.2). Similar expressions may be defined analogously for additional internal degrees of freedom if present.

For an isolated subsystem in thermal equilibrium described by the Fermi–Dirac distribution $f(E)$, Eq. (1.23) may be used to relate the local density (charge ($\nu = 0$) or spin ($\nu = 1, 2, 3$)) to the LDOS,

$$n^\nu(\mathbf{x}_i) = \int f(E) \underbrace{\frac{1}{2\pi} \sum_{ss'} \sigma^\nu_{ss'} \langle \mathbf{x}_i, s' | \hat{A}(E) | \mathbf{x}_i, s \rangle}_{\equiv d^\nu(\mathbf{x}_i, E)}\, \mathrm{d}E,$$

in analogy to Eq. (1.35). Here, we also introduced the operator $\hat{A}(E)$ corresponding to the matrix $A(E)$.

Local current density

By correspondence to the classical expression $\mathbf{j} = n\mathbf{v}$, the local current density operator can be defined as $\hat{\mathbf{j}}^\nu(\mathbf{x}_i) \equiv \frac{1}{2}\{\hat{n}^\nu(\mathbf{x}_i), \hat{\mathbf{v}}\}$ for charge ($\nu = 0$) and spin ($\nu = 1, 2, 3$), where the anti-commutator symmetrizes the otherwise non-hermitian operator. Here, $\hat{\mathbf{v}} \equiv \mathrm{d}\hat{\mathbf{x}}/\mathrm{d}t = \mathrm{i}[\hat{H}, \hat{\mathbf{x}}]/\hbar$ denotes the velocity operator and $\hat{\mathbf{x}} = \sum_i \mathbf{x}_i |i\rangle\langle i|$ the position operator. We obtain

$$\hat{\mathbf{j}}^\nu(\mathbf{x}_i) = \frac{\mathrm{i}}{2\hbar} \sum_{j,s,s',\tilde{s}} \sigma^\nu_{ss'} (\mathbf{x}_j - \mathbf{x}_i)(H_{is',j\tilde{s}} |\mathbf{x}_i, s\rangle\langle\mathbf{x}_j, \tilde{s}| - H_{j\tilde{s},is} |\mathbf{x}_j, \tilde{s}\rangle\langle\mathbf{x}_i, s'|)$$

and thus $\mathbf{j}^\nu(\mathbf{x}_i) = \int \mathbf{j}^\nu(\mathbf{x}_i, E)\, \mathrm{d}E$ with

$$\mathbf{j}^\nu(\mathbf{x}_i, E) \equiv \frac{1}{2\pi\hbar} \sum_{j,s,s',\tilde{s}} (\mathbf{x}_j - \mathbf{x}_i)\, \mathrm{Re}\left(\sigma^\nu_{ss'} H_{is',j\tilde{s}} G^<_{j\tilde{s},is}(E)\right).$$

Chapter 2

Numerical implementation

With the transmission function, Eq. (1.33), we established an expression from which the current through the system under consideration can in principle be calculated. Central ingredients of this quantity are the self-energies of the leads, whose practical numerical calculation is so far unclear. We will thus take on where we left in Section 1.3 and begin this chapter by outlining how the leads can be modeled in order to facilitate the calculation of the self-energy. Having established the concrete design of the leads, we can then relate the Green's function formalism and in particular the transmission function to the scattering matrix formalism, which offers a much more intuitive interpretation of Eq. (1.33) as well as certain advantages for a numerical implementation. Subsequently, we turn to the actual calculation of the relevant Green's function elements using a variant of a well-established and highly efficient recursive scheme. The efficiency of this technique is due to the absence of interactions beyond a mean-field approximation and, concluding this chapter, we will shortly outline the changes to the theory developed so far that would emerge if generic interactions had been included.

2.1 Surface Green's function and self-energy of an isolated lead

A numerical treatment of quantum transport necessitates the description of the system under consideration through matrices of finite size. So far, the leads, which are assumed to extend to infinity, are described by a Hamiltonian matrix of infinite size; a truncation of this matrix would immediately destroy the open character of the quantum system, therefore rendering this naive approach inapplicable. Instead, a particular semi-infinite lead L, as depicted in Fig. 1.3, is usually modeled exhibiting a periodic, crystalline structure, i.e., an infinite sequence of identical unit cells L^z, $z \in \mathbb{N}_0$, of finite size (see Fig. 2.1(a)). Then, the full information about the lead is contained in the intra-cell matrix H_{uc} and the inter-cell coupling matrix H_c, which are independent of z due to the periodicity of the lead and whose elements are given by

$$\hat{H}_{L^z} = \sum_{ij} (H_{uc})_{ij} |i_{L^z}\rangle\langle j_{L^z}|, \qquad\qquad (H_{uc})_{ij} \equiv \langle i_{L^z}|\hat{H}|j_{L^z}\rangle,$$

$$\hat{H}_{L^z L^{z+1}} = \sum_{ij} (H_c)_{ij} |i_{L^z}\rangle\langle j_{L^{z+1}}| = (\hat{H}_{L^{z+1} L_z})^{\dagger}, \qquad\qquad (H_c)_{ij} \equiv \langle i_{L^z}|\hat{H}|j_{L^{z+1}}\rangle.$$

Further, Bloch states, which are characterized by a well-defined crystal momentum quantum number, can be defined according to Bloch's theorem [Blo29] in the corresponding infinite
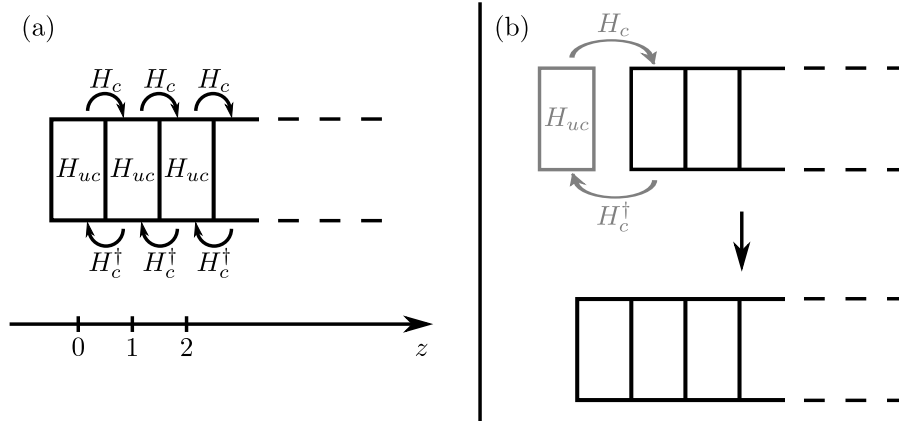
Figure 2.1: (a) A semi-infinite lead L is modeled as an infinite sequence of identical unit cells L^z, $z \in \mathbb{N}_0$, and is fully described by the intra-cell matrix H_{uc} and the inter-cell coupling matrix H_c, both of which are of finite size. The corresponding infinite lead is given by the straightforward extension of the series of units cells for negative values of z. (b) The semi-infinite lead is invariant under the addition of another unit cell according to Eq. (2.7).

lead that is obtained from the semi-infinite lead by extending the sequence of identical unit cells to negative values of z.

In addition, in realistic systems only a finite number of matrix elements of H_{SL} is non-zero so that the unit cell can always be chosen such that any lattice sites in the scattering region S only couple to the first unit cell L^0 of the lead, which we will refer to as the "surface" of the lead. The matrix product in Eq. (1.29) then only involves matrix elements of the Green's function that are located within the surface:[1]

$$\Sigma_l^r = H_{SL_l^0} g_l^r(E) H_{L_l^0 S},$$

where we defined the retarded surface Green's function

$$g_l^r(E) \equiv \left(G_{L_l,0}^r(E) \right)_{L_l^0}.$$

Due to the periodic structure of the lead, it is possible to derive an analytic expression for the surface Green's function. To this end, we will follow the approach by Sanvito et al. [San99]. This approach requires the coupling matrix that connects neighboring unit cells to be invertible. Since this requirement will not be fulfilled for the lattice structures considered later, in Section 2.3, we will introduce an effective description of the lead that remedies this problem and in addition offers increased performance of the algorithm presented later in Section 2.4. For the remainder of this section, we will again suppress the lead index as well as the dependence of the surface Green's function on energy for brevity.

In order to calculate the retarded surface Green's function, we essentially follow the general idea from Ref. [San99] however using an elegant argument from Ref. [Wim09a] that simplifies the derivation. In addition, we will change the terminology with respect to these references

---

[1] In what follows, we can restrict ourselves to the consideration of retarded quantities.

from left- and right-moving states to in- and out-moving states for a universal description of arbitrarily oriented leads in terms of a single expression for the retarded Green's function.

We start by considering the infinite lead that corresponds to the semi-infinite lead shown in Fig. 2.1(a). Since a given unit cell L^z only couples to cells L^{z-1} and L^{z+1}, the Hamiltonian of the infinite lead has a tridiagonal block matrix structure and the corresponding stationary Schrödinger equation can be written as

$$H_c^\dagger \Phi(z-1) + H_{uc}\Phi(z) + H_c\Phi(z+1) = E\Phi(z), \quad z \in \mathbb{Z}. \tag{2.1}$$

Due to Bloch's theorem [Blo29], the eigenvectors Φ have the form of a Bloch state,

$$\Phi(z) = n_k \phi(k)\mathrm{e}^{\mathrm{i}kz} \equiv \Phi_k(z), \tag{2.2}$$

where k is a longitudinal wave vector, the vector $\phi(k)$ is assumed to be normalized according to $\phi^\dagger(k)\phi(k) = 1$, and n_k is a normalization constant that will be fixed later. Substituting this Bloch ansatz into Eq. (2.1), we obtain an effective Schrödinger equation,

$$(H_c^\dagger \mathrm{e}^{-\mathrm{i}k} + H_{uc} + H_c\mathrm{e}^{\mathrm{i}k})\phi(k) = E\phi(k). \tag{2.3}$$

Numerically, the problem of finding the wavevectors k and the corresponding eigenvectors $\phi(k)$ for a fixed value of the energy E is most conveniently solved by considering the equivalent eigenvalue problem[2]

$$\begin{pmatrix} -H_c^{-1}(H_{uc} - E) & -H_c^{-1}H_c^\dagger \\ \mathbf{1} & \mathbf{0} \end{pmatrix} \begin{pmatrix} \phi(k) \\ \mathrm{e}^{-\mathrm{i}k}\phi(k) \end{pmatrix} = \mathrm{e}^{\mathrm{i}k} \begin{pmatrix} \phi(k) \\ \mathrm{e}^{-\mathrm{i}k}\phi(k) \end{pmatrix}. \tag{2.4}$$

Obviously, this equation is well-defined only if H_c is invertible, as mentioned above. Each of the solutions—commonly called "modes" or "channels"—can be classified into one of four categories according to Eq. (2.2) and—for propagating modes, i.e., $\mathrm{Im}\,k = 0$ (see below)—the group velocity

$$v \equiv \frac{1}{\hbar}\frac{\partial E(k)}{\partial k} = \frac{1}{\hbar}\frac{\partial}{\partial k}\Big(\phi^\dagger(k)(H_c^\dagger \mathrm{e}^{-\mathrm{i}k} + H_{uc} + H_c\mathrm{e}^{\mathrm{i}k})\phi(k)\Big)$$

$$= \frac{\mathrm{i}}{\hbar}\phi^\dagger(k)(H_c\mathrm{e}^{\mathrm{i}k} - H_c^\dagger \mathrm{e}^{-\mathrm{i}k})\phi(k) = -\frac{2}{\hbar}\mathrm{Im}\,(\phi^\dagger(k)H_c\mathrm{e}^{\mathrm{i}k}\phi(k)) \tag{2.5}$$

(where we have used the Hellmann–Feynman theorem[3] [Hel37, Fey39]):

- The *out-propagating* modes ϕ_n, $n = 1, \ldots, N$, are characterized by $\mathrm{Im}\,k_n = 0$ and $v_n > 0$, i.e., they propagate away from the surface in the direction of increasing z.

- The *in-propagating* modes $\phi_{\bar{n}}$, $n = 1, \ldots, N$, are characterized by $\mathrm{Im}\,k_{\bar{n}} = 0$ and

---

[2] Note that in contrast to the more common situation where the spectrum is calculated for a given value of the wavevector, here we have to solve the inverse problem where the possible wavevectors k that are compatible with a given value of the energy E are sought after, $H(k)\phi(k) = E\phi(k)$. The solutions $\phi(k)$ are thus not guaranteed to form a complete orthonormal set, since they are solutions for the same energy but different Hamiltonians, rather than for different energies and the same Hamiltonian.

[3] For $H(k)\phi(k) = E(k)\phi(k)$, we find $\partial_k\big(\phi^\dagger(k)H(k)\phi(k)\big) = \phi^\dagger(k)\big(\partial_k H(k)\big)\phi(k) + E(k)\partial_k\big(\phi^\dagger(k)\phi(k)\big)$ using the product rule for derivatives. The second term vanishes due to the normalization $\phi^\dagger(k)\phi(k) = 1$.

$v_{\bar{n}} < 0$, i.e., they propagate toward the surface in the direction of decreasing z. The number of in-propagating modes equals the number of out-propagating modes at a given energy since the energy dispersion is periodic beyond the first Brillouin zone and each band thus crosses the energy E an equal number of times with positive and negative slope [Wim09a, San99].[4]

- The *out-decaying* modes ϕ_n, $n = N + 1, \ldots, M$, are characterized by $\mathrm{Im}\, k_n > 0$, i.e., they decay away from the surface in the direction of increasing z.

- The *in-decaying* modes $\phi_{\bar{n}}$, $n = N + 1, \ldots, M$, are characterized by $\mathrm{Im}\, k_{\bar{n}} < 0$, i.e., they decay toward the surface in the direction of decreasing z.[5] The number of in-decaying modes equals the number of out-decaying modes at a given energy since Eq. (2.3) can be recast into a quadratic eigenvalue problem, $(H_c \lambda^2 + (H_{uc} - E)\lambda + H_c^\dagger)\phi(k) = 0$, where $\lambda \equiv \mathrm{e}^{\mathrm{i}k}$, or, after hermitian conjugation, $\phi^\dagger(k)(H_c \tilde{\lambda}^2 + (H_{uc} - E)\tilde{\lambda} + H_c^\dagger) = 0$, where $\tilde{\lambda} \equiv 1/\lambda^*$, so for each eigenvalue to a right eigenvector with $\mathrm{Im}\, k < 0$ there exists an eigenvalue to a left eigenvector with $\mathrm{Im}\, k > 0$ and vice versa [Wim09a, San99].

Degenerate propagating modes corresponding to the same eigenvalue $\lambda = \mathrm{e}^{\mathrm{i}k}$ and constituting the columns of a matrix $U_\lambda \equiv (\phi_{n_1}, \phi_{n_2}, \ldots, \phi_{\bar{n}_1}, \phi_{\bar{n}_2}, \ldots)$ can always be chosen such that the matrix

$$V_\lambda \equiv \mathrm{i}U_\lambda^\dagger (H_c \lambda - H_c^\dagger \lambda^*)U_\lambda, \tag{2.6}$$

which acts as a velocity operator in the subspace of degenerate states, is diagonal; this is true since V_λ is hermitian and can thus be diagonalized by means of a unitary transformation, and we will assume this choice in the following.[6] Further, the definition of the group velocity according to Eq. (2.5) is applicable to propagating modes only since for evanescent modes, the expression $(H_c \mathrm{e}^{\mathrm{i}k} - H_c^\dagger \mathrm{e}^{-\mathrm{i}k})$ is non-hermitian and the corresponding velocity would in general be complex. Instead, we formally assign a vanishing group velocity $v = 0$ to evanescent modes since these do not carry current.

We now employ the argument from Ref. [Wim09a]: As is clear from Fig. 2.1(a), the surface Green's function does not depend on the absolute position z of the surface. We can thus employ Eq. (1.27) for the coupling shown in Fig. 2.1(b),

$$g^r = (E - H_{uc} - H_c g^r H_c^\dagger + \mathrm{i}0^+)^{-1}, \tag{2.7}$$

and note at this point that Eq. (2.7) can serve as a strong consistency check of the numerical implementation for the calculation of the surface Green's function. With this equation, we can show that each eigenvector $\tilde{\phi}$ of the matrix $(g^r H_c^\dagger)$ with eigenvalue $\mathrm{e}^{\mathrm{i}\tilde{k}}$, $\tilde{k} \in \mathbb{C}$, is a solution to Eq. (2.4):

$$\mathrm{e}^{-\mathrm{i}\tilde{k}} H_c^\dagger \tilde{\phi} = (g^r)^{-1} \tilde{\phi} = (E - H_{uc} - H_c g^r H_c^\dagger)\tilde{\phi} = (E - H_{uc} - H_c \mathrm{e}^{\mathrm{i}\tilde{k}})\tilde{\phi},$$

---

[4] This is nothing else than the application of the mean value theorem of calculus to a periodic function.

[5] It is clear that the decaying (or *evanescent*) modes are not normalizable solutions of the infinite lead; however, they are solutions of Eq. (2.4) and become relevant for the semi-infinite lead as we will see below.

[6] This choice is not arbitrary; it is essential for the correct classification of degenerate states with different propagation direction. Moreover, even for states with the same direction of propagation, this choice is required if the Landauer formula, Eq. (2.9), is invoked to calculate the transmission function [Wim09a], and in order for the scattering matrix, Eq. (2.11), to be unitary [San99].

where we explicitly took the limit $i0^+ \times \tilde{\phi} \to 0$. Thus, the matrix $(g^r H_c^\dagger)$ can be written in its spectral representation,[7]

$$g^r H_c^\dagger = U \Lambda U^{-1}, \tag{2.8}$$

where the columns of U contain appropriate solutions of Eq. (2.4) with corresponding eigenvalues on the diagonal of the diagonal matrix Λ. As is done in Refs. [San99, Dat05], the "appropriate" solutions can be inferred from the retarded property of the Green's function, namely that it may only contain solutions that propagate or decay away from the surface.[8] Since each column of g^r is given as a linear combination of the columns of U, it is thus clear that the out-propagating and out-decaying modes constitute the columns of U with corresponding eigenvalues e^{ik} on the diagonal of the diagonal matrix Λ:

$$U = (\phi_1, \ldots, \phi_M), \quad \Lambda = \mathrm{diag}(e^{ik_1}, \ldots, e^{ik_M}).$$

Due to the property $g^r H_c^\dagger \Phi_k(z) = \Phi_k(z+1)$, the matrix $g^r H_c^\dagger$ is commonly called "transfer matrix" [Lee81a, Reu00] since it essentially propagates the Bloch wave from one unit cell to the next.

2.2 Scattering description in the Landauer–Büttiker formalism

Having obtained the surface Green's function of the leads, one can explicitly calculate the transmission function, Eq. (1.33). However, this formula still lacks physical intuition. It is therefore convenient to connect the NEGF formalism to the description of transport in non-interacting systems in terms of transmission amplitudes in the framework of the Landauer–Büttiker formalism [Lan57, Büt85], and therefore to show the equivalence of Eq. (1.33) to the Landauer formula,

$$T_{ll'}(E) = \mathrm{tr}(t_{ll'}^\dagger t_{ll'}) = \sum_{n,n'} |(t_{ll'})_{nn'}|^2, \tag{2.9}$$

which expresses the total transmission through the probabilities $|(t_{ll'})_{nn'}|^2$ for transmission from an in-propagating mode n' in lead $L_{l'}$ into an out-propagating mode n in lead L_l at energy E (again, we will suppress the dependence on energy in the following). The probability

---

[7] ..., provided that such a representation exists, i.e., U is invertible; however, a proof for this to be true is lacking [Wim09a]. Note that also in the formulation of Ref. [San99] such an inversion is required although it is not apparent at first glance since it is hidden in the implicit definition of the so-called dual vectors.

[8] In a bit more detail: According to the discussion below Eq. (1.21), the retarded Green's function of the *infinite* lead $(G_0^\infty)_{z0}$ describing the wave function in some unit cell z due to an excitation in the unit cell located at $z = 0$ would exhibit contributions that propagate or decay toward larger (smaller) values of z for $z > 0$ ($z < 0$) due to causality. $(G_0^\infty)_{00}$ is then given by requiring continuity. Since for a *semi-infinite* lead with the surface located at $z = 0$ as in Fig. 2.1(a) there are no cells with $z < 0$ and therefore no contributions that propagate or decay toward smaller values of z, continuity is required with cells $z > 0$ only and thus only solutions that propagate or decay away from the surface towards larger values of z contribute to $(G_0^{\infty/2})_{00}$. For an alternative approach based on contour integration in the complex plane that avoids using this argumentation for the construction of the surface Green's function, we refer the reader to Ref. [Wim09a].

amplitudes[9]

$$(t_{ll'})_{nn'} = \frac{i}{\hbar} \frac{1}{\sqrt{v_n v_{\bar{n}'}}} \phi_n^\dagger (\Gamma_l G_{L_l^0 L_{l'}^0}^r \Gamma_{l'} + i\Gamma_l \delta_{ll'}) \phi_{\bar{n}'} \tag{2.10}$$

constitute the elements of a matrix $t_{ll'}$ and in turn, these matrices constitute the blocks of a unitary scattering matrix S,[10]

$$S = \begin{pmatrix} t_{11} & \ldots & t_{1N_L} \\ \ldots & \ldots & \ldots \\ t_{N_L 1} & \ldots & t_{N_L N_L} \end{pmatrix}, \tag{2.11}$$

where N_L is the number of leads. For an excellent presentation of the rather involved derivation of Eq. (2.10), starting from the scattering wave function of the system, we refer the reader to Appendix C of Ref. [Wim09a]. Here, we restrict ourselves to showing the equivalence of Eqs. (1.33) and (2.9)—also following Ref. [Wim09a]—for calculating the transmission between two leads, $l \neq l'$, taking Eq. (2.10) as a definition.

To this end, we reconsider Eq. (2.4) for out-propagating and out-decaying modes,

$$(E - H_{uc})\lambda_n \phi_n = (H_c \lambda_n^2 + H_c^\dagger)\phi_n,$$

where $\lambda_n \equiv e^{ik_n}$, and combine this equation with the adjoint,

$$\phi_{n'}^\dagger \lambda_{n'}^* (E - H_{uc}) = \phi_{n'}^\dagger (H_c^\dagger (\lambda_{n'}^*)^2 + H_c),$$

to give

$$\left[i\phi_{n'}^\dagger (H_c \lambda_n - H_c^\dagger \lambda_{n'}^*) \phi_n \right] \times \left[1 - \lambda_n \lambda_{n'}^* \right] = 0.$$

The expression in the second pair of brackets vanishes if and only if both modes n and n' are propagating and $\lambda_n = \lambda_{n'}$. In this case, the group velocity is recovered in the first pair of brackets.[11] In all other cases, the expression in the first bracket has to vanish. Since we assigned $v_n = 0$ for evanescent modes, we can thus write

$$i\phi_{n'}^\dagger (H_c \lambda_n - H_c^\dagger \lambda_{n'}^*) \phi_n = \hbar v_n \delta_{nn'}.$$

---

[9] Any such relation connecting transmission probability amplitudes with Green's functions is generally called "Fisher–Lee relation" after Fisher and Lee, who were first to derive such a relation [Fis81]. We also mention that for the actual calculation in the later chapters we use the expression for the transmission amplitudes given in Ref. [San99], while for showing the connection between the NEGF and scattering formalisms, Eq. (2.10) is more convenient. Of course, both expressions are equivalent [Wim09a].

[10] The diagonal blocks of the scattering matrix describe reflection within a single lead instead of transmission between two different leads and therefore commonly the notation r_{ll} is used for the diagonal elements instead of t_{ll}. Further, in the presented form, the scattering matrix is expressed in terms of current amplitudes rather than wave amplitudes—a prerequisite for the S-matrix being unitary [Dat05, Sto88], expressing the conservation of current—i.e., it connects asymptotically free states in the leads, Eq. (2.2), that are normalized to unit flux, $n_k = 1/\sqrt{|v|}$, where the group velocity v is given by Eq. (2.5).

[11] Note that we chose degenerate eigenvectors to diagonalize Eq. (2.6).

Using this as well as Eq. (2.8),

$$g^r H_c^\dagger = U \Lambda U^{-1} = \sum_{n=1}^M \phi_n \lambda_n \tilde{\phi}_n^\dagger = (H_c g^a)^\dagger,$$

where we denoted the n-th row of U^{-1} as $\tilde{\phi}_n^\dagger$, we can now rewrite:

$$
\begin{aligned}
\Gamma &= \mathrm{i}(H_c g^r H_c^\dagger - H_c g^a H_c^\dagger) \\
&= \mathrm{i} \sum_{n=1}^M \Big(\underbrace{\sum_{m=1}^M \tilde{\phi}_m \phi_m^\dagger}_{1} H_c \phi_n \lambda_n \tilde{\phi}_n^\dagger - \tilde{\phi}_n \lambda_n^* \phi_n^\dagger H_c^\dagger \underbrace{\sum_{m=1}^M \phi_m \tilde{\phi}_m^\dagger}_{1} \Big) \\
&= \sum_{n=1}^M \sum_{m=1}^M \tilde{\phi}_m \underbrace{\mathrm{i}\phi_m^\dagger (H_c \lambda_n - H_c^\dagger \lambda_m^*) \phi_n}_{\hbar v_n \delta_{nm}} \tilde{\phi}_n^\dagger \\
&= \sum_{n=1}^N \tilde{\phi}_n \hbar |v_n| \tilde{\phi}_n^\dagger = \sum_{n=1}^N \tilde{\phi}_{\bar{n}} \hbar |v_{\bar{n}}| \tilde{\phi}_{\bar{n}}^\dagger,
\end{aligned}
$$

where the last equality follows in analogy noting that the advanced surface Green's function is given by $g^a H_c^\dagger = \bar{U} \bar{\Lambda} \bar{U}^{-1}$, where $\bar{U}$ and $\bar{\Lambda}$ are composed of in-propagating and in-decaying solutions. By multiplication from the left and using the relation $\phi_m^\dagger \tilde{\phi}_n = \phi_{\bar{m}}^\dagger \tilde{\phi}_{\bar{n}} = \delta_{nm}$, we further find

$$\phi_m^\dagger \Gamma = \hbar |v_m| \tilde{\phi}_m^\dagger \quad \text{and} \quad \phi_{\bar{m}}^\dagger \Gamma = \hbar |v_{\bar{m}}| \tilde{\phi}_{\bar{m}}^\dagger,$$

which highlights the role of Γ as velocity (or current) operator in the lead [Wim09a],

$$\phi_m^\dagger \Gamma \phi_n = \hbar |v_m| \delta_{nm}, \tag{2.12}$$

and analogous for in-propagating modes. Thus, we finally obtain

$$\Gamma = \sum_{n=1}^N \Gamma \frac{\phi_n \phi_n^\dagger}{\hbar |v_n|} \Gamma = \sum_{n=1}^N \Gamma \frac{\phi_{\bar{n}} \phi_{\bar{n}}^\dagger}{\hbar |v_{\bar{n}}|} \Gamma,$$

where we used $\Gamma = \Gamma^\dagger$. This expression can now be substituted into Eq. (1.33) to show the equivalence of the NEGF formalism and the scattering description in the Landauer–Büttiker formalism:

$$
\begin{aligned}
T_{ll'}(E) &= \mathrm{tr}\left(\Gamma_l G_{L_l^0 L_{l'}^0}^r \Gamma_{l'} G_{L_{l'}^0 L_l^0}^a \right) \\
&= \mathrm{tr}\left(\sum_{n=1}^{N_l} \Gamma_l \frac{\phi_n^{(l)} (\phi_n^{(l)})^\dagger}{\hbar |v_n^{(l)}|} \Gamma_l G_{L_l^0 L_{l'}^0}^r \sum_{n'=1}^{N_{l'}} \Gamma_{l'} \frac{\phi_{\bar{n}'}^{(l')} (\phi_{\bar{n}'}^{(l')})^\dagger}{\hbar |v_{\bar{n}'}^{(l')}|} \Gamma_{l'} G_{L_{l'}^0 L_l^0}^a \right) \\
&= \sum_{n=1}^{N_l} \sum_{n'=1}^{N_{l'}} \underbrace{\frac{1}{\hbar^2 |v_n^{(l)}| |v_{\bar{n}'}^{(l)}|} \left((\phi_n^{(l)})^\dagger \Gamma_l G_{L_l^0 L_{l'}^0}^r \Gamma_{l'} \phi_{\bar{n}'}^{(l')} \right) \left((\phi_{\bar{n}'}^{(l')})^\dagger \Gamma_{l'} G_{L_{l'}^0 L_l^0}^a \Gamma_l \phi_n^{(l)} \right)}_{|(t_{ll'})_{nn'}|^2},
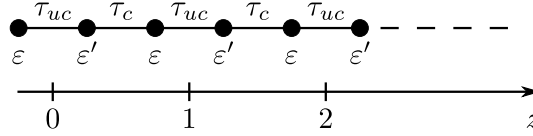\end{aligned}
$$

Figure 2.2: A simple one-dimensional lattice structure whose coupling matrix H_c is not invertible, see Eq. (2.13).

where we reintroduced the lead indices l and l', and formally defined the scattering region to include the first unit cell of each lead. In the special case where $\phi_n = \phi_{\bar{n}}$ and $\Gamma \phi_n = \hbar |v_n| \phi_n$, the expression for the transmission amplitudes reduces to the familiar form encountered in textbooks such as Ref. [Dat05].

Expressing transport quantities in terms of transmission amplitudes rather than invoking Eq. (1.33) has several advantages besides the intuitive interpretation the scattering formalism offers. First, the unitarity of the scattering matrix S serves as a strong consistency check for the implementation of the transport algorithm. Second, although not directly observable, the scattering matrix offers additional information about the system since it resolves the total transmission into individual scattering channels that can easily be inspected. Finally, additional observables, such as the Fano factor $F = \text{tr}\left(T(1 - T)\right)/\text{tr}(T)$, where $T = t_{ll'}^\dagger t_{ll'}$ [Two06], or in general the full counting statistics, i.e., the momenta of the transmission distribution $\text{tr}(T)^n$ [Naz94], are easily obtained from the scattering matrix.

2.3 Effective description of leads with non-invertible inter-cell coupling matrices

For lattice structures other than a simple square lattice, the issue of singular inter-cell coupling matrices H_c mentioned in Section 2.1 is quite generic and will also be relevant for the lattice structures considered later. We therefore introduce a simple prescription how to resolve this issue. The general idea of this method is based on the observation that in most cases when H_c is singular, the reason is that there exist lattice sites in cell L^z that do not couple to cell L^{z-1}, as in the example shown in Fig. 2.2;[12] there, the lead is defined by matrices that can be parameterized as

$$H_{uc} = \begin{pmatrix} \varepsilon & \tau_{uc} \\ \tau_{uc}^* & \varepsilon' \end{pmatrix}, \quad H_c = \begin{pmatrix} 0 & 0 \\ \tau_c & 0 \end{pmatrix}, \tag{2.13}$$

where $\varepsilon, \varepsilon' \in \mathbb{R}$ in order for the Hamiltonian to be hermitian and $\tau_{uc}, \tau_c \in \mathbb{C}$. Oviously, H_c is not invertible in this case. A straightforward approach to resolving this issue is to find an effective description of the lead that does not contain such lattice sites that do not couple to the previous unit cell. This is achieved by formally decomposing the unit cell into two

---

[12] Besides, there exist other cases where H_c is singular; for a discussion and an alternative approach on how to calculate the surface Green's function in such cases, we refer to Ref. [Roc06].
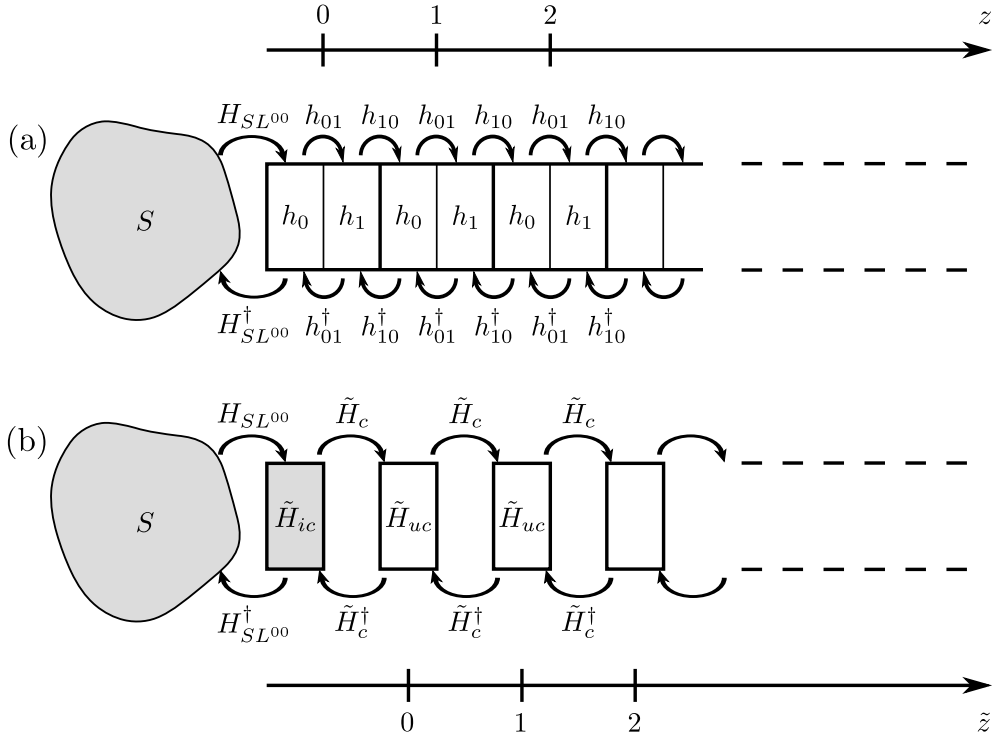
Figure 2.3: (a) Decomposition of unit cells (thick lines) into subcells (thin lines) according to Eq. (2.14) yielding a doubly-periodic structure for the lead that terminates at $z = 0$. The subcell described by h_1 located within the unit cell at position z neither couples to the previous unit cell located at $z - 1$ nor to the scattering region S. (b) The effective lead resulting from the elimination of the subcells described by h_1 again exhibits a singly-periodic structure. Note that the effective lead terminates at $z = 1$ (or $\tilde{z} = 0$) and is coupled to the scattering region via an interface cell at $z = 0$ described by $\tilde{H}_{ic}$.

subcells,[13]

$$H_{uc} = \begin{pmatrix} h_0 & h_{01} \\ h_{01}^\dagger & h_1 \end{pmatrix}, \quad H_c = \begin{pmatrix} \mathbf{0} & \mathbf{0} \\ h_{10} & \mathbf{0} \end{pmatrix}, \tag{2.14}$$

as shown in Fig. 2.3(a), that leads to an effective lead structure exhibiting a doubly-periodicity. Here, lattice sites described by h_1 neither couple to the previous unit cell nor to the scattering region; they may be eliminated from the description by taking them into account in an effective direct coupling between lattice sites described by h_0: Denoting the wave function in the lead as $\Psi(z) \equiv (\Psi_0(z), \Psi_1(z))^\mathsf{T}$ and the wave function in the scattering region as Ψ_S, we

---

[13] This decomposition is always possible, since structures not containing such lattice sites that do not couple to the previous unit cell (such as a simple square lattice) can be trivially included into this description via the choice $h_0 = h_1 = H_{uc}$ and $h_{01} = h_{10} = H_c$.

find:

$$h_{01}^\dagger \Psi_0(z) + h_1 \Psi_1(z) + h_{10} \Psi_0(z+1) = E\Psi_1(z) \text{ for } z \geq 0,$$
$$h_{10}^\dagger \Psi_1(z-1) + h_0 \Psi_0(z) + h_{01} \Psi_1(z) = E\Psi_0(z) \text{ for } z > 0, \text{ and}$$
$$H_{SL^{00}}^\dagger \Psi_S + h_0 \Psi_0(0) + h_{01} \Psi_1(0) = E\Psi_0(0).$$

Here, L^{00} denotes the subcell of the surface of the lead that directly couples to the scattering region. The first of these equations can be solved for $\Psi_1(z)$ and then be substituted into the two remaining equations to give

$$\tilde{H}_c^\dagger \Psi_0(z-1) + \tilde{H}_{uc} \Psi_0(z) + \tilde{H}_c \Psi_0(z+1) = E\Psi_0(z) \text{ for } z > 0, \text{ and}$$
$$H_{SL^{00}}^\dagger \Psi_S + \tilde{H}_{ic} \Psi_0(0) + \tilde{H}_c \Psi_0(1) = E\Psi_0(0),$$

where

$$\tilde{H}_{uc} \equiv \theta_{10}^\dagger + h_0 + \theta_{01},$$
$$\tilde{H}_c \equiv h_{01}(E - h_1)^{-1} h_{10},$$
$$\tilde{H}_{ic} \equiv h_0 + \theta_{01},$$
$$\theta_{ij} \equiv h_{ij}(E - h_1)^{-1} h_{ij}^\dagger. \tag{2.15}$$

These equations describing the coupling of the scattering region to the effective lead (see Fig. 2.3(b)) are well-defined if the energy parameter E is chosen such that $(E - h_1)$ is invertible; since h_1 is hermitian, this is always the case when E does not coincide with one of the eigenvalues of h_1. In the later chapters, we will identify such isolated singularities in the parameter space of the energy E for the particular lattice structures under consideration. For the case of $\tilde{H}_c$ still being singular—which will not be the case for the lattice structures considered in this work—there exist alternative ways to construct the surface Green's function, either by a more elaborate regularization procedure [Roc06, Run08] or directly by solving the generalized eigenvalue problem corresponding to Eq. (2.4) [Wim09a]; the latter however was found to be rather unstable under some circumstances [Roc06].

2.4 The Recursive Green's Function (RGF) algorithm

In order to determine the scattering matrix, the calculation of the lead surface components of the system Green's function is needed (see Eq. (2.10)). In principle, this can be achieved by direct inversion using the Dyson equation,

$$\tilde{G}^r = (\mathbf{1} - \tilde{G}_0^r \tilde{V})^{-1} \tilde{G}_0^r,$$

where

$$
\tilde{G}_0^r \equiv \begin{pmatrix} \tilde{G}_{\tilde{S},0}^r & & & \\ & g_1^r & & \\ & & \ddots & \\ & & & g_{N_L}^r \end{pmatrix}, \quad \tilde{V} \equiv \begin{pmatrix} & \tilde{H}_c^{(1)} & \cdots & \tilde{H}_c^{(N_L)} \\ (\tilde{H}_c^{(1)})^\dagger & & & \\ \vdots & & & \\ (\tilde{H}_c^{(N_L)})^\dagger & & & \end{pmatrix},
$$

and $\tilde{G}_{\tilde{S},0}^r \equiv (E - H_{\tilde{S}} + \mathrm{i}0^+)^{-1}$, where $\tilde{S}$ is the effective scattering region that contains the proper scattering region S as well as the interface cells of the leads, see Fig. 2.4. However, due to the size of $\tilde{S}$, this direct approach is usually numerically not feasible, both in terms of computing time and memory. An efficient way is based on the facts that (i) in order to evaluate observables it is not necessary to calculate the full Green's function matrix but rather some particular matrix elements thereof, and (ii) for practical purposes, the matrix $H_{\tilde{S}}$ is usually sparse, i.e., most of its entries are zero due to the local character of the coupling between atomic sites within a tight binding model.[14] Then, the scattering region S can be formally decomposed into layers S_s, $s = 1, \ldots, N_S$, so that the Hamiltonian of the scattering region can be written in block-tridiagonal form:

$$
H_S = \begin{pmatrix} H_1 & H_{1,2} & & & \\ H_{2,1} & H_2 & H_{2,3} & & \\ & \ddots & \ddots & \ddots & \\ & & H_{N_S-1,N_S-2} & H_{N_S-1} & H_{N_S-1,N_S} \\ & & & H_{N_S,N_S-1} & H_{N_S} \end{pmatrix}, \tag{2.16}
$$

where $H_{s,s'} = H_{s',s}^\dagger$ and we introduced the notation $H_s \equiv H_{S_s}$, $H_{s,s'} \equiv H_{S_s,S_{s'}}$; below, we will also use the notation $T_s^\dagger \equiv (T_{1,s}^\dagger, \ldots, T_{N_L,s}^\dagger)$, where $T_{l,s} \equiv H_{L_l^{00}S_s} = H_{S_s L_l^{00}}^\dagger$.

We can now iteratively build up the whole system by repeatedly using the Dyson equation for the individual layers as we will show in the following. Since we will only consider retarded Green's functions, we will suppress the upper index r for brevity, and we will also absorb $E \leftarrow E + \mathrm{i}0^+$. In principle, the infinitesimal shift $\mathrm{i}0^+$ can be taken care of in the implementation of the algorithm presented below by means of a corresponding parameter that is very small compared to the relevant energy scales in the system as is done for example in Ref. [Krs02]. This parameter has to be tuned in a controlled manner to ensure proper convergence. However, in practice this inconvenient handle is hardly necessary as it will be absorbed by the imaginary part of the self-energy, which is of finite size if there are any propagating states present in the lead [Wim09a].

---

[14] Physically, the off-diagonal matrix elements, which describe hopping between two atomic sites on the lattice, are determined from integrals involving products of the orbital wavefunctions located at the corresponding sites. Since these wavefunctions decay exponentially, only hopping integrals between nearest (and sometimes between next-nearest) neighbors are commonly taken into account while hopping between distant atomic sites is neglected.
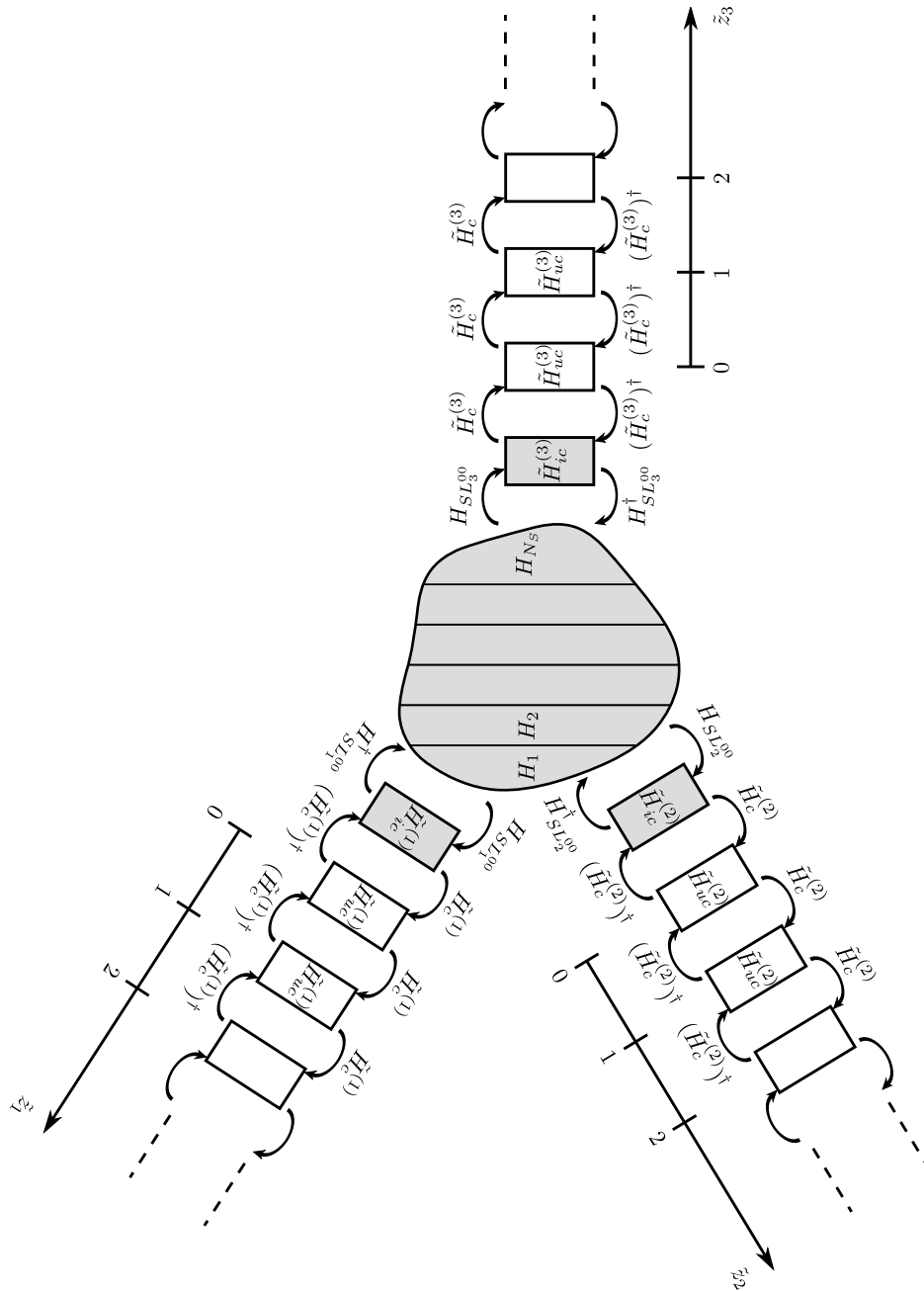
Figure 2.4: A detailed sketch of the effective system from which the surface components of the Green's function are calculated, shown for the case $N_L = 3$. The effective scattering region $\tilde{S}$, which is composed of the proper scattering region S and the interface cells of the leads, is shaded gray. A particularly simple choice of layers S_s, $s = 1, \ldots, N_S$, described by Eq. (2.16), is also shown.

Connecting the interface cell to the lead surface

The initial step in the iterative scheme can be depicted in the following way:
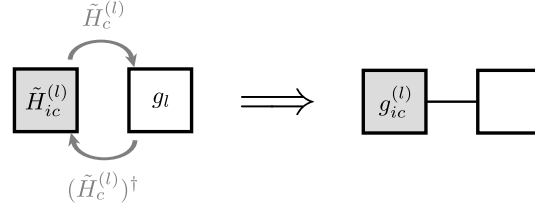
Analogous to the derivation of Eq. (2.7), we find the Green's function matrix within the interface cell in the presence of the lead,

$$g_{ic}^{(l)} = \left(E - \tilde{H}_{ic}^{(l)} - \tilde{H}_c^{(l)} g_l (\tilde{H}_c^{(l)})^\dagger \right)^{-1}.$$

Connecting the first layer

The coupling of the first layer has the following structure:
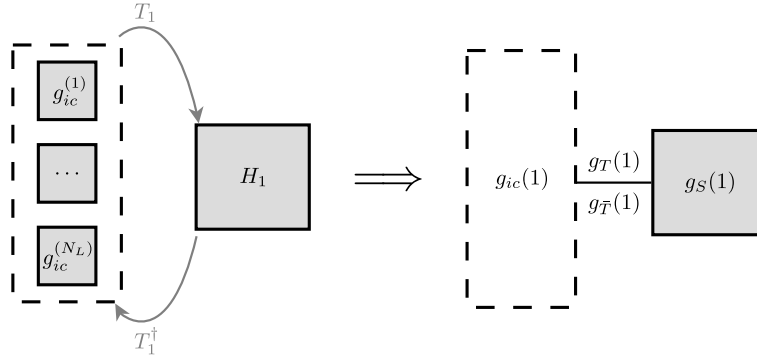
To connect the first layer S_1 of the proper scattering region S to the appropriate interface cells, we solve the Dyson equation $g(1) = (\mathbf{1} - g_0(1)V(1))^{-1} g_0(1)$, where

$$g_0(1) \equiv \begin{pmatrix} g_{ic}(0) & \mathbf{0} \\ \mathbf{0} & (E - H_1)^{-1} \end{pmatrix}, \qquad V(1) \equiv \begin{pmatrix} \mathbf{0} & T_1 \\ T_1^\dagger & \mathbf{0} \end{pmatrix}, \qquad g_{ic}(0) \equiv \begin{pmatrix} g_{ic}^{(1)} & & \\ & \ddots & \\ & & g_{ic}^{(N_L)} \end{pmatrix},$$
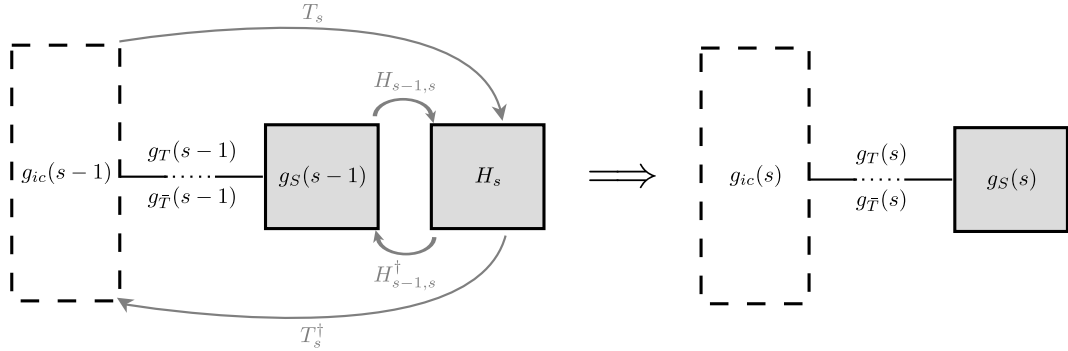
and

$$g(1) \equiv \begin{pmatrix} g_{ic}(1) & g_T(1) \\ g_{\bar{T}}(1) & g_S(1) \end{pmatrix},$$

and we find (see Appendix A)

$$
\begin{aligned}
g_S(1) &= \left(E - H_1 - T_1^\dagger g_{ic}(0) T_1\right)^{-1}, \\
g_T(1) &= g_{ic}(0) T_1 g_S(1), \\
g_{\bar{T}}(1) &= g_S(1) T_1^\dagger g_{ic}(0), \\
g_{ic}(1) &= g_{ic}(0) + g_{ic}(0) T_1 g_{\bar{T}}(1).
\end{aligned}
$$

Connecting the remaining layers ("forward sweep")

The iterative connection of the remaining layers proceeds according to this scheme:

To connect layer $S_s, s \in \{2, \ldots, N_S\}$, to the previous layer S_{s-1} and to the appropriate interface cells, we solve the Dyson equation $g(s) = \left(\mathbf{1} - g_0(s) V(s)\right)^{-1} g_0(s)$, where

$$
g_0(s) = \begin{pmatrix} g_{ic}(s-1) & g_T(s-1) & \mathbf{0} \\ g_{\bar{T}}(s-1) & g_S(s-1) & \mathbf{0} \\ \mathbf{0} & \mathbf{0} & (E - H_s)^{-1} \end{pmatrix}, \qquad V(s) \equiv \begin{pmatrix} \mathbf{0} & \mathbf{0} & T_s \\ \mathbf{0} & \mathbf{0} & H_{s-1,s} \\ T_s^\dagger & H_{s-1,s}^\dagger & \mathbf{0} \end{pmatrix},
$$

and

$$
g(s) \equiv \begin{pmatrix} g_{ic}(s) & \cdot & g_T(s) \\ \cdot & \cdot & \cdot \\ g_{\bar{T}}(s) & \cdot & g_S(s) \end{pmatrix}.
$$

The matrix elements indicated by "·" in $g(s)$ do not need to be calculated since only the elements in the four corners of the matrix $g(s)$ will enter into $g_0(s+1)$ in the next step of the iteration. We obtain (see Appendix A)

$$
\begin{aligned}
g_S(s) &= \left(E - H_s - \left(\tilde{\Omega}_s T_s + T_s^\dagger \Omega_s' + H_{s-1,s}^\dagger g_S(s-1) H_{s-1,s}\right)\right)^{-1}, \\
g_T(s) &= \Omega_s g_S(s), \\
g_{\bar{T}}(s) &= g_S(s) \tilde{\Omega}_s, \\
g_{ic}(s) &= g_{ic}(s-1) + \Omega_s g_{\bar{T}}(s),
\end{aligned}
\tag{2.17}
$$

where we have defined

$$
\begin{aligned}
\Omega'_s &\equiv g_T(s-1)H_{s-1,s}, \\
\Omega_s &\equiv g_{ic}(s-1)T_s + \Omega'_s, \\
\tilde{\Omega}_s &\equiv T_s^\dagger g_{ic}(s-1) + H_{s-1,s}^\dagger g_{\bar{T}}(s-1).
\end{aligned}
$$

Usually, $N_S \gg 1$ in practice, so this iteration for $s = 2, \ldots, N_S$ is the most time-consuming part of the calculation and should therefore be optimized. An efficient algorithm—involving a minimum number of individual calculations and a minimum amount of computer memory—could have the following form:

- Setting $T_s = \mathbf{0}$, calculate Ω_s, $\tilde{\Omega}_s$, and $\omega_s \equiv E - H_s - H_{s-1,s}^\dagger g_S(s-1)H_{s-1,s}$.

- If $T_s \neq \mathbf{0}$, then update in this order:
  1. $\omega_s \leftarrow \omega_s - T_s^\dagger \Omega_s$ (note that still $\Omega_s = \Omega'_s$ at this point),
  2. $\Omega_s \leftarrow \Omega_s + g_{ic}(s-1)T_s$,
  3. $\tilde{\Omega}_s \leftarrow \tilde{\Omega}_s + T_s^\dagger g_{ic}(s-1)$,
  4. $\omega_s \leftarrow \omega_s - \tilde{\Omega}_s T_s$.

- Invert ω_s to obtain $g_S(s)$ and calculate—in this order—$g_T(s)$, $g_{\bar{T}}(s)$, and $g_{ic}(s)$ according to Eqs. (2.17).

Updating the lead components

According to this scheme, the final values of the lead components are calculated:
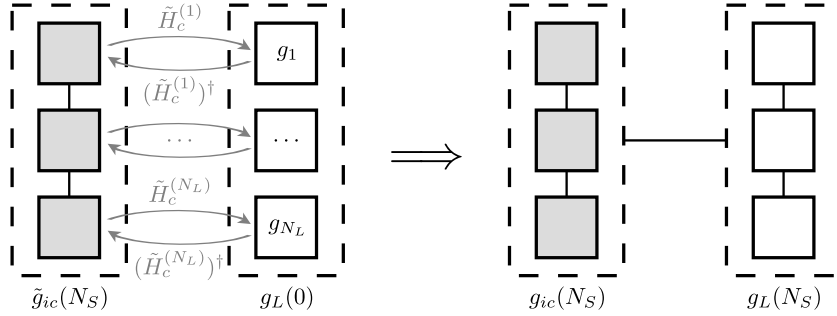
The Dyson equation for this step reads $g_L^{ic}(N_S) = \left(\mathbf{1} - g_L^{ic}(0)V_L^{ic}\right)^{-1} g_L^{ic}(0)$, where

$$
g_L^{ic}(0) \equiv \begin{pmatrix} \tilde{g}_{ic}(N_S) & \mathbf{0} \\ \mathbf{0} & g_L(0) \end{pmatrix}, \qquad V_L^{ic} \equiv \begin{pmatrix} \mathbf{0} & \tilde{H}_c^L \\ (\tilde{H}_c^L)^\dagger & \mathbf{0} \end{pmatrix},
$$

where we defined

$$
g_L(0) \equiv \begin{pmatrix} g_1 & & \\ & \ddots & \\ & & g_{N_L} \end{pmatrix}, \qquad \tilde{H}_c^L \equiv \begin{pmatrix} \tilde{H}_c^{(1)} & & \\ & \ddots & \\ & & \tilde{H}_c^{(N_L)} \end{pmatrix},
$$

and

$$g_L^{ic}(N_S) \equiv \begin{pmatrix} g_{ic}(N_S) & \cdot \\ \cdot & g_L(N_S) \end{pmatrix}.$$

Again, "·" indicates matrix elements that do not need to be calculated. The component $\tilde{g}_{ic}(N_S)$ describing the Green's function matrix elements on the interface cells in the presence of the scattering region but in the absence of the leads is not known and therefore has to be eliminated according to Eq. (A.1). Thus, we finally obtain the matrix Green's function components that enter the corresponding equation to Eq. (2.10) for the effective system shown in Fig. 2.4,

$$\begin{pmatrix} G_{\tilde{L}_1^0 \tilde{L}_1^0} & \dots & G_{\tilde{L}_1^0 \tilde{L}_{N_L}^0} \\ \dots & \dots & \dots \\ G_{\tilde{L}_{N_L}^0 \tilde{L}_1^0} & \dots & G_{\tilde{L}_{N_L}^0 \tilde{L}_{N_L}^0} \end{pmatrix} \equiv g_L(N_S)$$

$$= g_L(0) + g_L(0)(\tilde{H}_c^L)^\dagger g_{ic}(N_S)\tilde{H}_c^L g_L(0), \qquad (2.18)$$

where $\tilde{L}_l^0$ is the surface of the effective lead $\tilde{L}_l$ located at $\tilde{z}_l = 0$ in Fig. 2.4.

2.5 Outlook

In this section concluding the methodic part of this thesis, we take a look beyond the actual focus of this thesis to highlight the full potential of the RGF algorithm, discuss the effects of interactions beyond a mean-field approximation, and comment on alternative computational techniques.

Updating the scattering region ("backward sweep")

The backward sweep proceeds according to this scheme:
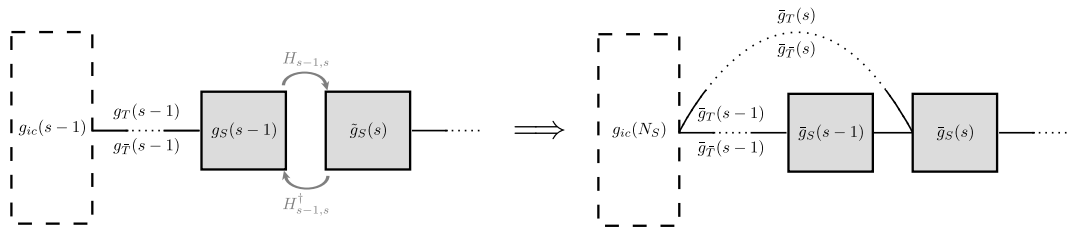
For the evaluation of the transmission function, it is sufficient to calculate the surface elements of the system Green's function matrix as outlined above. If local quantities as defined in Section 1.6 are of interest, it is necessary to calculate additional elements of the retarded system Green's function matrix. This is achieved by performing a "backward sweep" in analogy to the "forward sweep" discussed in Section 2.4. The complexity of this procedure depends on the number of non-zero couplings T_s. Since it is always possible (though not always optimal in terms of efficiency) to choose layers such that $T_s = \mathbf{0}$ for $s > 1$, we will outline this procedure for this simple case. Again, we have to solve the Dyson equation

$\bar{g}(s) = \left(\mathbf{1} - \bar{g}_0(s)\bar{V}(s)\right)^{-1}\bar{g}_0(s)$ iteratively for $s = N_S, \ldots, 2$, where

$$\bar{g}_0(s) \equiv \begin{pmatrix} g_{ic}(s-1) & g_T(s-1) & \mathbf{0} \\ g_{\bar{T}}(s-1) & g_S(s-1) & \mathbf{0} \\ \mathbf{0} & \mathbf{0} & \tilde{g}_S(s) \end{pmatrix}, \qquad \bar{V}(s) \equiv \begin{pmatrix} \mathbf{0} & \mathbf{0} & \mathbf{0} \\ \mathbf{0} & \mathbf{0} & H_{s-1,s} \\ \mathbf{0} & H_{s-1,s}^\dagger & \mathbf{0} \end{pmatrix},$$

and

$$\bar{g}(s) \equiv \begin{pmatrix} g_{ic}(N_S) & \cdot & \cdot \\ \bar{g}_{\bar{T}}(s-1) & \bar{g}_S(s-1) & \cdot \\ \bar{g}_{\bar{T}}(s) & \cdot & \bar{g}_S(s) \end{pmatrix},$$

where again "$\cdot$" indicates matrix elements that do not need to be computed, and $\tilde{g}_S(s)$, describing the Green's function matrix elements on layer s in the presence of layers $s' > s$ but in the absence of the leads and layers $s' < s$, is not known. The matrices $g_S(s)$, $s = 1, \ldots, N_S$, have to be stored during the forward sweep. From Appendix A, we obtain the relations

$$\bar{g}_S(s-1) = g_S(s-1) + g_S(s-1)H_{s-1,s}\bar{g}_S(s)H_{s-1,s}^\dagger g_S(s-1),$$

$$\bar{g}_{\bar{T}}(s-1) = \underbrace{g_{\bar{T}}(s-1)}_{\left(\bar{g}_S(s)H_{s-1,s}^\dagger\right)^{-1}\bar{g}_{\bar{T}}(s)} + g_S(s-1)H_{s-1,s}\bar{g}_{\bar{T}}(s),$$

where $g_{\bar{T}}(s-1)$ can be substituted as indicated if it is not stored during the forward sweep, e.g., due to limited computer memory. The initial conditions $\bar{g}_S(N_S) = g_S(N_S)$ and $\bar{g}_{\bar{T}}(N_S) = g_{\bar{T}}(N_S)$ are known from the last step in the forward sweep. From $\bar{g}_S(s) = G_{S_s}^r(E)$, the LDOS or rather the quantity $d^\nu(\mathbf{x}_i, E)$ defined in Section 1.6 can be obtained according to Eq. (1.35) and with $\bar{g}_{\bar{T}}(s) = G_{S_s S_{ic}}^r(E)$, where S_{ic} denotes the set of interface cells, the elements of the lesser Green's function that enter into the definition of the local charge or spin (current) density can be obtained from Eqs. (1.28) and (1.29).

In some cases, it can be preferable—in terms of computational efficiency—to choose layers, e.g., such that also $T_{N_S} \neq \mathbf{0}$; a commonly encountered situation where this is true is the case of having a scattering region that is connected to two leads only. Then, the Green's function matrix elements involving sites on the last layer would have to be maintained during the backward sweep. The necessary extensions to the algorithm presented in the previous paragraph are straightforward. For more details, we refer the reader to Ref. [Wim09a], where the author develops an optimization algorithm (based on graph theory) that automatically identifies and constructs the layers for an arbitrary multi-terminal system geometry with maximum performance.

Effect of interactions

Here, we summarize the changes to the formalism in the context of the computational technique developed in this chapter if interactions beyond a mean-field approximation are taken into account. We first note that the presence of such interactions at $t = t_0$ give rise to an appendix to the Keldysh contour along the negative imaginary time axis; however, in most cases of interest, it can be argued that this appendix is negligible [Ram07]. The fluctuation-dissipation theorem, Eq. (1.23), still holds in thermal equilibrium in the presence

of interactions [Wim09a, Kad62], and while Eq. (1.32) is not valid anymore in the interacting case, the current can still be obtained from Eq. (1.31) if interactions are present only in the scattering region [Wim09a, Mei92]. Eq. (1.10) is amended by a self-energy contribution $\Sigma_{\text{int}}(\tau_1, \tau_2)$ [Ram07, Wim09a],

$$G = G^{(0)} + G^{(0)}(V + \Sigma_{\text{int}})G$$

in compact notation. In an open quantum system in the steady state, in the energy domain we then have equations for the retarded Green's function of the form

$$G_S = G_S^{(0)} + G_S^{(0)}\Big(\boldsymbol{\Sigma}_S + \sum_{l,l'} \boldsymbol{\Sigma}_{SL_l}\tilde{G}_{ll'}\boldsymbol{\Sigma}_{L_{l'}S}\Big)G_S,$$

$$\tilde{G}_{ll'} \equiv \delta_{ll'}G_{L_l}^{(0)} + \sum_{l''} G_{L_l}^{(0)}\boldsymbol{\Sigma}_{L_lL_{l''}}\tilde{G}_{l''l'},$$

where we suppressed the upper index r and the energy variable E. For the case of non-interacting leads, $\boldsymbol{\Sigma}_{L_lL_{l'}} = \mathbf{0}$, a direct inversion (which is feasible for small systems only) is still possible if $\boldsymbol{\Sigma}_{SL_l}$ and $\boldsymbol{\Sigma}_{L_lS}$ only involve the (appropriately chosen) surface of the lead:

$$G_S = \Big(\mathbf{1} - G_S^{(0)}\Big(\boldsymbol{\Sigma}_S + \sum_l \boldsymbol{\Sigma}_{SL_l}G_{L_l}^{(0)}\boldsymbol{\Sigma}_{L_lS}\Big)\Big)^{-1} G_S^{(0)}.$$

Further, a recursive technique is applicable only if additionally $\boldsymbol{\Sigma}_{SL_l}$ and $\boldsymbol{\Sigma}_{L_lS}$ are local in the sense that they only involve lattice sites in the (appropriately chosen) interface cell, and if $\boldsymbol{\Sigma}_S$ is layer-local, i.e., only involves lattice sites within neighboring layers. In this case, $\boldsymbol{\Sigma}_{SL_l}$ and $\boldsymbol{\Sigma}_{L_lS}$ can simply be absorbed into the coupling matrices T_s, while $\boldsymbol{\Sigma}_S$ can be absorbed into the matrices H_s, $H_{s-1,s}$, and $H_{s,s-1}$.[15]

Alternative numerical techniques

The foundations of the algorithm presented in the previous section have already been established about 30 years ago by Thouless and Kirkpatrick [Tho81], Lee and Fisher [Lee81b], as well as MacKinnon [Mac85], who made this technique popular. Since then, a great number of variants and extensions as well as similar techniques have evolved, and we refer the reader to Ref. [Tod94] as well as Sections 4.1 and 4.4.2 of Ref. [Wim09a] for a number of relevant references (for references concerning the construction of the lead Green's function, see Sections 3.1 and D.1 therein).

In the original formulation, the algorithm is restricted to systems with only two collinear leads, giving rise to a natural ordering [Wim09a, Wim09b] of layers along the line connecting the two leads. However, this restriction is easily resolved and while in Refs. [Wim09a, Wim09b], the authors focus on the development of an elaborate generic transport algorithm based on a graph-theoretic approach, which is applicable to arbitrary multi-terminal setups and lattice structures and which provides optimal performance, in the previous section we presented a prescription how multiple terminals can be taken into account that shows how

---

[15] Note that the resulting effective Hamiltonian might not be hermitian anymore, so the concrete formulas in Section 2.4 would have to be modified accordingly, e.g., by replacing $H_{s-1,s}^\dagger \rightarrow H_{s,s-1}$.

easily such an extension to the original formulation can be obtained especially in the case where only the scattering matrix is of interest. The key feature lies in maintaining more components of the Green's function during the recursion, and while our algorithm is therefore not as efficient as the graph-theoretic approach, for most cases it is still comparable in performance in the sense that the system sizes that can be managed for a given geometry are similar for both algorithms.[16]

A key element of our implementation of the RGF technique is the effective treatment of leads with non-invertible inter-cell coupling matrices H_c in a way that allows for solving an ordinary linear eigenvalue problem, Eq. (2.4), instead of an equivalent generalized eigenvalue problem, which is used in Ref. [Wim09a], but was found to be unstable in certain cases by the authors of Ref. [Roc06]. While this effective description introduces a finite and usually very small number of isolated singularities for the possible values of the energy E into the problem, the matrix $\tilde{H}_{uc}$ describing the effective lead is generally smaller than H_{uc} and corresponding matrix multiplications are thus performed faster in the effective description—a feature from which also the technique developed in Ref. [Wim09a] may benefit; we also mention that the algorithm used there is not immune to such isolated singularities in general; if at a given energy there are propagating states with vanishing group velocity, they cannot be classified into in- or out-propagating states and consequently, eigendecomposition as well as Schur decomposition based methods fail.

In Ref. [Wim09a], the author identifies numerically unstable behavior of the commonly applied eigendecomposition based methods—as also used in the present thesis—to calculate the lead surface Green's function in the presence of strong magnetic fields in the leads,[17] in which case the matrix U may become ill-conditioned and its inversion in Eq. (2.8) is thus meaningless. Using the Schur decomposition, the author further develops an alternative construction routine for the lead Green's function based on the calculation of so-called invariant subspaces instead of individual eigenvectors, resolving this issue; however, although the author finds this technique to be numerically stable for the investigated systems, he does not rule out the possibility of this method becoming unstable in other contexts (see Section 3.3.3 in this reference). As another slight disadvantage, he finds that the developed technique is not able to cope with degenerate propagating states of different propagation direction without introducing an inconvenient infinitesimal imaginary (or real) shift of the energy into the numerics; in an eigendecomposition based method, Eq. (2.6) can always be invoked in this case.

---

[16] Due to the scaling properties of the various RGF algorithms, the theoretical increase in computing time is a factor of 16 if the system size is scaled by a factor of 2. The graph-theoretic approach is found to yield a performance gain up a factor of three only, for large systems and appropriate system geometries [Wim09a, Wim09b]. Therefore, the main advantage of this routine is seen in the automated construction of layers providing an effective two-terminal system, enabling the calculation of local properties in the first place.

[17] In our opinion, the relevance of such a situation for practical purposes is not immediately clear. Sure, confining the magnetic field such that it vanishes in the leads can be argued to be not quite realistic; however, if one instead implements the magnetic field in the leads, it would have to be homogeneous there over an infinite distance due to the enforced periodicity of the lead—a situation which can be argued to be equally unrealistic. However, avoiding the additional scattering at the boundaries of a region of confined magnetic field by extending the field into the leads may be of use in the interpretation of numerical results.

Part II

Electronic transport in graphene

Chapter 3

Basic properties of graphene

The formalism developed in the previous chapters allows for the numerical computation of observables in effectively non-interacting open quantum systems described within the tight binding approximation. The efficiency of the recursive scheme outlined in Section 2.4 facilitates the treatment of mesoscopic systems, i.e., systems composed of a large number of lattice sites or atoms, which are much more complex than a typical molecule while still being small enough to be subject to quantum effects. Mesoscopic systems thus constitute an intermediate regime between the microscopic and macroscopic worlds fully governed by quantum and classical physics, respectively.

In 2004, mesoscopic physics has been revolutionized by the first successful isolation of a strictly two-dimensional material composed of an one atom thick layer of carbon atoms arranged in a hexagonal lattice called "graphene" [Nov04]. Although alternative and improved methods for isolating graphene have been developed in recent years [Gei07, Gei09], the original technique, which is surprisingly simple and is often referred to as scotch-tape technique [Gei09], is still routinely used. With this technique, individual carbon multilayers are extracted from graphite by mechanical exfoliation and the number of layers of a particular sample is determined by optical microscopy and Raman spectroscopy [Fer06, Gup06, Gei07]. Nowadays, besides topological insulators, graphene is still the most-used material system in the field of mesoscopic physics and has already found its way into the commercial market [gra12].

With its discovery in 2004, this two-dimensional allotrope is the last element in the series of related carbon configurations of different dimensionality besides graphite, fullerenes (or buckyballs), and carbon nanotubes [Gei07]. However, graphene has been known theoretically since the fundamental work by Wallace in 1946 [Wal47]. In the remainder of this chapter, we summarize some fundamental properties of graphene that will form the basis of the effects investigated in the following chapters.

3.1 Tight binding and effective mass models of graphene

In Fig. 3.1(a), we show the hexagonal lattice structure of crystalline graphene, also known as the honeycomb lattice. Each carbon atom is connected to three nearest neighbors at a distance $a_0 \approx 0.142$ nm [CN09] via the vectors

$$\boldsymbol{\delta}_s = a_0 \begin{pmatrix} \cos(\alpha + 2\pi s/3) \\ \sin(\alpha + 2\pi s/3) \end{pmatrix}, \qquad s = 0, 1, 2.$$
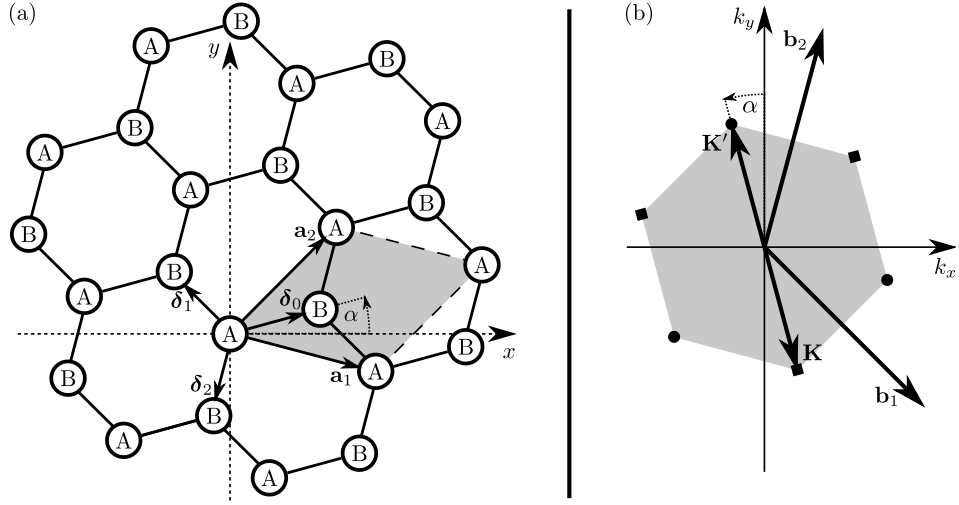
Figure 3.1: (a) The hexagonal lattice structure of crystalline graphene, also known as the honeycomb lattice. The primitive unit cell (shaded) spanned by the primitive lattice vectors $\mathbf{a}_1$ and $\mathbf{a}_2$ contains two inequivalent basis atoms forming two hexagonal sublattices labeled A and B. Each A atom has three nearest neighbors on the B sublattice to which it is connected via the vectors $\boldsymbol{\delta}_s$, $s = 0, 1, 2$ (Figure adapted from Ref. [Sch11]). (b) The reciprocal lattice in $\mathbf{k}$-space spanned by the primitive reciprocal lattice vectors $\mathbf{b}_1$ and $\mathbf{b}_2$. The $\mathbf{K}$- and $\mathbf{K}'$-points as defined in the text are also indicated; note that the remaining four corners of the Brillouin zone (shaded) are equivalent to either the $\mathbf{K}$-point (squares) or the $\mathbf{K}'$-point (circles) by means of a translation along a reciprocal lattice vector.

Note that although there is only one type of atoms present, the graphene lattice cannot be described as a Bravais lattice with a basis consisting of just one atom. Instead, the primitive unit cell consists of two inequivalent[1] basis atoms, encloses an area $A = 3a_0^2\sqrt{3}/2$, and can be chosen to be spanned by the primitive lattice vectors

$$\mathbf{a}_{1,2} = \boldsymbol{\delta}_0 - \boldsymbol{\delta}_{1,2}, \qquad |\mathbf{a}_{1,2}| = a_0\sqrt{3}.$$

The presence of two basis atoms within the primitive unit cell induces a sublattice structure: Atoms located at positions $\mathbf{r} = n\mathbf{a}_1 + m\mathbf{a}_2$, $n, m \in \mathbb{Z}$, are said to belong to the A sublattice, the remaining atoms are said to belong to the B sublattice.

With the usual definition $\mathbf{a}_i\mathbf{b}_j = 2\pi\delta_{ij}$, $i, j \in \{1, 2\}$ [Kit96], we obtain the primitive reciprocal lattice vectors

$$\mathbf{b}_{1,2} = \frac{2\pi}{3a_0} \begin{pmatrix} \cos\alpha \pm \sqrt{3}\sin\alpha \\ \sin\alpha \mp \sqrt{3}\cos\alpha \end{pmatrix}, \qquad |\mathbf{b}_{1,2}| = \frac{4\pi}{3a_0}.$$

The reciprocal space (or $\mathbf{k}$-space) defined by these vectors as well as the (first) Brillouin zone is shown in Fig. 3.1(b). The corners of the Brillouin zone are commonly called $\mathbf{K}$- or

---

[1] In a lattice (real or reciprocal space), we refer to two lattice sites as being equivalent if they are connected by a (reciprocal) lattice vector.

$\mathbf{K}'$-point; more specifically, we define

$$\mathbf{K} = \frac{4\pi}{3a_0\sqrt{3}} \begin{pmatrix} \sin\alpha \\ -\cos\alpha \end{pmatrix}, \qquad \mathbf{K}' = -\mathbf{K},$$

without loss of generality; the remaining corners of the Brillouin zone are equivalent to either $\mathbf{K}$ or $\mathbf{K}'$ by means of a translation along a reciprocal lattice vector and therefore do not constitute independent states in $\mathbf{k}$-space.

The regions around the $\mathbf{K}$- and $\mathbf{K}'$-points are particularly crucial as we will see in the following. To this end, we consider the electronic spectrum of graphene. Carbon atoms have four valence electrons in the outermost shell. In the planar configuration, carbon exhibits a sp^2-hybridization, where the $2s$-orbital is hybridized with the $2p_x$- and $2p_y$-orbitals (assuming an orientation within the xy-plane) to yield three energetically equivalent sp^2-orbitals. For each carbon atom, three of the four valence electrons are used to form σ-bonds within the sp^2-orbitals in the graphene plane while the fourth electron remains as conduction electron in the π-orbitals formed by the remaining $2p_z$-orbitals; usually, the calculation of the electronic spectrum (or bandstructure) is solely concerned with these delocalized π-electrons. To be more specific, there actually exist two bands of electronic states due to the fact that there are two carbon atoms per unit cell; however, since there is only one π-electron per carbon atom, only half of the states is actually occupied in undoped graphene.

The calculation of the tight binding bandstructure of graphene follows the standard textbook procedure [Ash76] and has been done a number of times in the literature; for details, we direct the reader to Refs. [Wal47, Wim09a, Ben09b, Sch12c, Sai00, Sai98]. In the simplest approximation, where only hopping between nearest neighbors is taken into account, the tight binding model of graphene can be formulated as

$$-t\sum_{s=0}^{2} \Psi(\mathbf{r} + \zeta_{\mathbf{r}}\boldsymbol{\delta}_s) = E\Psi(\mathbf{r}), \tag{3.1}$$

where the sign factor $\zeta_{\mathbf{r}} = \pm 1$ specifies the sublattice (A $\widehat{=}$ +1 and B $\widehat{=}$ −1) of the lattice site located at position $\mathbf{r}$ and $t \approx 2.7\,\mathrm{eV}$ is the nearest neighbor hopping integral [CN09]. Neglecting overlap integrals of neighboring orbital wavefunctions, which are small compared to the nearest neighbor hopping integral, the final expression for the energy dispersion relation reads

$$E(\mathbf{k}) = \pm t \left| 1 + \mathrm{e}^{\mathrm{i}\mathbf{k}\mathbf{a}_1} + \mathrm{e}^{\mathrm{i}\mathbf{k}\mathbf{a}_2} \right| \tag{3.2}$$

and is shown in Fig. 3.2(a). Since exactly half of the available states are filled in undoped (or intrinsic) graphene in the ground state, states with $E < 0$, which form the valence band (bonding π band), are occupied, whereas states with $E > 0$, which form the conduction band (antibonding π^* band), are empty, and the Fermi energy is $E_F = 0$; this zero of energy is therefore also referred to as the charge neutrality point. Intrinsic graphene is thus a zero-gap semiconductor or semimetal with a vanishing density of states[2] at the charge neutrality point as well as a van Hove singularity [Hov53] of divergent density of states at $|E| = t$ (see Fig. 3.2(b)). With respect to the ground state, the electronic excitations are referred

---

[2] An analytical expression for the density of states is given in Refs. [CN09, Hob53].

(a)

k_y $[\pi/a_0]$

E $[t]$

k_x $[\pi/a_0]$

K′

K

(b)

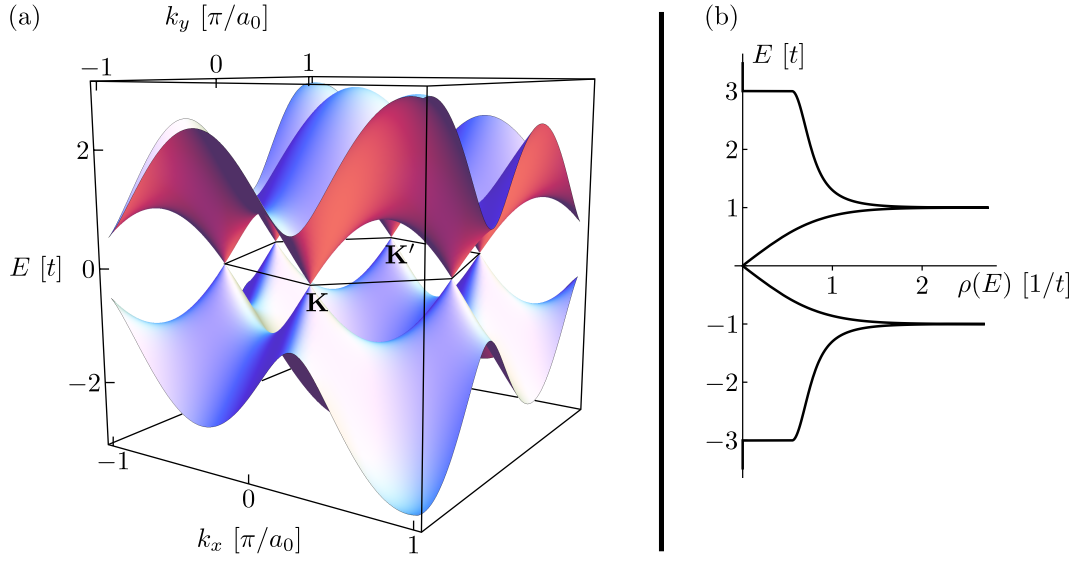E $[t]$

$\rho(E)$ $[1/t]$

Figure 3.2: (a) The tight binding energy dispersion relation of graphene, obtained from Eq. (3.2), shown for $\alpha = \pi/12$. The Brillouin zone and the Dirac points from Fig. 3.1(b) are also indicated. (b) The corresponding density of states $\rho(E)$ as given in Refs. [CN09, Hob53], which exhibits a divergent van Hove singularity [Hov53] at $|E| = t$ and a linear behavior around $E = 0$ with slope $2A/(\pi v_F^2)$.

to either as electron states (occupied states in the conduction band) or hole states (empty states, i.e., missing electrons, in the valence band). A change of the Fermi energy can be induced, e.g., by means of a electrostatic gate potential. Such extrinsic graphene may be either n-doped ($E_F > 0$) or p-doped ($E_F < 0$), and junctions between regions of different doping levels are correspondingly referred to as np-junctions, nn'-junctions, and so forth.

The regions around **K**, **K′**, and equivalent points are commonly called "valleys". Two neighboring valleys are separated by a distance $\Delta K \equiv 4\pi/(3a_0\sqrt{3})$ in reciprocal space, which provides the amount of momentum transfer necessary to scatter between the valleys ("intervalley scattering") by means of a scattering potential $V(\mathbf{r}) = (2\pi)^{-2} \int \tilde{V}(\mathbf{q}) e^{-i\mathbf{q}\mathbf{r}} d\mathbf{q}$. This potential thus has to contain dominant high-frequency Fourier components $\tilde{V}(\mathbf{q})$ with $|\mathbf{q}| \sim \Delta K$ and in turn fluctuates on the lattice scale, $\lambda \sim 2\pi/\Delta K = 3a_0\sqrt{3}/2 \sim a_0$. Such a potential is commonly called "short-ranged", in contrast to long-range potentials, which vary over distances that are large compared to the lattice scale; such smooth potentials only contain dominant low-frequency Fourier components $\tilde{V}(\mathbf{q})$ where $|\mathbf{q}| \ll \Delta K$ and thus only support scattering within a single valley ("intravalley scattering").

Since electronic transport takes place in a narrow energy range $\sim k_B T$ around the Fermi energy, only states in the vicinity of the valleys at the **K**- and **K′**-points contribute to the electronic transport, which is thus well-described by a low-energy expansion around these points. This low-energy approximation, also called effective mass or continuum model, can be introduced by the ansatz

$$\Psi(\mathbf{r}) = \sqrt{A}\left(e^{i\mathbf{K}\mathbf{r}}\phi_{\zeta_\mathbf{r}} + e^{-i\mathbf{K}\mathbf{r}}\phi'_{\zeta_\mathbf{r}}\right) \tag{3.3}$$

for the tight binding wavefunction $\Psi(\mathbf{r})$, where the two pairs of envelope functions $\phi_\pm$ and $\phi'_\pm$ that correspond to the valleys at $\mathbf{K}$ and $\mathbf{K}'$, respectively, are smooth on the scale a_0, i.e., composed of Fourier components with wavevectors $\boldsymbol{\kappa}$ where $|\boldsymbol{\kappa}| \ll |\mathbf{K}|$ such that we may use the Taylor series approximation up to first order,

$$\phi(\mathbf{r} \pm \boldsymbol{\delta}_s) \approx \phi(\mathbf{r}) \pm \boldsymbol{\delta}_s \cdot (\boldsymbol{\nabla}\phi)(\mathbf{r}), \qquad s = 0, 1, 2, \tag{3.4}$$

for any of the four envelope functions. Arranging these four slowly varying amplitudes in the vector

$$|\Phi\rangle \equiv \left(\mathrm{e}^{-\mathrm{i}\alpha/2}\phi_+, \ -\mathrm{i}\mathrm{e}^{\mathrm{i}\alpha/2}\phi_-, \ -\mathrm{i}\mathrm{e}^{-\mathrm{i}\alpha/2}\phi'_-, \ \mathrm{e}^{\mathrm{i}\alpha/2}\phi'_+\right)^{\mathsf{T}} \tag{3.5}$$

and substituting the ansatz (3.3) into the tight binding model (3.1) taking into account Eq. (3.4), one arrives at the valley-isotropic Dirac or Dirac–Weyl Hamiltonian [Bee08a],[3]

$$H_0 = v_F \begin{pmatrix} \boldsymbol{\sigma} \cdot \mathbf{p} & 0 \\ 0 & \boldsymbol{\sigma} \cdot \mathbf{p} \end{pmatrix}, \qquad \mathbf{p} = -\mathrm{i}\hbar\boldsymbol{\nabla}, \tag{3.6}$$

to which $|\Phi\rangle$ is an eigenstate,

$$H_0|\Phi\rangle = \pm\hbar v_F \kappa |\Phi\rangle,$$

if the envelope functions $\phi_\pm$ and $\phi'_\pm$ therein are composed of Fourier components with wave vectors of modulus $|\boldsymbol{\kappa}| = \kappa$; here $\hbar v_F \equiv 3ta_0/2$ and $\boldsymbol{\sigma} \equiv (\sigma_x, \sigma_y)^{\mathsf{T}}$ is the vector of Pauli matrices in the sublattice space.

At this point, we like to add the following remark: Note that the presence of the two (identical) carbon atoms per unit cell and the corresponding sublattice degree of freedom are directly connected to the presence of the two bands π and π^* and the electron–hole symmetry of the spectrum; however, it is not connected to the presence of the two inequivalent Dirac points $\mathbf{K}$ and $\mathbf{K}'$ in the reciprocal space and the corresponding valley degree of freedom. The sublattice and valley structures constitute two independent degrees of freedom, commonly— but inconsistently[4]—called pseudo- and isospin, respectively, due to the resemblance to the real electron spin. Also note that due to the presence of the two Dirac points, clean graphene exhibits a two-fold valley (or orbital) degeneracy, in addition to the usual two-fold real spin degeneracy. We also note that there is an additional degeneracy directly at the charge neutrality point due to the touching of valence and conduction band.[5]

Using the usual replacement $\mathbf{p} \to \hbar\boldsymbol{\kappa}$, we see that momentum eigenstates also fulfill the eigenvalue equation

$$\frac{\boldsymbol{\sigma} \cdot \boldsymbol{\kappa}}{\kappa} \begin{pmatrix} \mathrm{e}^{-\mathrm{i}\phi/2} \\ \pm\mathrm{e}^{\mathrm{i}\phi/2} \end{pmatrix} = \pm \begin{pmatrix} \mathrm{e}^{-\mathrm{i}\phi/2} \\ \pm\mathrm{e}^{\mathrm{i}\phi/2} \end{pmatrix}, \qquad \kappa \equiv |\boldsymbol{\kappa}|, \qquad \mathrm{e}^{\mathrm{i}\phi} \equiv \frac{\kappa_x + \mathrm{i}\kappa_y}{\kappa}, \tag{3.7}$$

which is valid for each of the two valleys. The direction of the pseudospin is thus tied to the momentum (measured with respect to the charge neutrality point): it is parallel for

---

[3] The valley-isotropic representation (3.6) is only one out of a number of different and commonly used representations that are connected to each other by unitary transformations (see, e.g., Ref. [Akh08b]).

[4] Compare, e.g., Refs. [McC06] and [Bee08a].

[5] In more detail: At the Dirac points, the Hamiltonian density [Ben09b] vanishes, so that all possible linear combinations of the two orbital wavefunctions per unit cell provide a zero-energy eigenstate.

conduction band states while it is antiparallel for valence band states. Conduction band states are said to exhibit a positive chirality[6] (upper sign), while valence band states have a negative chirality (lower sign). This property becomes even more obvious if one notes that due to the conic structure of the low-energy dispersion, the direction of propagation, which is given by the group velocity, i.e., the gradient of the energy dispersion, is tied to the momentum $\boldsymbol{\kappa}$ and $\boldsymbol{\sigma}$ essentially represents the velocity operator in a single valley up to some prefactor:

$$\mathbf{v} \equiv \frac{\mathrm{d}}{\mathrm{d}t}\mathbf{r} \equiv \frac{\mathrm{i}}{\hbar}[H_0, \mathbf{r}] = v_F \begin{pmatrix} \boldsymbol{\sigma} & 0 \\ 0 & \boldsymbol{\sigma} \end{pmatrix},$$

where we used the Heisenberg equation of motion. Also note the spinor property of the two-component wavefunction in Eq. (3.7); it acquires an overall sign, a so-called Berry's phase π, by a rotation of the angle ϕ by 2π [Zha05, Nov05, CN09].

In summary, we can assess that the low-energy excitations of graphene behave similar to massless, relativistic Dirac fermions with a linear[7] dispersion forming one so-called Dirac cone per valley, however with a renormalized (Fermi) velocity $v_F \approx 10^6$ m/s, which is roughly 0.3% of the speed of light.

3.2 Some phenomenological aspects of graphene

The unusual electronic structure of graphene discussed in the previous section, namely the behavior of the low-energy excitations as massless Dirac fermions, gives rise to a number of peculiar electronic and transport phenomena of (pseudo)relativistic character. In this section, we shortly summarize some of these as far as they are relevant for the topics addressed in the following chapters. For more details and the discussion of additional phenomena, we refer to one of the reviews on graphene, see Refs. [Gei07, Bee08a, CN09, Gei09, DS11, Nov11, And09].

Boundary conditions and edge states. Graphene physics strongly depend on the boundary conditions at lattice terminations. In Fig. 3.3, we show the lattice structure and the electronic spectrum of so-called zigzag and armchair graphene nanoribbons, which are quasi-one-dimensional systems and are named according to the microscopic shape of their respective edges. The spectrum of an armchair graphene nanoribbon is obtained by quantizing the transverse wavevector—k_y at $\alpha = 0$—of two-dimensional graphene (see Figs. 3.1 and 3.2) according to the ribbon width. Note that in this case states from both valleys are located around $k_x = 0$ and the two valleys are therefore coupled. Further, the lowest modes which cross the zero of energy are only present in *metallic* armchair graphene nanoribbons that contain $(3n + 1) \times 4$, $n \in \mathbb{N}$, atoms in their primitive unit cell and not in the remaining *semiconducting* armchair graphene nanoribbons. In contrast, the spectrum of zigzag graphene nanoribbons cannot be obtained by simply quantizing the transverse wavevector—k_y at $\alpha = \pi/6$—of two-dimensional graphene, since the zigzag edge supports additional states that

---

[6] In the context of graphene, the terms helicity and chirality are often used interchangeably [CN09].

[7] The tight binding dispersion relation exhibits a three-fold rotational symmetry around the Dirac points. In the second order in momentum in the low-energy expansion, this gives rise to a corresponding deviation of the linear spectrum from the strictly conical form, which is known as trigonal warping [CN09, Dre02, And98].
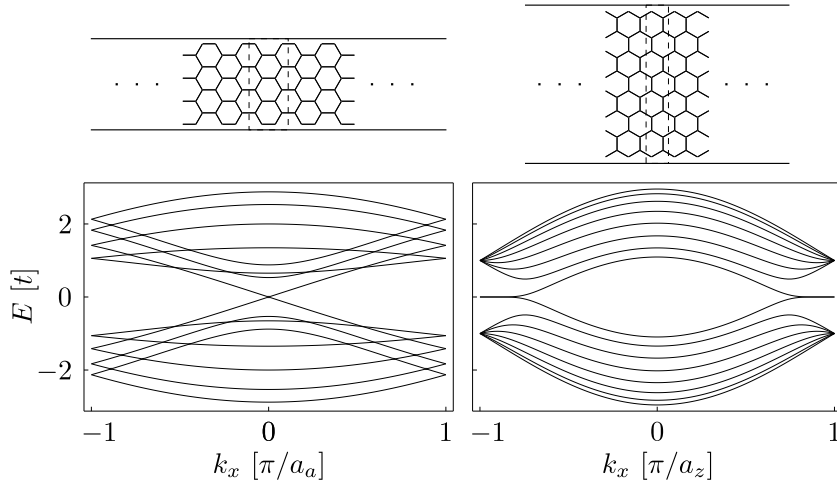
Figure 3.3: Lattice structures and electronic spectra of a metallic armchair graphene nanoribbon (left, lattice constant $a_a = 3a_0$) and a zigzag graphene nanoribbon (right, lattice constant $a_z = a_0\sqrt{3}$) with 16 atoms in the unit cell (dashed) each.

are localized at the edges, which are not captured in the models given in the previous section and shift the energies of the bulk states obtained by quantizing the transverse wavevector in energy by an amount depending on k_x. The edge states exhibit flat regions in the bandstructure at $|k_x| \gtrsim 2\pi/(3a_0\sqrt{3})$ leading to a divergence in the density of states at $E = 0$ in sharp contrast to the density of states of two-dimensional graphene (see Fig. 3.2(b)). Note further that states originating from the two valleys are well-separated and located around $k_x = \pm 2\pi/(3a_0\sqrt{3})$, respectively, in contrast to armchair graphene nanoribbons. Edges that do not exhibit pure zigzag or armchair terminations have been found to behave generically as zigzag edges [Akh08b]. For more details, we refer to Refs. [Bre06b, Bre07, Bre06a, Ryc07, Akh08a, Nak96, Fuj96] and in particular to Ref. [Wim09a].

Next-nearest neighbor hopping. The effects of hopping between next-nearest neighbors connected by the lattice vectors $\pm\mathbf{a}_1$, $\pm\mathbf{a}_2$, and $\pm(\mathbf{a}_1-\mathbf{a}_2)$, whose energy scale is $\sim 0.1t$ [CN09, Wim09a, Por95, Sas06], was neglected in the previous section. Inclusion of this hopping shifts the zero of energy and also breaks the electron–hole symmetry of the tight binding dispersion relation [Wal47, CN09],[8] which in turn leads to an asymmetric profile of the density of states [CN09, Wal47]. Next-nearest neighbor hopping also has a large impact on the edge state that is localized at a zigzag edge of graphene. It effectively acts on the edge state as if an on-site potential was applied to the zigzag edge atoms, introducing a dispersion into the previously flat band of the edge state [Wim09a]. Moreover, while electronic transport through the edge state in nearest neighbor approximation is found to be surprisingly robust to edge disorder, it suffers strong backscattering at such defects if next-nearest neighbor hopping is accounted for [Wim09a].

---

[8] Still, the linear spectrum of the effective mass model is electron–hole symmetric to a good approximation since next-nearest neighbor hopping only introduces corrections of second order in momentum [Wim09a].

Klein tunneling. An intriguing and extensively studied phenomenon that is encountered in graphene is chiral tunneling or Klein tunneling [Che06, Bee08a]. It is found that the transmission probability of Dirac quasiparticles through a potential barrier is one at normal incidence independent of the barrier height.[9] As the name suggests, this absence of backscattering is directly related to the chiral property of the low-energy excitations within one valley. At angles away from normal incidence, the transmission probability is in general less than one (except for transmission resonances that occur at specific values for the incident angle or the longitudinal momentum within the barrier) and is reduced with increasing smoothness of the potential barrier profile. Signatures of this behavior will be further discussed in Section 4.2.

Specular Andreev reflection. A related [Bee08b] phenomenon is the occurrence of specular Andreev reflection, i.e., the conversion of an electron to a hole at a graphene–superconductor junction, where the hole does not retrace the path of the incident electron as is the case in usual metals, but is instead reflected specularly from the interface [Bee06]. If the hole suffers specular reflection or instead retroreflection is determined by the Fermi energy and the energy of the electron–hole excitation. More specifically, reflection is specular if electron and hole originate from different bands, while retroreflection involves electrons and holes originating from the same band. This will be outlined further in Section 4.3. For details on the mean-field description of superconductivity in terms of the Bogoliubov–de Gennes Hamiltonian that couples electron and hole excitations via a superconducting order parameter, we refer the reader to Ref. [Gen99].

Pseudodiffusive transport and minimal conductivity. Due to the vanishing density of (propagating) states at $E = 0$, electronic transport at the Dirac point is dominated by evanescent modes and therefore exhibits pseudodiffusive behavior even in a disorder-free system [Pra07]. In contrast to ballistic transport, (pseudo)diffusive transport can be characterized in terms of a conductivity $\sigma = G \times L/W$ for a rectangular sample of length L along the transport direction, width W perpendicular to the transport direction, and conductance G. In clean graphene, the conductivity exhibits a minimum value $\sigma_{\min} = 4e^2/(\pi h)$ at the charge neutrality point in the universal limit $W \gg L$ where the microscopic details of the edges become insignificant while the Fano factor, which is a measure for the shot noise, exhibits the value $1/3$ typical for disordered metals [Two06, Kat06a, Dan08, Mia07, DiC08, Bee08a, Hee07, Bol08, Du08].

Disorder. Apart from the high mobilities—ranging from typical values of a few $10^4\,\mathrm{cm}^2/(\mathrm{Vs})$ up to values larger than $10^6\,\mathrm{cm}^2/(\mathrm{Vs})$ especially in suspended samples—and mean-free paths in the micron range at charge carrier densities up to $10^{13}\,\mathrm{cm}^{-2}$ [Nov04, Nov05, Zha05, Gei07, CN09, DS11, Nov11], graphene and in particular its electronic properties are quite susceptible to the effects of disorder due to the two-dimensional character of the material. For instance, the value $4e^2/h$ for the minimal conductivity—in contrast to the theoretical value of $4e^2/(\pi h)$—which is often observed especially in larger samples [Nov05, Zha05, Tan07, Gei07] may be attributed to the presence of impurities [Tit07a, Ost10, Sch09, Ost10]. Disorder can be introduced into the system in many different ways (for a detailed overview, see

---

[9] . . . , at least as long as contributions from evanescent modes within the barrier can be neglected [CN09].

Section IV in Ref. [CN09]), some of which are collected in the following. First, a long-ranged curvature of the graphene plane known as frozen flexural vibrational modes or ripples as well as structural or topological defects in the graphene lattice structure present main sources of intrinsic disorder. Curvatures and also strains within the graphene plane can locally change the hopping integrals, eventually leading to pseudomagnetic fields which break the effective time reversal symmetry within one valley (but not the real time reversal symmetry, which is conserved in the absence of a real magnetic field). Extrinsic sources of disorder are mainly classified according to their range; charged impurities that may be present either on top of the graphene plane or within the substrate induce smooth, long-ranged Coulomb potentials into the system, eventually leading to so-called electron–hole puddles, i.e., regions of different doping character (n or p). Further, intervalley scattering is induced in the presence of point-like defects, i.e., short-range potentials, which may originating from adatoms or molecules, such as hydrogen or CH_3, on the graphene surface. Adatoms, if strongly bound to graphene, effectively act as vacancies in the honeycomb lattice, which support electronic states at the charge neutrality point and thus act as resonant scatterers for the Dirac quasiparticles [Per06]. The effects of such impurities on the electronic transport properties of graphene are further investigated in Section 5.2.

Chapter 4

The Aharonov–Bohm effect in graphene

In this chapter, we consider electronic quantum interference in mesoscopic ring structures based on graphene with a focus on the interplay between the Aharonov–Bohm effect and the peculiar electronic and transport properties of this material. We first present an overview on recent developments of this topic both from the experimental as well as the theoretical side. We then present our work on two prominent graphene-specific features in the Aharonov–Bohm conductance oscillations, namely Klein tunneling and specular Andreev reflection. We close with an assessment of experimental and theoretical developments in the field and highlight open questions as well as potential directions of the developments in future work.[1]

4.1 Overview

The Aharonov–Bohm effect [Ehr49, Aha59, Aha61] is a fundamental phenomenon of quantum interference related to the transmission of particles through a closed loop pierced by a magnetic flux. Besides its fundamental significance for quantum theory, its importance for applications in mesoscopic interferometric devices such as the electron Sagnac gyroscope [Tol10] is omnipresent. The effect was originally observed in metal rings in 1985 [Web85] and later also in carbon nanotubes [Bac99]. In graphene, the Aharonov–Bohm effect is expected to exhibit unusual behavior due to the peculiar electronic properties of this material, in which charge carriers at low energy effectively behave as massless Dirac fermions, giving rise to a number of (pseudo)relativistic effects such as a Berry's phase π [Nov05, Zha05]. In the following, we review recent developments on the Aharonov–Bohm effect in graphene nanostructures, first from the experimental side, and later on, we elaborate more on theoretical aspects.

Experimental progress. The first experimental realization of a graphene ring structure was reported in 2008 [Rus08]. In this work, the authors investigate the Aharonov–Bohm oscillations in diffusive single-layer graphene as a function of the magnetic field which is applied perpendicular to the graphene plane in a two-terminal setup. They find clear magnetoconductance oscillations with the expected period corresponding to one magnetic flux quantum $\Phi_0 = h/e$ on top of a low-frequency background signal that is due to universal conductance fluctuations, which are present in any disordered, phase-coherent mesoscopic device [Dat05]. Increasing the temperature T gives rise to thermal averaging of the Aharonov–Bohm oscillations and the authors find that the oscillation amplitudes decay as $T^{-1/2}$ as is commonly observed in metal rings [Was86].

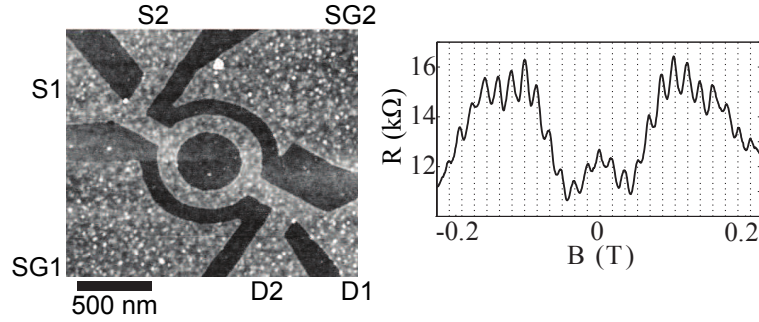[1] The work presented in this chapter has also been published in Refs. [Sch10a, Sch12b, Sch12a].

Figure 4.1: Scanning force micrograph and magnetoresistance of the four-terminal (S1/2, D1/2) graphene ring structure with two side gates (SG1/2) investigated in Ref. [Hue10] (Figure adapted from Ref. [Hue10]).

The authors further observe two unusual features in the recorded data. First, they find indications of a linear relationship between the oscillation amplitude and the overall ring conductance. Such a behavior has neither been observed in metal rings, nor in semiconductor heterostructures, with the exception of Ref. [Ang07], where a similar effect is seen. The authors speculate that tunnel barriers that may be present in their device could be responsible for the observed behavior; however, a detailed theoretical analysis has yet to be done.

A second peculiar feature is the significant increase of the oscillation amplitude at strong magnetic fields close to the onset of the quantum Hall regime. This increase is strong enough to make the second harmonic—i.e., oscillations of period $\Phi_0/2 = h/(2e)$—visible in the frequency spectrum. Such a behavior was also observed by another group in subsequent experiments with smaller rings and higher visibility in a two-terminal as well as a four-terminal geometry and was attributed there to scattering on magnetic impurities [Hue09]—an explanation derived from corresponding observations in metallic rings that is not compatible with the observations made in Ref. [Rus08], where the authors instead speculate that the increase of the oscillation amplitude may be due to orbital effects originating from a potential asymmetry in the arms of the ring; however, this assumption could not be confirmed in subsequent numerical calculations [Wur10].

In Ref. [Hue09], the authors also introduce additional tunability into the graphene ring device by applying a side gate potential to one of the ring arms. In subsequent experiments [Hue10], the same group systematically investigates the influence of such side gates in a four-terminal geometry (see Fig. 4.1) in the diffusive regime and find phase shifts of the Aharonov–Bohm oscillations as a function of the gate voltage as well as phase jumps of π at zero magnetic field—direct consequences of the electrostatic Aharonov–Bohm effect[2] (which is more feasible in graphene than in metal rings due to the low screening of this material) as well as the generalized Onsager relations. The authors of Ref. [Hue09] further speculate on the presence of edge disorder indicated by the fact that the various charge carrier trajectories around the ring, which can be derived from the frequency distribution of the magnetooscillations, do not cover the full area of the ring arms.

Further experiments on graphene ring structures include the local oxidation nanolithog-

---

[2] For details on the electrostatic Aharonov–Bohm, we refer the reader to Refs. [Boy73, Was87].

raphy using atomic force microscopy [Wen08] and antidot arrays on epitaxial graphene films [She08]; in the latter setup, universal conductance fluctuations are suppressed since the sample size exceeds the phase coherence length while Aharonov–Bohm oscillations are still visible due to the small size of the antidots. As a graphene-specific feature, the authors also observe increased visibility of weak localization due to intervalley scattering on antidot edges. Shubnikov–de Haas and Aharonov–Bohm effects on thin graphite single crystals with columnar defects were investigated in Refs. [Lat09, Lat10] in a four-probe measurement and a significant contribution of surface Dirac fermions ("graphene on graphite") as well as evidence supporting the theoretical prediction of edge states was found. Another multi-terminal measurement of Shubnikov–de Haas oscillations in monolayer graphene relating the Landau level separation between electrons and holes with the transport gap in the density of states is given in Ref. [Yoo10]; the poor visibility of the Aharonov–Bohm oscillations therein is attributed to a low phase coherence length.

Just recently, another experiment on the Aharonov–Bohm effect in graphene has been conducted. In Ref. [Smi12], the authors investigate the period and the amplitude of the observed Aharonov–Bohm oscillations in a graphene ring where one of the ring arms is subject to a top gate electrode allowing for the creation of a $pp'p$- or pnp-junction along this arm—a setup we initially proposed in Ref. [Sch10a] and which will be discussed in detail in Section 4.2.

Theoretical progress. On the theoretical side, there is a great variety of topics which have been addressed including the valley degree of freedom characteristic for graphene, particular device geometries and edge symmetries, resonant behavior and transistor applications, as well as the role of interactions. Common quantities expressing the influence of these aspects include electronic properties such as electronic spectrum and persistent current, as well as transport properties such as conductance and noise.

In the pioneering work on the topic of Aharonov–Bohm rings made of graphene [Rec07], it was shown—both analytically using a circular ring in the weak intervalley scattering limit in the continuum model as well as numerically using a hexagonal ring structure with zigzag terminated edges and strong intervalley scattering—that in the confined geometry of a graphene ring structure, an applied magnetic flux gives rise to a lifting of the orbital degeneracy in a controllable fashion, which is manifest in conductance and persistent current even in the absence of intervalley scattering. The magnitude of the lifting of the valley degeneracy and its dependence on details of the geometry of the ring have subsequently also been discussed in Ref. [Yan10]. The effect was further observed in numerical magnetotransport simulations in the closed (or weakly coupled) circular ring geometry described by the tight binding model [Wur10] for the case of smooth mass confinement, where intervalley scattering is suppressed. In this work, simulations have been done both for ballistic and diffusive regimes and up to the quantum Hall regime where Aharonov–Bohm oscillations are found to be suppressed.

Perfectly shaped ring devices with clean, well defined edges, such as the hexagonal ring structure mentioned before [Rec07], have been addressed in various studies exploiting graphene-specific features of such ideal nanostructures. A detailed numerical study of the influence of shape, geometry, edge symmetries, and corner structures on the electronic

structure in the presence of a magnetic field reveals, for example, the edge state anticrossing and therefore a gap opening due to the coupling of states localized at the inner and outer edges of the ring as well as the crucial role of corners in zigzag or armchair edge terminated rings [Bah09]. For instance, the corners in an ideal hexagonal ring with zigzag edge termination in a magnetic field introduce intervalley scattering as was considered in a supercell approach within the tight binding model [Ma09]; in this work, also a peculiar dependence of the spectrum as well as the persistent current on the even (resulting in semiconducting behavior) or odd (resulting in metallic behavior) character of the number of atoms across the ring arm was found. The spectrum of such hexagonal as well as trigonal rings of monolayer or bilayer graphene with zigzag boundaries as a function of the applied magnetic flux has further been discussed in Ref. [Rom12] in the nearest neighbor tight binding model, where, under inclusion of spin, the magnetization (or the persistent current) shows an even–odd behavior in connection with period doubling as is known from metallic rings in contrast to the observations made in Refs. [Yan10, Rec07]; while the authors argue that this discrepancy might originate from the infinite-mass boundary condition employed there, which is not able to capture effects of edge terminations and corner geometries, we believe that the extremely small width ($\approx 1\,\mathrm{nm}$) of the considered rings hardly allows for the observation of effects specific to (bulk) graphene, and indeed, the authors find that the observed behavior is substantially modified for wider rings. Similar hexagonal rings with metallic armchair termination have been considered in Refs. [Luo09, Fer10]; in such systems, appropriately chosen corner junctions exhibit signatures of broken effective time reversal symmetry—caused by pseudomagnetic fields—at low energies, such as broken electron–hole symmetry or a gap in the spectrum that may be closed by the application of a real magnetic flux.[3] In Ref. [Ma10], the authors calculate the spectrum and the persistent current in ideal diamond shaped graphene ring structures either with zigzag or armchair edge termination within the tight binding model; they also encounter the even–odd behavior mentioned before and compare their results with previous work on hexagonal rings [Ma09].

Such ideal structures have also been found to be dominated by resonant behavior in the magnetotransport, for instance in Ref. [Wu10], where for small rectangular graphene nanorings with perfect edges resonant tunneling through quasibound states was observed rather than Aharonov–Bohm oscillations, which may be tuned by varying geometry, Fermi energy, or magnetic field. Resonant behavior was also observed in Ref. [Wur10] as well as in in Ref. [Mun11], where it was proposed to utilize the electrostatic Aharonov–Bohm effect via side gates—such as already realized experimentally in Ref. [Hue10]—for application in a quantum interference transistor with high on/off ratio made of a hexagonal graphene ring structure with perfect edges, where armchair edges were found to be preferable. In contrast, zigzag edges in the leads acting as valley filters and a circular graphene ring structure exhibiting an irregular boundary have been considered in Ref. [Ryc09], where resonant behavior was encountered as well; however, the main finding of this work was that for opposite valley polarization in the leads and appropriately sized rings exhibiting higher harmonics in the Fourier spectrum due to multiple turns around the ring region, the lowest harmonic is suppressed while higher harmonics are unaffected. A similar geometry, namely

---

[3] The generation of pseudomagnetic fields in graphene rings under strain (or shear stress) has further been discussed in Ref. [Abe11].

a graphene Aharonov–Bohm ring connected to valley filters which encircles a dislocation, was considered in the continuum model in Ref. [Mes09] and decoherence properties were discussed. Possible applications as quantum interference transistors have also recently been discussed in Ref. [Xu12] for disordered graphene rings, where ballistic rectification and negative differential resistance are observed in the *I–V* characteristic; further, while for temperatures as large as 150 mK, phonon scattering is negligible, future work on the effect of electron–phonon interaction might be interesting.

Other aspects of interactions in graphene quantum rings have also been addressed in Ref. [Abe08] in the continuum model with a focus on the interplay between valley polarization and Coulomb interaction affecting the valley degeneracy. This influence was found to be accessible through the fractional nature of the periodicity of the Aharonov–Bohm oscillations in the persistent current as well as changes in the absorption spectrum. An analysis in the tight binding model including electron–electron interactions further revealed the connection between electronic correlations and the spin polarization of the interacting ground state as a function of ring size and number of electrons [Pot09, Pot10]. The interaction with the electromagnetic field has been discussed in Ref. [Mos09], where it was found that in a graphene ring threaded by a magnetic flux, excitations generated by electromagnetic pulses give rise to "valley currents"—in analogy to spin currents.

The peculiar properties of graphene systems suggest to consider the Aharonov–Bohm effect also in more graphene-specific ring geometries and transport regimes. The electronic properties of monolayer as well as bilayer graphene rings in a magnetic field have been addressed in Refs. [Zar09, Zar10b, Zar10a], either defining the ring geometry by tuning the band gap of bilayer graphene or employing a simplified zero-width ring geometry within the framework of the Dirac equation. In the magnetotransport within the (Andreev–)Corbino disk geometry in graphene, Landau level resonances, the suppression of conductance oscillations away from the charge neutrality point, and the crossover to the normal ballistic transport regime at large doping and weak fields have been encountered [Ryc10]. Analytical expressions for conductance and Fano factor in the magnetotransport of pseudodiffusive graphene rings, where transport at the Dirac point is dominated by evanescent modes, have been derived in Ref. [Kat10b].

In the next sections, we will discuss two graphene-specific effects in more detail. In Section 4.2, Klein tunneling of Dirac fermions through a potential barrier in a graphene ring system similar to the experimental setup of Refs. [Hue09, Hue10, Smi12] is considered. A related effect—Andreev reflection at a graphene–superconductor interface in a mesoscopic ring device—is subsequently discussed in Section 4.3. In Section 4.4 we will conclude and provide an outlook on potential future developments on the topic of the Aharonov–Bohm effect in graphene.

4.2 Interplay of the Aharonov–Bohm effect and Klein tunneling in graphene

In this section, we numerically investigate the effect of Klein tunneling [Kat06b, Che06] on the Aharonov–Bohm oscillations in a graphene ring on the basis of a tight binding model with nearest neighbor couplings. In order to introduce Klein tunneling into the system,
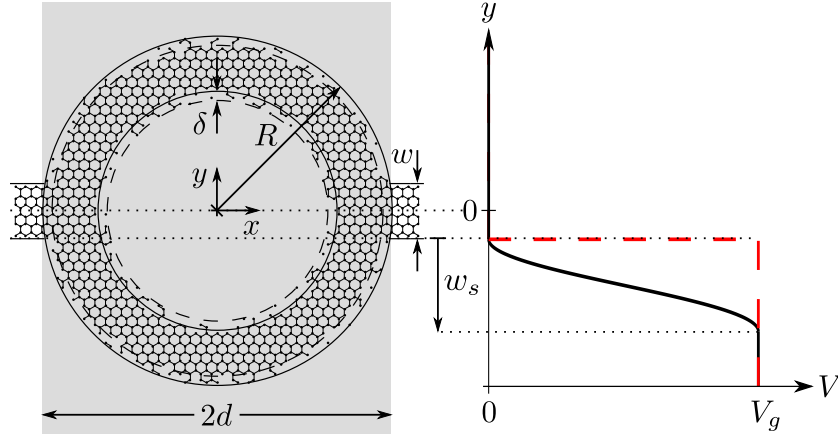
Figure 4.2: Schematic of the graphene ring structure (left) and the y-dependence of the on-site gate potential V (right) that is applied to the lattice sites on the lower arm of the ring. V exhibits either a smooth (black solid line) or sharp (red dashed line) profile along y-direction while being constant along x-direction. The width of the arms of the ring is chosen equal to the width w of the leads. The shaded area indicates the region of non-vanishing homogeneous magnetic field pointing out of plane. Different edge disorder configurations are realized by randomly removing sites within the two regions of width δ between dashed and solid circles (Figure adapted from Refs. [Sch10a, Sch12a]).

an electrostatic potential can be applied to one of the arms of the ring (see Fig. 4.2 for a schematic) such that this arm together with the two adjacent leads form either a $nn'n$- or npn-junction (n, n': conduction band transport, p: valence band transport). The former case corresponds to normal tunneling and the latter case to Klein tunneling. Then, the transmission properties strongly depend on the smoothness of the pn-interfaces. In particular, for sharp junctions the amplitude profile is symmetric around the charge neutrality point in the gated arm, whereas for smooth junctions the Aharonov–Bohm oscillations are strongly suppressed in the Klein tunneling regime as compared to the normal tunneling regime. Such a setup thus allows for a clear graphene-specific signature in Aharonov–Bohm measurements which seems to be readily observable. Its physical origin is the quantum interference of normal tunneling as well as Klein tunneling trajectories through the two arms of the ring.

In the following, we will introduce the tight binding model that we use for the transport analysis and afterwards, we will discuss our results in the different transport regions which show the interplay of the Aharonov–Bohm effect and Klein tunneling in phase-coherent graphene nanostructures.

Model

The calculation is based on the usual tight binding Hamiltonian for graphene,

$$H = \sum_i V_i |i\rangle\langle i| + \sum_{\langle i,j\rangle} t_{ij} |i\rangle\langle j|, \tag{4.1}$$

where the second sum runs over nearest neighbors and $V_i = V(\mathbf{r}_i)$ is a position-dependent on-site potential, taking the origin of coordinates at the center of the ring. The graphene
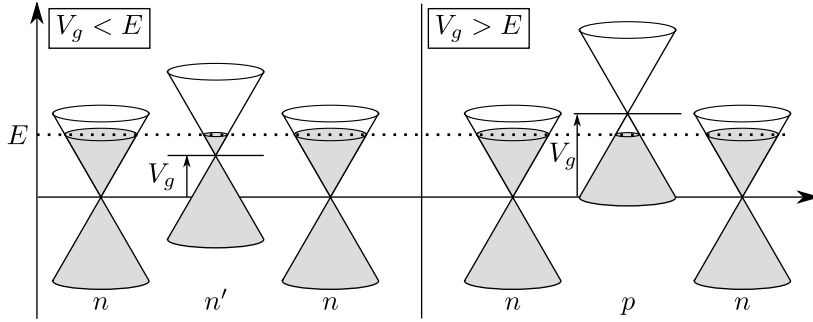
Figure 4.3: Schematic of the influence of the potential profile introduced by V_g on the spectrum of the lower arm of the ring. The left hand side shows the normal tunneling case ($nn'n$-junction) and the right hand side the Klein tunneling case (npn-junction) (Figure adapted from Refs. [Sch10a, Sch12a]).

hopping integral $t \approx 2.7\,\mathrm{eV}$ picks up a Peierls phase[4] [Pei33] in the presence of a magnetic field, yielding for the nearest neighbor coupling element the expression

$$t_{ij} = -t \exp\left(\frac{2\pi\mathrm{i}}{\Phi_0} \int_{\mathbf{r}_i}^{\mathbf{r}_j} \mathbf{A}(\mathbf{r})\,\mathrm{d}\mathbf{r}\right), \tag{4.2}$$

where the line integral is taken along the straight path between sites i and j. $\Phi_0 = h/e$ is the magnetic flux quantum and

$$\mathbf{A}(\mathbf{r}) = -By\Theta(d - |x|)\hat{\mathbf{e}}_x \tag{4.3}$$

with $d = \sqrt{R^2 - w^2/4}$ is the vector potential giving rise to a homogeneous magnetic field

$$\mathbf{B}(\mathbf{r}) = \boldsymbol{\nabla} \times \mathbf{A}(\mathbf{r}) = B\Theta(d - |x|)\hat{\mathbf{e}}_z. \tag{4.4}$$

The system under consideration is a ring-shaped structure cut out of a graphene sheet which is attached to two crystalline leads also modeled using the graphene lattice structure (see Fig. 4.2). Besides the magnetic field, the structure is also subject to a gate electrode potential V_g located on top of the lower arm of the ring. The smoothness of the potential interface is controlled via the smoothing width w_s measured from the lower edges of the leads:

$$\begin{aligned} V &= 0 && \text{for} \quad y \geq -w/2, \\ V &= V_g && \text{for} \quad y \leq -w/2 - w_s, \\ 0 &< V < V_g && \text{otherwise.} \end{aligned}$$

In the presented simulations, a cosine-shaped smoothing profile is used and $0 \leq w_s \leq R - 3w/2$.

For a Fermi energy $E > 0$, together with the adjacent leads this lower arm forms either a $nn'n$- or npn-junction for $V_g < E$ and $V_g > E$, respectively (see Fig. 4.3 for a schematic; the Fermi energy is measured relative to the charge neutrality point in the leads). Note that the setup exhibits a flat potential profile for trajectories along the upper ring arm,

---

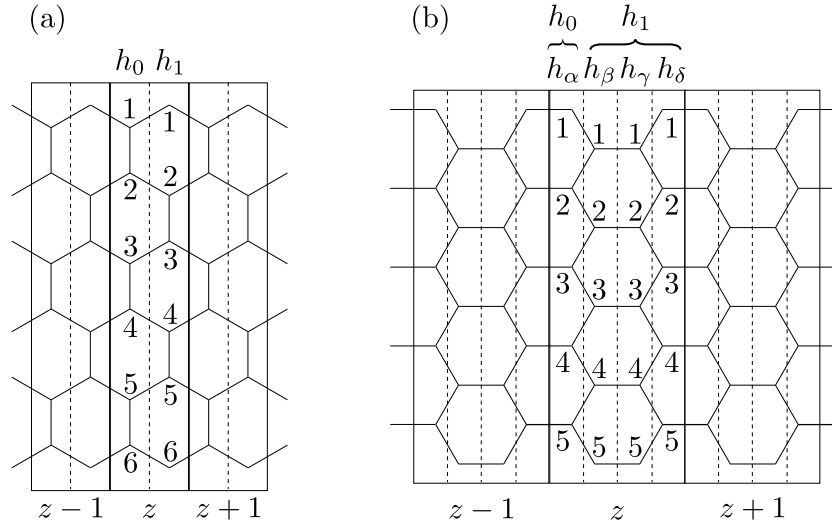[4] See Appendix F of Ref. [Wim09a] for a derivation.

Figure 4.4: Graphene leads in (a) zigzag and (b) armchair orientation, as well as their decomposition of unit cells (solid lines) into subcells (dashed lines) according to Fig. 2.3(a). The enumeration of lattice sites within a subcell is also indicated. In the zigzag case, half of the lattice sites can be eliminated by employing the effective description of the lead, see Fig. 2.3(b), while in the armchair case even 3 out of 4 lattice sites can be eliminated, thus greatly reducing the size of the matrices that describe the lead (Figure adapted from Ref. [Sch10a]).

i.e., a *nnn*-junction since there is no gate potential applied. This enables a rather large transmission through the ring even when the lower ring arm is tuned towards the Dirac point since transport through the upper arm always takes place at an energy distance E away from the charge neutrality point.

We derive the transmission function through the ring from the *S*-matrix via Eq. (2.9) in the Landauer–Büttiker formalism for elastic transport at zero temperature assuming complete phase-coherence. The semi-infinite left and right leads are described through their respective real-space surface Green's functions, and below we will outline their explicit construction for the case of a graphene lattice according to the method presented in Section 2.3. The coupling of the leads via the Hamiltonian describing the ring structure is realized following the recursive scheme introduced in Section 2.4.

Surface Green's function and definition of layers

Fig. 4.4 shows two particularly simple choices of boundary conditions (or lattice orientations) for a lead exhibiting the graphene lattice structure, namely zigzag and armchair orientations, which are named after the microscopic shape of the edges (also see Fig. 3.3).[5] By comparison with Fig. 2.3 and Eq. (2.14), we find for the case of a zigzag edge (see Fig. 4.4(a)) the subcell matrices h_{01}, h_{10}, and h_k, $k \in \{0,1\}$, whose non-zero elements can be parameterized in a

---

[5] The subdivision of the graphene lead unit cell as depicted in Fig. 4.4 has also been previously used in Ref. [Xu08].

compact form ($i \in \mathbb{N}$):

$$(h_k)_{ii} = V_0,$$
$$(h_k)_{2i+k-1,2i+k} = -t_0 = (h_k)_{2i+k,2i+k-1},$$
$$(h_{01})_{ii} = -t_0 = (h_{10})_{ii},$$

where we assumed $t_0 \in \mathbb{R}^+$ and a constant on-site matrix element $V_0 \in \mathbb{R}$. Of course, the roles of h_0 and h_1 are interchangeable, depending on the details of the lead surface. Obviously, the effective coupling matrix (see Eq. (2.15))

$$\tilde{H}_c = h_{01}(E - h_1)^{-1}h_{10} = t_0^2(E - h_1)^{-1}$$

is invertible, in contrast to the coupling matrix H_c in the non-effective description, which is clearly non-invertible since there are lattice sites within the unit cell that do not couple to the previous unit cell, as was the case in Eq. (2.13). Additionally, the size of the matrices describing the effective lead is smaller by a factor of two compared to the original description, yielding increased performance of the computational routines.

The performance gain is even larger in the case of graphene leads with armchair edges (see Fig. 4.4(b)) since then only 1/4 of the atomic sites within a particular unit cell couple to the previous cell. We find

$$h_0 = h_\alpha, \qquad\qquad h_{01} = (h_{\alpha\beta}, 0, 0),$$

$$h_1 = \begin{pmatrix} h_\beta & h_{\beta\gamma} & 0 \\ h_{\beta\gamma}^\dagger & h_\gamma & h_{\gamma\delta} \\ 0 & h_{\gamma\delta}^\dagger & h_\delta \end{pmatrix}, \qquad\qquad h_{10} = \begin{pmatrix} 0 \\ 0 \\ h_{\delta\alpha} \end{pmatrix},$$

where

$$h_\alpha = h_\beta = h_\gamma = h_\delta = V_0 \cdot \mathbf{1}, \qquad h_{\beta\gamma} = h_{\delta\alpha} = -t_0 \cdot \mathbf{1},$$

and the non-vanishing matrix elements of $h_{\alpha\beta} = h_{\gamma\delta}^\dagger$ are given by

$$(h_{\alpha\beta})_{ij} = -t_0(\delta_{ij} + \delta_{i-1,j}).$$

Again, the labels α, β, γ, and δ are interchangeable depending on the details of the lead surface.

One point to note is that $\tilde{H}_c$ is not well defined for energy values E matching the eigenvalues of h_1. In the case of zigzag edges, this corresponds to the choices $E = V_0$ and $E = V_0 \pm t_0$. The choice $E = V_0$ corresponds to the charge neutrality point in graphene. In bulk graphene, the density of states vanishes at this point and hence there are no propagating bulk modes in the lead that may contribute to the current. The zigzag edge supports an additional edge state, which can in principle carry current; however, at the charge neutrality point, the band describing the edge states becomes completely flat, leading to a divergent density of states, a vanishing group velocity, and therefore vanishing current (see Fig. 3.3). Thus, at $E = V_0$, there are no current-carrying modes available in the leads. The singularity at $E = V_0 \pm t_0$ corresponds to the high-energy van Hove singularity in graphene, where the density of states

diverges. In the armchair case, except for the singularity at the charge neutrality point, there are only such singularities for $|E - V_0| > t_0$. Since for the remainder of this work we will only be interested in the low-energy properties of graphene, $|E - V_0| \ll t_0$, these singularities do not pose any problem.[6]

For the recursive scheme introduced in Section 2.4, we employ a simple partitioning of the Hamiltonian which divides the ring area into layers $H_1, \ldots, H_{N_S}$ (see Eq. (2.16) and Fig. 2.4), that proceeds in the very same fashion as the decomposition of the lead unit cell into subcells, see Fig. 4.4. The width Δx of each layers in this natural ordering [Wim09b] along x-direction is given by $\Delta x/a_0 = \sqrt{3}/2$ in the zigzag case and $\Delta x/a_0 = 3/4$ in the armchair case. A slightly more efficient way of defining layers is given by following the optimization approach developed in Refs. [Wim09a, Wim09b], as already discussed in Section 2.5.

Results

In the following, we present transmission properties for a ring with $R = 300a_0$ and $w = 60a_0$, $a_0 \approx 0.142\,\text{nm}$ being the nearest neighbor distance in graphene, in terms of the linear conductance $G = 2e^2/h \times \text{tr}\left(\hat{t}^\dagger \hat{t}\right)$, where the factor 2 accounts for spin degeneracy and $\hat{t}$ is the $N \times N$ transmission matrix between the two leads, i.e., the lower left block of the unitary scattering matrix S,

$$S = \begin{pmatrix} \hat{r} & \hat{t}' \\ \hat{t} & \hat{r}' \end{pmatrix}.$$

N is the number of propagating modes in the leads. Edge disorder is applied to the ring by randomly removing sites within a width δ from the inner and outer edges of the ring, respectively (see Fig. 4.2). We choose $\delta = 1.5a_0$ in order to keep the edge of the ring as smooth as possible while still allowing for different edge disorder configurations. Fermi energy E and gate potential V_g are chosen such that transport always takes place in between the van Hove singularities located at $E = \pm t$, where the density of states diverges in the tight binding model of graphene, $0 < E < t$, $0 \leq V_g \leq 2E$. In Fig. 4.5, we plot the magnetoconductance at Fermi energy $E = 0.5t$ and zero gate voltage ($V_g = 0$) for a particular ring realization showing pronounced Aharonov–Bohm oscillations on top of a low-frequency background. The background signal results from universal conductance fluctuations (UCF) which are typical for phase-coherent mesoscopic devices [Dat05]. The behavior is in agreement with the observations made in Ref. [Wur10], where the authors investigate an even wider magnetic field range up to the quantum Hall regime. In Fig. 4.6, we also show the corresponding frequency spectrum obtained from a Fourier transform of the magnetoconductance signal up to $B = 10^{-3}\Phi_0/a_0^2$ as well as the UCF background signal and the magnetooscillations after background removal by means of a high pass frequency filter. The contributions to the Aharonov–Bohm oscillations are centered around $(\Delta B a_0^2 e/h)^{-1} \sim 2.3 \times 10^5$. Using $\tilde{R}^2 \pi \Delta B = h/e$, this frequency corresponds to a mean radius $\tilde{R} \sim 270a_0$ of interfering electron trajectories, which perfectly lies within the boundaries of the ring.

In Fig. 4.7, we show the same plot for $E = 0.1t$. The oscillations diminish at $B a_0^2 e/h \sim$

---

[6] Note that also the alternative algorithms developed in Ref. [Wim09a] are based on a classification of propagating modes according to the sign of the group velocity. Therefore, they are also not applicable at band edges, i.e., in the case of vanishing group velocities and a divergent density of states.
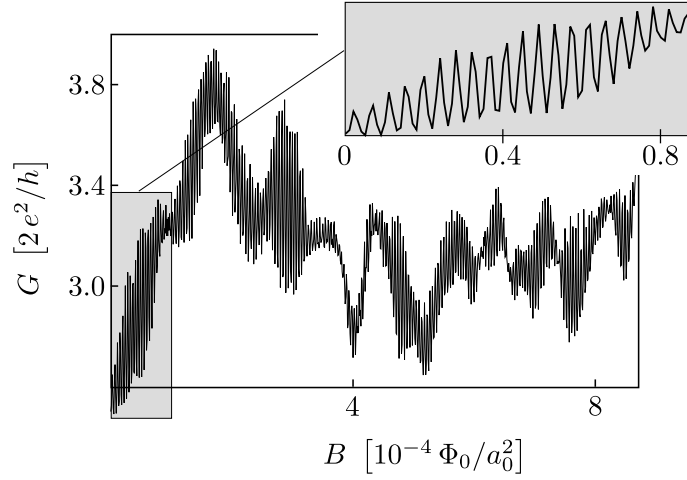
Figure 4.5: Magnetoconductance of a ring with $R = 300a_0$ and $w = 60a_0$ at energy $E = 0.5t$ and zero gate voltage showing clear Aharonov–Bohm oscillations on top of a background signal which is due to universal conductance fluctuations (Figure adapted from Refs. [Sch10a, Sch12a]).
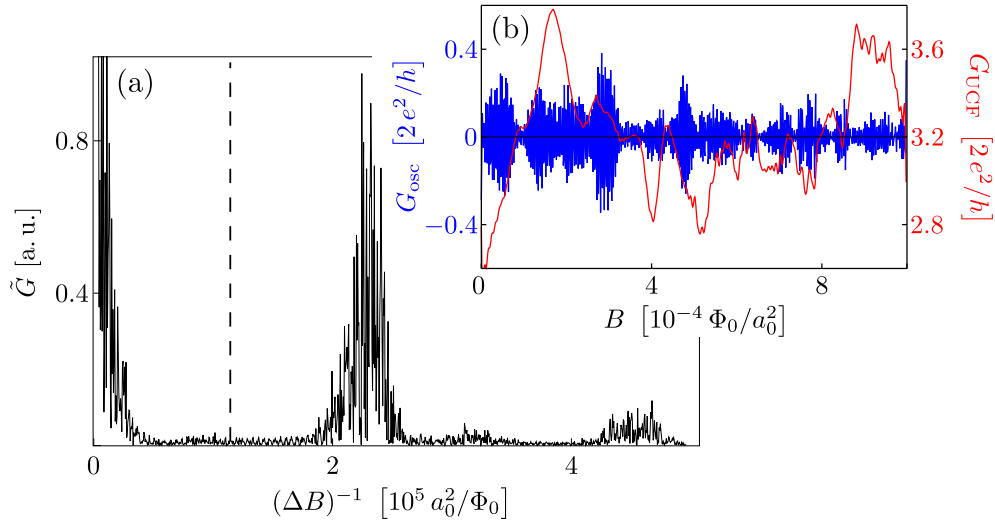

Figure 4.6: (a) Frequency spectrum corresponding to Fig. 4.5, obtained from the Fourier transform $\tilde{G}$ of the magnetoconductance G. Besides the low frequency background and the fundamental oscillation component, the second harmonic is also slightly visible in the spectrum. The dashed line indicates the frequency limit of the high pass frequency filter used for background subtraction. (b) UCF background signal (red) and magnetooscillations (blue) corresponding to Fig. 4.5 after background subtraction (Figure adapted from Refs. [Sch10a, Sch12a]).
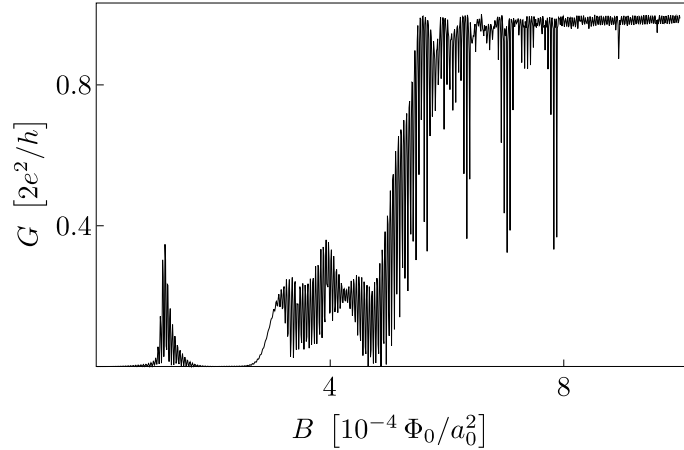
Figure 4.7: Magnetoconductance of a ring with $R = 300a_0$, $w = 60a_0$ at energy $E = 0.1t$ and zero gate voltage, showing the onset of the quantum Hall regime. Note: The conductance is still finite near zero magnetic field, which is not visible on this scale (Figure adapted from Ref. [Sch10a]).

6×10^{-4}. This field strength marks the onset of the quantum Hall regime, where the cyclotron diameter becomes comparable to the width of the arms of the ring; an estimate [Wur10] of the graphene cyclotron diameter $d_c = 2E/(v_F eB)$, taking the Fermi velocity at the Dirac point in graphene, $v_F = 3\pi t a_0/h$, yields $d_c \sim 40a_0$, a value of same order of magnitude as the width $w = 60a_0$.

By applying a gate voltage $V_g > 0$ to one of the ring arms, the magnitude of the Aharonov–Bohm oscillations may be modified. A convenient measure of the oscillation magnitude is the root mean square (RMS) amplitude of the signal. Prior to the RMS analysis, the UCF background has to be removed from the signal. This is achieved by applying a high pass frequency filter to the Fourier transform of the magnetoconductance data as indicated in Fig. 4.6(a). The retained unbiased signal is squared and the root of the average over the squared signal is defined as the RMS amplitude ΔG_{RMS}.

In Fig. 4.8(a), we show the dependence of the RMS oscillation amplitude ΔG_{RMS} on the gate voltage V_g for different smoothing widths w_s (see Fig. 4.2) at energy $E = 0.5t$, where the average is taken over the range $0 \leq Ba_0^2/\Phi_0 \leq 10^{-3}$. Increasing the gate voltage from zero towards the neutrality point $V_g = E$ not only leads to increased potential scattering but also to a reduction in the number of accessible propagating states in the lower arm of the ring. As can be seen in Fig. 4.8(a), the oscillation amplitude diminishes and reaches a minimum value at the neutrality point. Note that since the transmission through the upper ring arm is not at all affected by a gate potential, the overall conductance itself is only slightly changed to fluctuate around $2.5 \times 2e^2/h$ (see Fig. 4.9) as compared to values around $3.4 \times 2e^2/h$ in the case of zero gate potential on the lower ring arm (see Fig. 4.5).

For $V_g < E$, the decay of the RMS amplitude towards the neutrality point does not depend on the details of the gate potential interface. However, in the regime of Klein tunneling, $V_g > E$, the oscillation behavior strongly depends on the smoothness of the gate potential. In case of a smooth potential, the partial waves in the lower arm have to tunnel through a finite region of low density of states, where $V \sim E$ (see Fig. 4.2), in order to interfere with
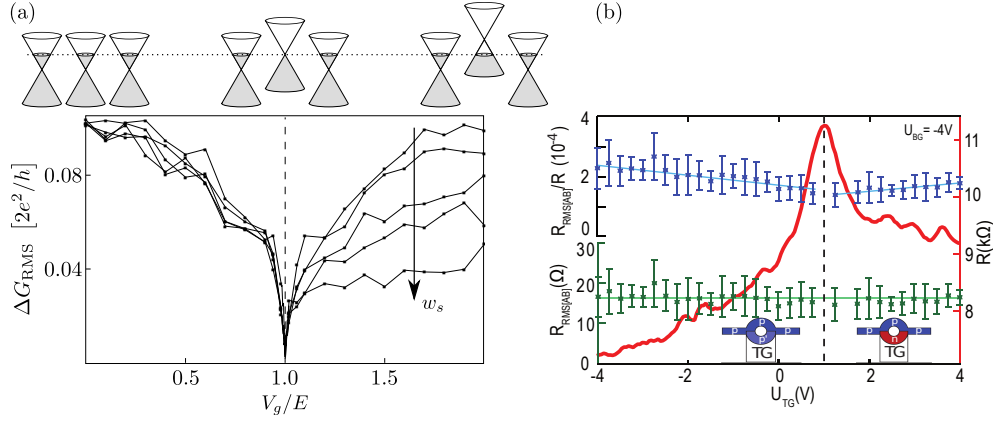
Figure 4.8: (a) RMS analysis for the setup used in Fig. 4.5 for different smoothing widths $w_s/a_0 \in \{0, 21, 52.5, 105, 210\}$. Each data point results from an average over five realizations of edge disorder. The corresponding standard deviations lie between $0.005 \times 2e^2/h$ and $0.015 \times 2e^2/h$ but are suppressed for better visibility. For better clarity, the spectrum schematics (see Fig. 4.3) are also included (Figure adapted from Refs. [Sch10a, Sch12a]). (b) A corresponding measurement from Ref. [Smi12]; parameters are given in the text. For a broad range of values of the top gate voltage U_{TG} applied to the lower arm resulting in either a *pp′p*- or *pnp*-junction as schematically shown, the background resistance R (red) as well as the absolute (green) and relative (blue) resistance oscillation amplitudes $R_{\mathrm{RMS[AB]}}$ and $R_{\mathrm{RMS[AB]}}/R$ are shown. The dashed line indicates the effective position of the charge neutrality point (Figure adapted from Ref. [Smi12]).
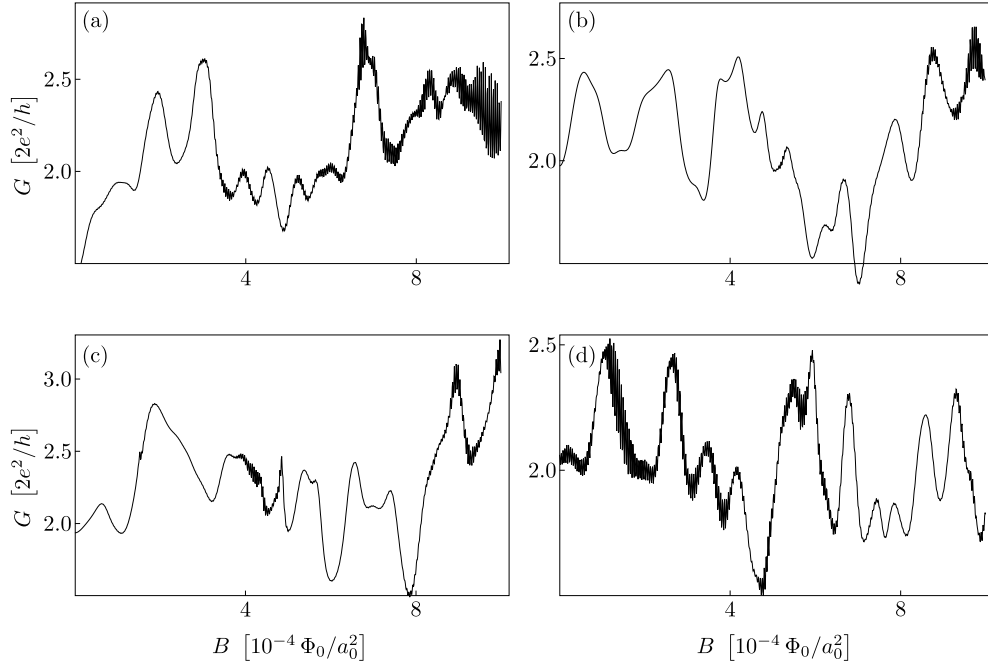

Figure 4.9: Magnetoconductance of a ring with $R = 300a_0$ and $w = 60a_0$ tuned close to the neutrality point in the lower arm with a smooth potential interface ($w_s = 210a_0$). The plots (a)–(d) constitute a representative selection and are obtained by a variation of the microscopic edge disorder configuration (which is always chosen randomly) for values $V_g/E = 1.00 \pm 0.01$ (Figure adapted from Ref. [Sch10a]).

the partial waves traversing the upper arm. The lower arm becomes increasingly penetrable as this region gets narrower, until it gets transparent in case of a sharp potential. This reflects the usual behavior of Klein tunneling phenomena, where the probability for tunneling through a *pn*-junction depends on the smoothness of the *pn*-interface [Bee08a, Che06].

Just recently, a corresponding experiment has been conducted on a graphene ring with inner and outer radii $r_i = 220\,\text{nm}$ and $r_o = 360\,\text{nm}$ in the diffusive regime with a mean free path of approximately $105\,\text{nm}$, a charge carrier density of $8.6 \times 10^{11}\,\text{cm}^{-2}$, and an observed oscillation period of $16.5\,\text{mT}$, which corresponds to an effective radius of $\tilde{r} \approx 285\,\text{nm}$ [Smi12]. A back gate voltage $U_{BG} = -4\,\text{V}$ determines the Fermi level in the system for a vanishing voltage $U_{TG} = 0\,\text{V}$ on the top gate, which is applied to one of the ring arms to give either a $pp'p$- or pnp-junction. The measurement, shown in Fig. 4.8(b), extends over a broad range of values for U_{TG}, thus complementing our analysis, where we considered limiting cases of a *nnn*- and *npn*-junction with equal doping levels in the ring arms and the leads, corresponding to $U_{TG} \sim 0\text{–}2\,\text{V}$ in the experimental situation, see Fig. 4.8(a). In particular, the authors mention that there is no clear observation of Aharonov–Bohm oscillations at the charge neutrality point, as is the case in the numerical simulations, while away from the charge neutrality point, the oscillation amplitude is essentially constant—a behavior that might already be indicated by the saturation of the oscillation amplitude away from the charge neutrality point in Fig. 4.8(a). Unfortunately, from this experiment, it is not clear how the oscillation amplitude behaves in a close vicinity around the Dirac point, e.g., for values $U_{TG} \approx 0.75\text{–}1.25\,\text{V}$, and how it depends on the smoothing width.

The described behavior of the RMS amplitude (see Fig. 4.8(a)) is robust over the whole energy range under consideration, except for an increasing uncertainty at lower values for the Fermi energy. Although all results are presented for zigzag boundary conditions in the leads, the effects are independent of a change of orientation of the graphene lattice to armchair boundaries in the leads.

Finally, we mention here an additional observation concerning the dependence of the magnitude of the Aharonov–Bohm oscillations on the magnetic field strength B when the lower arm of the ring is tuned near the neutrality point (see Fig. 4.9). It seems that in this regime the oscillation magnitude is in general significantly lower for low field strengths compared to the oscillations at higher field strengths. This is indeed the case for most of the ring realizations we investigated though not for all of them (see Fig. 4.9(d)). The reason for such a behavior is so far not understood. Since the increase in the oscillation magnitude cannot be related to any particular length scale, a connection to the quantum Hall effect seems unlikely.

In summary, Klein tunneling in graphene exhibits clear signatures in the Aharonov–Bohm oscillations observed in mesoscopic rings. In the next section, we will show how another graphene-specific effect, namely specular Andreev reflection at a graphene–superconductor interface [Bee06], can be identified in such nanostructures.

4.3 How to distinguish specular from retro Andreev reflection in graphene rings

In this section, we present numerical transport calculations of Andreev reflection in a graphene ring system threaded by a magnetic flux and attached to one normal conducting and one superconducting lead. To this end, the Bogoliubov–de Gennes equation [Gen99] for the tight binding model using the recursive Green's functions technique is solved within the Landauer–Büttiker framework for elastic transport. By tuning chemical potential and bias voltage, it is possible to switch between regimes where electron and hole originate from the same band ("retro configuration") or from different bands ("specular configuration") of the graphene dispersion, respectively. Andreev reflection is known to be closely related to the effect of Klein tunneling discussed in the previous section [Bee08b]. However, different aspects of Klein tunneling have become experimentally accessible in the last years [Sta09, You09] whereas specular Andreev reflection has not been observed to date although there exist a number of proposals for the experimental control [Che09b] and detection [Bee06, Tit07b, Che11] of this process. (For a review on both effects, see Ref. [Bee08a].) Here, we review a novel approach concerning the identification of specular Andreev reflection, distinguishing it from conventional retro reflection, and discuss the advantages over previous works in the field. We find that the dominant contributions to the Aharonov–Bohm oscillations in the subgap transport, i.e., in the absence of propagating modes in the superconducting lead, are of period $h/(2e)$ in retro configuration, whereas they are of period h/e in specular configuration. This result confirms the predictions obtained from a qualitative analysis of interfering scattering paths and since it is robust against disorder and moderate changes of the system, it provides a clear signature to distinguish both types of Andreev reflection processes in graphene.

Scattering path analysis

Our approach is based on the observation that in general, the probability for an incident electron to be reflected as a hole is less than one. This allows for effects typical for phase-coherent mesoscopic devices, such as universal conductance fluctuations or Aharonov–Bohm oscillations [Aha59] in the magnetoconductance. While in normal metals the fundamental period of these oscillations is given by the flux quantum $\Phi_0 = h/e$, it is half the value for Andreev (retro) reflection in conventional metals due to the charge $2e$ of a Cooper pair. However, this is not true anymore in the case of specular Andreev reflection, therefore providing a criterion to distinguish between specular and retro reflection. In order to show this, we consider the phases due to the magnetic flux that are picked up by the various scattering paths. In this analysis, we restrict ourselves to the contributions up to first order in the sense that we take processes into account that involve only a single electron–hole conversion process and that contain at most one additional round-trip of electron or hole, respectively; higher order contributions connected with additional round-trips are often times negligible [Sch10a, Rus08]. The corresponding paths are summarized in Fig. 4.10. In order to obtain the magnetoconductance for the two types of Andreev reflection, we sum up the
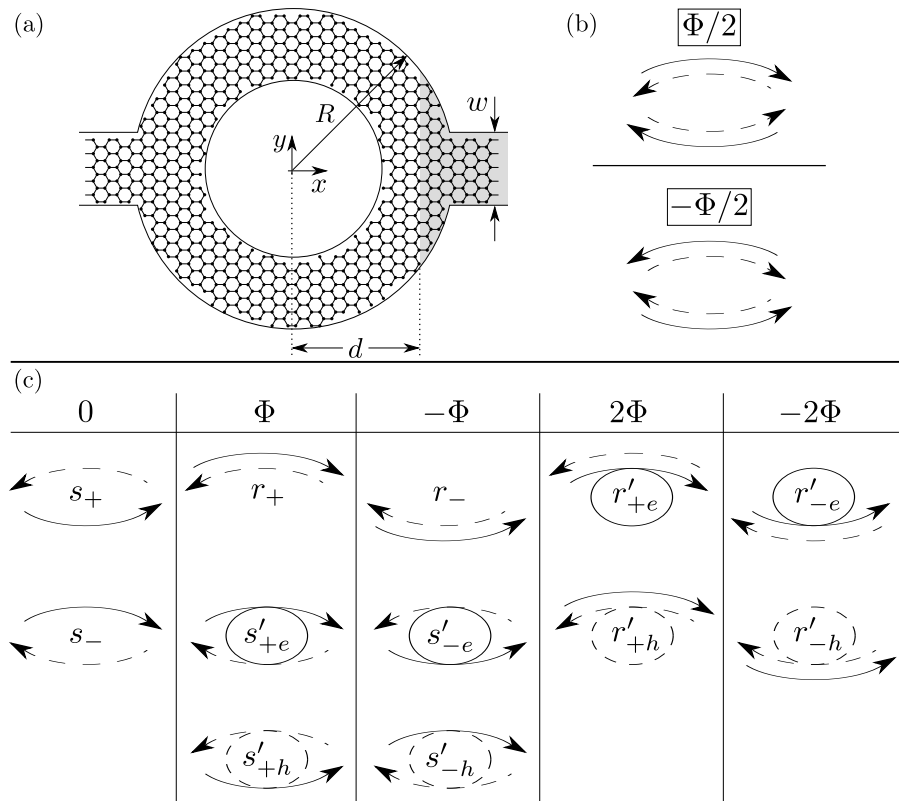
Figure 4.10: (a) Device geometry showing a graphene ring structure that is penetrated by a magnetic flux Φ measured in units of the flux quantum Φ_0. At the interface with the superconductor (shaded region), electron–hole conversion may occur. (b) The gauge is chosen such that each of the eight individual electron (solid lines) and hole (dashed lines) paths picks up a phase $\pm\Phi/2$ as indicated. (c) Scattering paths for electrons injected from and holes leaving through the left normal conducting lead; only zeroth and first order contributions are included, i.e., terms containing a single electron–hole conversion process and at most one additional round-trip of the electron or the hole. The paths are categorized according to the total phase that is picked up and each path is associated with a corresponding amplitude, where first order amplitudes are indicated by a prime (Figure adapted from Refs. [Sch12b, Sch12a]).

amplitudes as defined in Fig. 4.10 for the various paths coherently:

$$R_s(\Phi) \cong \left| s_+ + s_- + s'_+ e^{i\Phi} + s'_- e^{-i\Phi} \right|^2,$$

$$R_r(\Phi) \cong \left| r_+ e^{i\Phi} + r_- e^{-i\Phi} + r'_+ e^{2i\Phi} + r'_- e^{-2i\Phi} \right|^2,$$

where $s'_\pm = s'_{\pm e} + s'_{\pm h}$, $r'_\pm = r'_{\pm e} + r'_{\pm h}$, and Φ is the magnetic flux measured in units of the flux quantum Φ_0. Assuming $|s| \gg |s'|$ for any zeroth and first order amplitudes, respectively, we obtain

$$R_s(\Phi) \cong R_s^0 + 2 \operatorname{Re}\left((s'_+ s_0^* + s_0 s'^*_-) e^{i\Phi} \right) + \mathcal{O}\left[(s')^2 \right], \tag{4.5}$$

where $s_0 = s_+ + s_-$ and R_s^0 contains contributions that are constant with respect to Φ. Therefore, in the case of specular reflection, oscillations of period h/e are dominant. In contrast, in the case of retro reflection, contributions of period $h/(2e)$ are dominant as expected:

$$R_r(\Phi) \cong R_r^0 + 2 \operatorname{Re}\left(r_+ r_-^* e^{2i\Phi} \right) + \mathcal{O}\left[rr', \ (r')^2 \right], \tag{4.6}$$

where again R_r^0 contains Φ-independent terms and we assume $|r| \gg |r'|$ for any zeroth and first order amplitudes, respectively.

Numerical model

In order to test the previous analysis on the basis of a microscopic model, we implement the Bogoliubov–de Gennes Hamiltonian from the mean-field description of superconductivity [Gen99],

$$\mathcal{H} = \begin{pmatrix} H - E_F & \boldsymbol{\Delta} \\ \boldsymbol{\Delta} & E_F - H^* \end{pmatrix}, \tag{4.7}$$

within the tight binding formalism of graphene, Eq. (4.1). In this numerical calculation, all higher order contributions beyond the ones discussed in the previous subsection are also taken into account. In Eq. (4.7), we assume $\Delta_i = \Delta(\mathbf{r}_i) \in \mathbb{R}$ for the superconducting order parameter $\boldsymbol{\Delta} = \sum_i \Delta_i |i\rangle\langle i|$. The presence of a magnetic field is captured by a Peierls phase in the hopping matrix element, see Eq. (4.2).

The structure of the graphene device under consideration is schematically shown in Fig. 4.10. The two semi-infinite leads also exhibit the graphene lattice structure. Superconductivity is induced into the right lead due to the proximity effect [Hol32, Gen99] of a superconducting electrode on top of the graphene. We choose to orient the leads to exhibit armchair edges and later comment on the reason for this particular choice. The whole ring is penetrated by a uniform perpendicular magnetic field of strength B described by the vector potential (4.3). The origin of coordinates is taken at the center of the ring.

In order to fulfill the mean-field requirement of superconductivity, which demands the superconducting coherence length $\xi = \hbar v_F / \Delta$ to be large compared to the wavelength λ_S in the superconducting region [Bee06], we introduce additional doping into the superconducting region by applying a gate potential $V_i = V_g \Theta(x_i - d)$. The type of Andreev reflection that occurs at the NS interface is then determined by the excitation energy ε (i.e., the eigenvalues of Eq. (4.7)) and the Fermi energy E_F as shown in Fig. 4.11. In "retro configuration", $E_F > \varepsilon > 0$, where $v_y^{(h)} v_y^{(e)} < 0$ for the y-components of the electron and hole velocities,
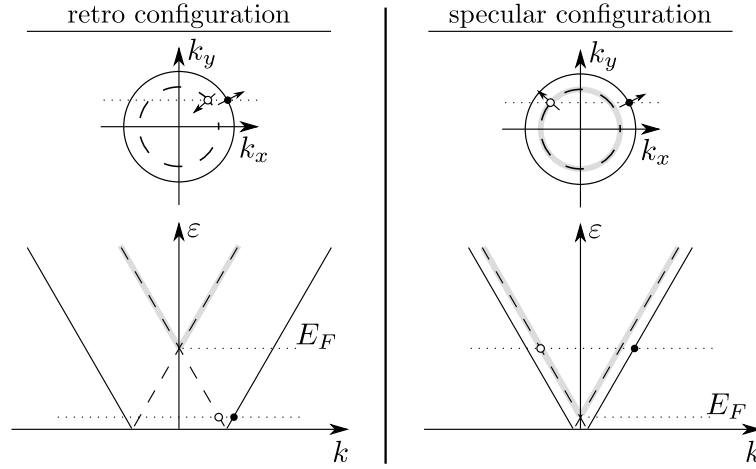
Figure 4.11: Schematics of the (radially symmetric) excitation spectrum (lower panel) and surfaces of constant excitation energy in **k**-space (upper panel) in the cases $E_F > \varepsilon > 0$ ("retro configuration") and $0 < E_F < \varepsilon$ ("specular configuration"), respectively. Solid and dashed lines indicate electron- and hole-like states, respectively; (hole) states originating from the valence band are shaded. The small arrows in the upper panel indicate the direction of propagation of the corresponding states. Electron–hole excitations are drawn assuming conservation of k_y at the NS interface (Figure adapted from Refs. [Sch12b, Sch12a]).

both electron and hole traverse the same arm of the ring. In "specular configuration", $0 < E_F < \varepsilon$, the hole is reflected back through the other arm of the ring since $v_y^{(h)} v_y^{(e)} > 0$. In the following, we choose $|V_g| \gg E_F$ justifying the adoption of the step-function model for the superconducting order parameter, $\Delta_i = \Delta\Theta(x_i - d)$ [Bee06].

In order to compare retro (r) and specular (s) configurations, we will choose $\varepsilon^{(r)} = E_F^{(s)}$ and $\varepsilon^{(s)} = E_F^{(r)}$ since then the states in both configurations exhibit the same wavelength and there is the same number of propagating modes. We further choose $\varepsilon^{(r)}, E_F^{(s)} \ll \varepsilon^{(s)}, E_F^{(r)}$ so that for nearly each value of k_y there exist electron–hole scattering channels.

Again, the transport properties of the system are obtained from the scattering matrix S that is calculated in the framework of the Landauer–Büttiker formalism using Eq. (2.10) and the recursive scheme introduced in Section 2.4. The decomposition of the ring Hamiltonian into layers and the construction of the effective leads according to Section 2.3 proceed as in Section 4.2. In this framework for elastic transport, Green's function and scattering matrix are parameterized by the eigenvalues ε of the Hamiltonian (4.7).

In the following, we will concentrate on the regime $\varepsilon < \Delta$ in which there are no propagating modes in the superconducting lead so that electrons injected from the normal conducting lead are reflected back either as electron (e) or hole (h). The scattering matrix thus has the structure

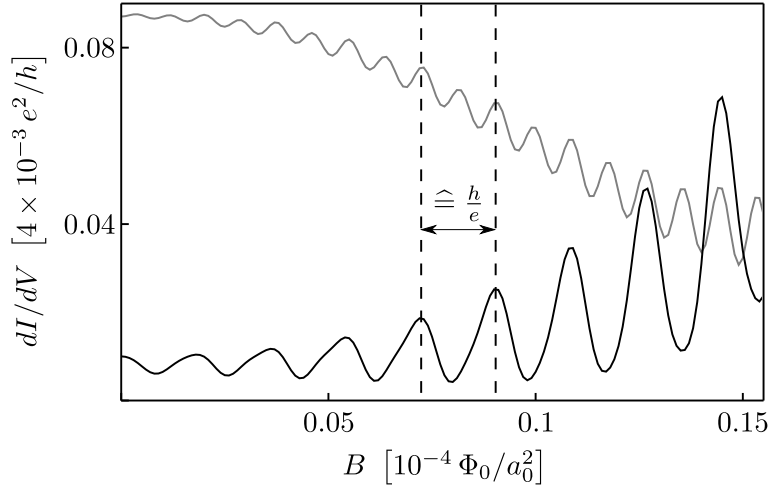$$S = \begin{pmatrix} r_{ee} & r_{eh} \\ r_{he} & r_{hh} \end{pmatrix},$$

Figure 4.12: Differential magnetoconductance for specular (black) and retro (gray) configuration for $E_F^{(r)} = 0.025t = \varepsilon^{(s)}$, $E_F^{(s)} = 0.001t = \varepsilon^{(r)}$, corresponding to 8 modes in the normal conducting lead including all degeneracies (spin, valley, electron/hole). The high doping in the superconducting lead is chosen such that $E_F - V_g = 0.5t$ in both cases. Other parameter values are provided in the main text. The period of the dominant oscillation is $B_0^{(s)} \approx 1.8 \times 10^{-6} a_0^{-2} h/e$ in specular configuration and $B_0^{(r)} \approx 8.8 \times 10^{-7} a_0^{-2} h/e \approx 0.5 B_0^{(s)}$ in retro configuration. The weak beating pattern in retro configuration and the asymmetry in specular configuration arise due to minor contributions of contrary frequencies (Figure adapted from Refs. [Sch12b, Sch12a]).

from which the differential conductance for the Andreev processes is given by

$$\frac{\mathrm{d}I}{\mathrm{d}V} = \frac{4e^2}{h} \times \mathrm{tr}\left(r_{he}^\dagger r_{he}\right),$$

where the factor 4 accounts for spin degeneracy and the quantization of charge in units of $2e$.

Results

In Fig. 4.12, we show the calculated transmission for a ring of width $w = 87\sqrt{3}a_0$ and outer radius $R = 500a_0$, where a_0 is the distance between nearest neighbors. The transmission function exhibits Aharonov–Bohm oscillations on top of a low frequency background which is due to universal conductance fluctuations. The position of the NS interface is given by $d = 400a_0$. The chosen dimensions of the ring are large enough to exclude finite-size effects while still being numerically manageable. For the superconducting order parameter we choose a value of $\Delta = 0.03t \approx 80\,\mathrm{meV}$ which may appear unrealistic at first sight considered the fact that typical values are up to a few meV [Kit96]. However, by making this choice, we scale the value of the superconducting order parameter according to the scale of the system size such that the dimensionless factor $(\Delta R)/(\hbar v_F)$ stays of same order of magnitude compared with values realized in experiments [Rus08, Hue10]. Thus, for a realistic system size of $R \sim 10^{-6}\,\mathrm{m}$, our choice of Δ would correspond to a value of a few meV for the superconducting gap. Note that due to these low energy scales and the rather large spacing
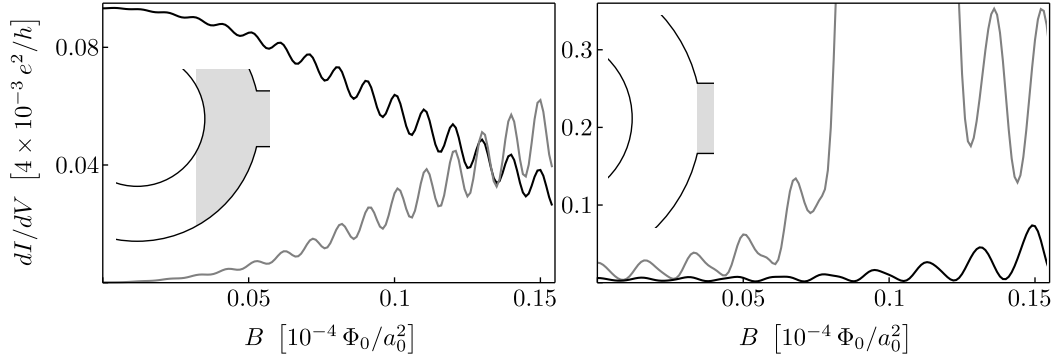
Figure 4.13: Breakdown of the h/e vs. $h/(2e)$ signature for shifted positions of the NS interface as explained in the text. Other parameters and color coding are chosen as in Fig. 4.12. For $d = 340a_0$ (left) in specular configuration, one observes oscillations of period $h/(2e)$ as in retro configuration. For $d = 490a_0$ (right), contributions of specularly reflected holes in retro configuration become important, leading to the observation of additional h/e-oscillations. The value of the superconducting coherence length is $\xi = 50a_0$ (Figure adapted from Refs. [Sch12b, Sch12a]).

of modes resulting from the narrow geometry of the electron waveguides in such a ring structure, in specular configuration only the regime of a low number of modes is accessible. Also note that due to strong electron backscattering at the front of the hole and at the rough edges of the ring, the average value of the differential conductance is much less than a conductance quantum, e^2/h.

The average radius $\bar{r}$ of the scattering path is calculated according to $\bar{r}^2 \pi B_0 = (h/e)/n$, where $n = 1$ ($n = 2$) in specular (retro) configuration and B_0 is the (dominant) period of the oscillation. Evaluating the period of the oscillations shown in Fig. 4.12, we obtain $\bar{r}^{(s)} \approx 420a_0$ in specular configuration and $\bar{r}^{(r)} \approx 425a_0$ in retro configuration. The obtained values lie well within the inner and outer radius of the ring and close to the arithmetic mean $R - w/2 \approx 425a_0$, therefore confirming the predictions obtained from Eqs. (4.5) and (4.6). Minor contributions of period h/e in retro configuration and $h/(2e)$ in specular configuration visible in Fig. 4.12 may arise due to terms neglected in Eqs. (4.5) and (4.6), scattering off the sharp boundaries of the ring structure, and the fact that for the electron–hole conversion at the NS interface k_y is not strictly conserved.

Another strong evidence that supports our interpretation of the two different periods is the breakdown of this particular signature that is observed for a shift of the position of the NS interface on the scale of the width of the ring. Indeed, while in Ref. [Hau10]—where a three-terminal graphene junction is analyzed—the exact position of the NS interface has no effect, it matters in our case; the reason is that ξ is comparable or even less than the system size while in Ref. [Hau10], the superconducting coherence length greatly exceeds the system dimensions. If the interface is too close to the hole region (see Fig. 4.13(a) inset), then specularly reflected holes are forced to traverse the same arm as the incoming electron. In this case, one should observe $h/(2e)$ oscillations in specular configuration. In contrast, if the interface is too far from the hole (see Fig. 4.13(b) inset), holes may significantly be reflected through the other arm, e.g., due to increased scattering at the ring boundaries. This would manifest itself in the observation of h/e oscillations in addition to the $h/(2e)$ oscillations
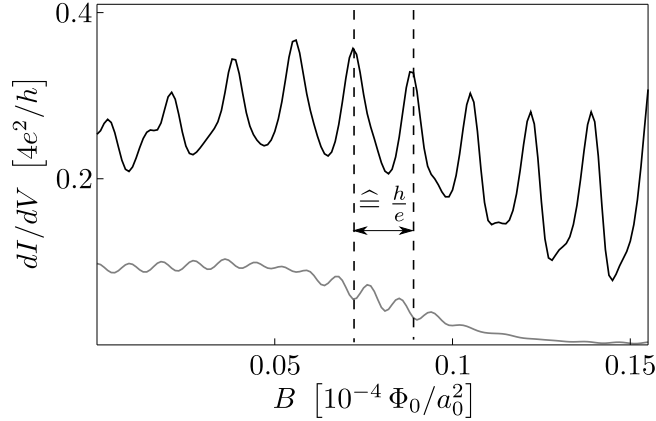
Figure 4.14: Differential magnetoconductance for $d = 430a_0$, $E_F^{(r)} = 0.029t = \varepsilon^{(s)}$, $E_F^{(s)} = 0.0001t = \varepsilon^{(r)}$, corresponding to twice the number of propagating modes compared to Fig. 4.12. Other parameters and color coding are chosen as in Fig. 4.12. Note that the magnetoconductance signal is strongly enhanced compared to Fig. 4.12 (Figure adapted from Ref. [Sch12a]).

in retro configuration. This behavior is confirmed in the observed magnetooscillations, as shown in Fig. 4.13.

Apart from that, the h/e vs. $h/(2e)$ signature proves to be very robust against moderate changes to the length and energy scales in the system, such as the extent of the magnetic field or the ratio of Fermi wavelength and the width of the NS interface. We also tested that the signature persists when more propagating modes are present in the lead, leading to values of the average conductance which are much larger compared to the few-mode situation shown in Fig. 4.12 (see Fig. 4.14). Additionally, the signature is hardly affected by bulk disorder, which is a major advantage of our setup. In Fig. 4.15, we show the magnetoconductance of the system used in Fig. 4.12 with a particular random short-range disorder configuration that is realized by applying an uncorrelated random on-site potential of Gaussian distribution with zero mean and width $\sigma = 0.01t$ to each site. In addition, the NS interface has been smeared out over a distance $l = 90a_0$ in this case. The robustness of the effect can be explained from the topological nature of the signature; since all microscopic scattering paths can be classified into just two groups—yielding h/e- or $h/(2e)$-oscillations, respectively—according to which arm is traversed by the quasiparticles, impurity scattering and the resulting deflection of quasiparticles has no adverse effect as long as scattering *between* the groups is weak, while scattering *within* one group may be arbitrarily strong. In addition, note that while our description of transport via the scattering matrix assumes complete phase coherence, a signature that distinguishes retro from specular Andreev reflection is assumed to persist also in the case of a finite phase coherence length. More specifically, if the phase coherence length is on the order of the ring circumference, first order amplitudes in Eqs. (4.5) and (4.6) may be neglected. Then, retro reflection would still manifest itself in $h/(2e)$-oscillations, while there would be no oscillations at all in the case of specular reflection.

Finally, we add a remark concerning the choice of armchair boundary conditions in the leads employed in the analysis in this section. In a tight binding implementation of graphene, there are two simple choices for the orientation of the leads. Often, zigzag edges are considered
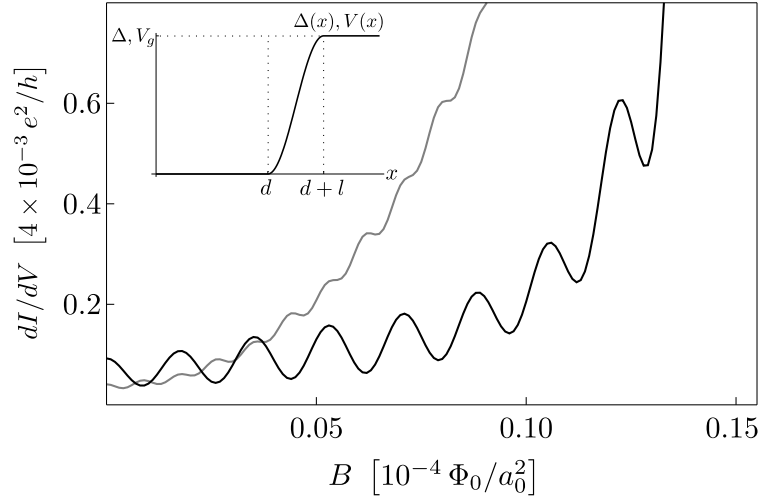
Figure 4.15: Magnetoconductance of the system used in Fig. 4.12 with a smooth potential profile (inset) with $l = 90a_0$ and bulk disorder of strength $\sigma = 0.01t$ as explained in the text. The h/e vs. $h/(2e)$ signature still persists. The color coding is the same as in Fig. 4.12 (Figure adapted from Refs. [Sch12b, Sch12a]).

to represent a generic boundary condition for graphene ribbons [Akh08b]. In this case, edge states are present in the system, which modify the simple picture provided in Fig. 4.11 by adding additional scattering channels between bulk and edge states while removing certain scattering channels between bulk states due to the conservation of the so-called pseudoparity symmetry that acts like a selection rule [Rai09]. In the realistic limit of metal leads providing a large number of propagating bulk modes, this effect should be less important. However, for the system geometry used in the numerical calculations in combination with the low energy scales, it may significantly affect the observed behavior. In order to avoid this influence, we chose armchair boundary conditions in the leads, which do not provide any edge states. Note in addition that in realistic systems the zigzag-specific effect would also be suppressed since the zigzag edge state is not protected against disorder when next-nearest neighbor hopping is taken into account [Wim09a]. Therefore, we are convinced that our results based on armchair edges in the reservoirs describe the generic situation for wide leads.

4.4 Summary and outlook

Considering the development of the topic of the Aharonov–Bohm effect in graphene, we can assess that there is a great variety of aspects covered by theoretical considerations, and despite the significant amount of work done on graphene ring systems, there are still a number of open questions drawn from initial experiments that remain unanswered so far as well as a large number of theoretical predictions not yet confirmed by corresponding experiments. On the one hand, it would be interesting from a theoretical point of view to investigate the origin and significance of the seemingly linear relationship between conductance and oscillation amplitude as well as the significant increase of the oscillation amplitude at high

magnetic field observed in Ref. [Rus08]. Further analysis on the role of interactions may also be worthwhile. On the other hand, while some of the theoretical models are hardly realizable in experiments at the present stage, i.a., due to insufficient control over edge properties, there are systems that should be experimentally accessible and robust and should therefore allow for the observation of graphene-specific features in the Aharonov–Bohm effect. Two of such systems have been introduced in the previous two sections. In Section 4.2, it was shown that Klein tunneling through a *npn*-junction in graphene manifests itself in the Aharonov–Bohm oscillations in a graphene ring structure where one of the ring arms is gated to form the junction together with the two adjacent leads; more specifically, it was found that for smooth *npn*-junctions, tunneling through this arm and thus the electron interference and magnetooscillations in the ring structure are increasingly suppressed in accordance with the fundamental properties of Klein tunneling in graphene as described in Refs. [Bee08a, Che06]. In Section 4.3, Andreev reflection at the interface between a graphene ring structure and a superconducting lead in the subgap regime has been considered. Depending on the ratio of Fermi energy and excitation energy (or bias voltage), the holes created at the interface are either retro reflected or reflected specularly, with respect to the direction of the incident electron. The corresponding trajectories of the charge carriers through the ring give rise to different dominant frequencies of the observed magnetooscillations from which the type of Andreev reflection can be inferred. This signature is topologically robust in the sense that scattering has no adverse effect as long as the trajectories still traverse the same arm of the ring.

Chapter 5

Resonant scattering in graphene

In this chapter, we investigate the effects of disorder on the transport properties of graphene. In particular, we concentrate on strong short-range on-site potentials induced, e.g., by strongly bound adatoms or, equivalently, vacancies in the graphene lattice. Such defects are known to support localized electronic states close to the Dirac point [Eli09, Ost06, Sta07, Per08, Rob08, Ni10, Kat10a, Tit10, Ost10, Weh10, Yua10] and therefore act as resonant scatterers for the Dirac fermions, which can be expected to alter the transport properties of the low-energy excitations in graphene. Due to the sublattice degree of freedom in the graphene lattice, the transport may not only depend on the total impurity concentration but may also be affected by an imbalance of the distribution of defects over the two sublattices. Indeed, such a dependence was found in Ref. [Ost10], where the authors study the quantum critical regime at high impurity concentration, where the conductivity saturates at a value that depends on the imbalance of the vacancy distribution among the two sublattices.

In Section 5.2, we will uncover an even more subtle sensitivity of the conductance of a graphene sample in the presence of impurities, not only to the sublattice degree of freedom but also to the specific type of defect site within a given sublattice. This particular type of site is determined by the phase of the corresponding T-matrix, which may assume one out of three possible values, giving rise to a superlattice structure with six inequivalent sites per supercell and thus an extended classification of atomic sites within the graphene lattice beyond the conventional sublattice structure.

The short-range character of the disorder type under consideration allows for an exact analytical treatment of the full counting statistics in a N-dimensional vector space called "unfolded (impurity) space" [Ost10], where N is the number of individual impurities. This unfolded scattering theory, which is based on Nazarov's generating function technique in a matrix Green's function formalism [Naz94, Tit10, Sch10b, Ost10, Ryu07], is presented in Section 5.1 for a completely general Hamiltonian corresponding to the geometry shown in Fig. 5.1 in the presence of point-like defects of arbitrary impurity profile.[1] In Section 5.2, we apply this theory to the particular case of vacancy states in the low-energy effective model of graphene and compare the results with numerical simulations performed on the tight binding model concentrating on the simplest case of only two vacancies present in the system. In Section 5.3, we provide an outlook on potential future developments of the topic including the dependence of the conductivity on the distribution of defects over the six inequivalent sites at finite impurity concentration.

---

[1] The expression "point-like" will be specified in more detail in the following section.
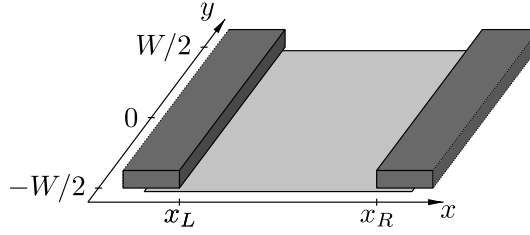
Figure 5.1: Two-terminal transport setup under consideration; a rectangular sample with length L and width W is connected to two contacts at $x = x_L$ and $x = x_R$, respectively, where x denotes the transport direction (Figure adapted from Ref. [Sch10b]).

5.1 Unfolded scattering theory

In order to formulate the transport theory in the N-dimensional unfolded vector space formed by N individual impurities, we utilize the generating function technique within the matrix Green's function formalism as pioneered by Nazarov [Naz94, Tit10, Sch10b, Ost10, Ryu07]. To this end, we partly follow Ref. [Sch10b] and consider a system with a left lead and a right lead as shown in Fig. 5.1, whose transport characteristics can be described by a unitary scattering matrix

$$S = \begin{pmatrix} r & t' \\ t & r' \end{pmatrix}.$$

Without loss of generality, we will consider transport described by the transmission matrix t in the following. The full counting statistics[2] are conveniently expressed in terms of a (cumulant) generating function $\mathcal{F}$ [Sch10b, Tit10, Ost10, Lev93], which we define as

$$\mathcal{F}(z) \equiv \sum_{k=1}^{\infty} z^{k-1} \operatorname{tr}\left(t^{\dagger}t\right)^k = \operatorname{tr}\left(\left(t^{\dagger}t\right)^{-1} - z\right)^{-1} = \sum_{m=1}^{M} \frac{T_m}{1 - zT_m}, \qquad 0 \le z < 1,$$

where we used the expansion of the geometric series and the so-called "counting field" $z \ge 0$ is chosen sufficiently small for this series to converge, i.e., $|zT_m| < 1$ for all $m = 1, \ldots, M$, where $T_1, \ldots, T_M$ denote the M transmission eigenvalues, i.e., the eigenvalues of the matrix $t^{\dagger}t$. With this definition, the moments of the transmission distribution are generated from the derivatives of $\mathcal{F}(z)$ with respect to z evaluated at $z = 0$:[3]

$$\mathcal{F}^{(k)}(0) = k! \operatorname{tr}\left(t^{\dagger}t\right)^{k+1}, \qquad k \in \mathbb{N}_0.$$

Since a perturbation theory is best formulated in the language of Green's functions, a transition from the scattering description to the Green's function formalism is convenient.

---

[2] The full counting statistics are given by the moments $\operatorname{tr}(t^{\dagger}t)^n$, $n \in \mathbb{N}$, of the transmission distribution, yielding conductance, noise, and higher order cumulants, and contain the same information as the transmission distribution itself, i.e., the probability distribution of the transmission eigenvalues (the eigenvalues of the matrix $t^{\dagger}t$) [Sch10b].

[3] We use the common short-hand notation for derivatives, $(\mathrm{d}/\mathrm{d}x)^n f(x)|_{x=x_0} \equiv f^{(n)}(x_0)$ with $f'(x) \equiv f^{(1)}(x)$, and in addition define $f^{(n)}(0) \equiv \lim_{x_0 \to 0^+} f^{(n)}(x_0)$ for functions $f(x)$ where x is restricted according to $x \ge 0$.

In order to obtain an elegant formulation of this perturbation theory, we introduce two quantities and relate them to the moments of the transmission distribution.

We first define a Green's function $\check{G}$ via the Dyson equation,

$$\check{G} \equiv \check{G}_0 + \check{G}_0 \check{\mathcal{V}} \check{G} \equiv \sum_{n=0}^{\infty} \check{G}^{(n)}$$

in the compact notation introduced in Chapter 1, where integration over internal degrees of freedom is implicitly assumed, and n denotes orders in $\check{\mathcal{V}}$. $\check{G}_0$ contains uncoupled retarded and advanced Green's functions and $\check{\mathcal{V}}$ describes their coupling at the lead–sample interfaces:

$$\check{G}_0 \equiv \begin{pmatrix} \hat{G}^r & 0 \\ 0 & \hat{G}^a \end{pmatrix}, \qquad \check{\mathcal{V}} \equiv \sqrt{z} \begin{pmatrix} 0 & \hat{\Gamma}_L \\ \hat{\Gamma}_R & 0 \end{pmatrix},$$

where $\hat{G}^{r,a} \equiv \left(E - \hat{H} \pm \mathrm{i}0^+ \right)^{-1}$ denote the usual retarded and advanced Green's functions corresponding to the Hamiltonian $\hat{H}$ parametrized by the energy E. The coupling $\check{\mathcal{V}}$ is localized according to

$$\hat{\Gamma}_{L,R}(\mathbf{r}, \mathbf{r}') \equiv \delta(x - x_{L,R}) \hat{\Gamma}(\mathbf{r}, \mathbf{r}').$$

$\hat{\Gamma}$ is defined according to Section 2.2 and, as described there (see Eq. (2.12)), essentially represents the velocity operator in the leads (times $\hbar$). More specifically, we express this operator through the Heisenberg equation of motion as

$$\hat{\Gamma} \equiv \hbar \hat{v}_x \equiv \hbar \frac{\mathrm{d}}{\mathrm{d}t} \hat{x} = \mathrm{i}[\hat{H}, \hat{x}] \tag{5.1}$$

for the system shown in Fig. 5.1. $\check{G}$ is a matrix Green's function in the so-called retarded–advanced (RA) space [Sch10b, Tit10, Ost10],

$$\check{G} \equiv \begin{pmatrix} \hat{G}_{11} & \hat{G}_{12} \\ \hat{G}_{21} & \hat{G}_{22} \end{pmatrix} \equiv \sum_{n=0}^{\infty} \begin{pmatrix} \hat{G}_{11}^{(n)} & \hat{G}_{12}^{(n)} \\ \hat{G}_{21}^{(n)} & \hat{G}_{22}^{(n)} \end{pmatrix},$$

and was first introduced by Nazarov [Naz94, Naz95]. Solving the Dyson equation for the inverse, $\check{G}^{-1}$, we obtain

$$\check{G}^{-1} = \check{G}_0^{-1} - \check{\mathcal{V}} = \begin{pmatrix} E - \hat{H} + \mathrm{i}0^+ & -\sqrt{z}\hat{\Gamma}_L \\ -\sqrt{z}\hat{\Gamma}_R & E - \hat{H} - \mathrm{i}0^+ \end{pmatrix}. \tag{5.2}$$

We further define the quantity[4]

$$\tilde{\Omega}(z) \equiv -\operatorname{tr} \ln \check{G} = \operatorname{tr} \ln \check{G}^{-1}$$

and show that it is related to the generating function. First, the derivative of $\tilde{\Omega}$ with respect

---

[4] Sometimes the identity $\operatorname{tr} \ln A = \ln \det A$ for any square, non-singular matrix A [Wit10] is encountered or used in the literature and we will also make use of it in the following.

to the counting field z gives

$$\tilde{\Omega}'(z) = \mathrm{tr}\left(\breve{G}\frac{\mathrm{d}}{\mathrm{d}z}\breve{G}^{-1}\right) = -\frac{1}{2\sqrt{z}}\Big(\mathrm{tr}\,(\hat{G}_{12}\hat{\Gamma}_R) + \mathrm{tr}\,(\hat{G}_{21}\hat{\Gamma}_L)\Big).$$

Noting that $\hat{G}_{12}^{(2n)} = \hat{G}_{21}^{(2n)} = 0$ for $n \in \mathbb{N}_0$, we can then rewrite

$$
\begin{aligned}
-\tilde{\Omega}'(z) &= \frac{1}{2\sqrt{z}}\sum_{n=1}^{\infty}\Big(\mathrm{tr}\,(\hat{G}_{12}^{(2n-1)}\hat{\Gamma}_R) + \mathrm{tr}\,(\hat{G}_{21}^{(2n-1)}\hat{\Gamma}_L)\Big) \\
&= \frac{1}{2}\sum_{n=1}^{\infty}\Big(\mathrm{tr}\,(\hat{G}^r\hat{\Gamma}_L\hat{G}^a\hat{\Gamma}_R)^n z^{n-1} + \mathrm{tr}\,(\hat{G}^a\hat{\Gamma}_R\hat{G}^r\hat{\Gamma}_L)^n z^{n-1}\Big) \\
&= \sum_{n=1}^{\infty} z^{n-1}\,\mathrm{tr}\,(\hat{\Gamma}_R\hat{G}^r\hat{\Gamma}_L\hat{G}^a)^n = \mathcal{F}(z),
\end{aligned}
$$

where the last step is obtained in complete analogy to Section 2.2 noting that the trace is invariant under a change of the basis by means of a unitary transformation.[5]

To conveniently express transport observables, i.e., moments of the transmission distribution, in terms of this quantity, we introduce a parametrization in terms of a so-called "counting angle":

$$z \equiv -\sinh^2(\phi/2), \qquad \Omega(\phi) \equiv \tilde{\Omega}(-\sinh^2(\phi/2)), \qquad 0 \le \mathrm{i}\phi < \pi.$$

In this parametrization, the relation to the generating function reads

$$\mathcal{F}(z)\big|_{z=-\sinh^2(\phi/2)} = -\left(-\frac{\mathrm{d}}{\mathrm{d}\phi}\sinh^2(\phi/2)\right)^{-1}\Omega'(\phi) = \frac{2}{\sinh\phi}\Omega'(\phi), \tag{5.3}$$

or equivalently

$$\int \mathcal{F}(z)\,\mathrm{d}z\big|_{z=-\sinh^2(\phi/2)} = -\mathrm{tr}\ln\left(\mathbf{1} + \sinh^2(\phi/2)t^\dagger t\right) + \mathrm{const.} = -\Omega(\phi). \tag{5.4}$$

We can immediately infer $\Omega'(0) = 0$, while for the second derivative, we obtain—either by direct calculation from Eq. (5.4) or by applying l'Hôpital's rule to Eq. (5.3)—the linear conductance:

$$G = \frac{e^2}{h}\,\mathrm{tr}\,(t^\dagger t) = \frac{e^2}{h}\mathcal{F}(0) = \frac{2e^2}{h}\Omega^{(2)}(0). \tag{5.5}$$

The two properties $\Omega'(0) = 0$ and $\Omega^{(2)}(0) \ge 0$ motivate the term "(fictitious) free energy" that is commonly used for Ω [Sch10b] since this quantity is minimized under the influence of a fictitious potential [Naz94, Naz95], expressed in terms of the counting field, for the physical situation where this field vanishes.

One word of warning: The factor 2 in Eq. (5.5) originates from the last expression in Eq. (5.3) and therefore does not account for any kind of (spin) degeneracy whatsoever. Any

---

[5] Note that the theory outlined in the present section is formulated in a completely general abstract notation, whereas in Section 2.2, a particular basis involving the (transverse) position representation has been chosen.

such degeneracies still have to be taken into account either explicitly in the matrix structure of the transmission matrix t—as is implicitly assumed here—or by introducing additional factors by hand into the expression for the conductance. These prefactors must not be confused.

Higher moments of the transmission distribution are most easily obtained by repeatedly applying l'Hôpital's rule; e.g., for the second moment, we obtain using Eq. (5.3):

$$
\begin{aligned}
\operatorname{tr}\left(t^\dagger t\right)^2 = \frac{\mathrm{d}}{\mathrm{d}z}\mathcal{F}(z)\Big|_{z=0} &= \left(-\frac{\mathrm{d}}{\mathrm{d}\phi}\sinh^2(\phi/2)\right)^{-1}\frac{\mathrm{d}}{\mathrm{d}\phi}\frac{2}{\sinh\phi}\Omega'(\phi)\Big|_{\phi=0} \\
&= -4\frac{\Omega^{(2)}(\phi)\sinh\phi - \Omega'(\phi)\cosh\phi}{\sinh^3\phi}\bigg|_{\phi=0} \\
&\to -4\frac{\Omega^{(3)}(\phi) - \Omega'(\phi)}{3\sinh\phi\cosh\phi}\bigg|_{\phi=0} \to -4\frac{\Omega^{(4)}(\phi) - \Omega^{(2)}(\phi)}{3\cosh(2\phi)}\bigg|_{\phi=0} \\
&= \frac{4}{3}\left(\Omega^{(2)}(0) - \Omega^{(4)}(0)\right),
\end{aligned}
$$

where the application of l'Hôpital's rule is indicated by arrows.

Perturbation theory

In the following, we follow in parts Ref. [Ost10] and consider the contribution to the free energy Ω due to a disorder potential

$$
V \equiv \sum_{n=1}^{N} V_n,
$$

which is composed of N individual impurity potentials V_n. As usual, the perturbation is accounted for by means of a Dyson equation, which can be written as

$$
\mathcal{G}^{-1} \equiv \mathcal{G}_0^{-1} - V, \qquad \mathcal{G}_0 \equiv \check{G}. \tag{5.6}
$$

The change in the free energy due to the presence of the disorder potential is then given as[6]

$$
\delta\Omega \equiv \operatorname{tr}\ln\mathcal{G}^{-1} - \operatorname{tr}\ln\mathcal{G}_0^{-1} = \operatorname{tr}\ln\left(\mathcal{G}_0\mathcal{G}^{-1}\right) = \operatorname{tr}\ln(1 - \mathcal{G}_0 V). \tag{5.7}
$$

Using Sylvester's determinant theorem [She12], which is a special case of the matrix determinant lemma [Bro12] and states that $\det(\mathbf{1} + AB) = \det(\mathbf{1} + BA)$ for any $n \times m$ matrix A

---

[6] Note that in general, the relation $\ln(AB) = \ln A + \ln B$ for two matrices A and B only holds if A and B commute; however, even for non-commuting matrices, we have $\operatorname{tr}\ln(AB) = \ln\det(AB) = \ln(\det A\det B) = \ln\det A + \ln\det B = \operatorname{tr}\ln A + \operatorname{tr}\ln B$. We thank Pavel Ostrovsky for pointing this identity out to us.

and any $m \times n$ matrix B, we can rewrite this expression in the following way:

$$\delta\Omega = \mathrm{tr}\ln(\mathbf{1} - \mathcal{G}_0 V) = \ln\det(\mathbf{1} - \mathcal{G}_0 V) = \ln\det\left(\mathbf{1} - (\mathcal{G}_0, \ldots, \mathcal{G}_0)\begin{pmatrix} V_1 \\ \vdots \\ V_N \end{pmatrix}\right)$$

$$= \ln\det\left(\mathbf{1} - \begin{pmatrix} V_1 \\ \vdots \\ V_N \end{pmatrix}(\mathcal{G}_0, \ldots, \mathcal{G}_0)\right) = \ln\det(\mathbf{1} - \hat{V}\hat{\mathcal{G}}_0) = \mathrm{tr}\ln(\mathbf{1} - \hat{V}\hat{\mathcal{G}}_0), \qquad (5.8)$$

where "^" indicates $N \times N$ block matrices in the unfolded vector space of N individual impurities, whose elements we label with indices $n, m \in \{1, \ldots, N\}$ in the following; in particular, the elements of $\hat{V}$ and $\hat{\mathcal{G}}_0$ are defined by $(\hat{V})_{nm} \equiv V_n\delta_{nm}$ and $(\hat{\mathcal{G}}_0)_{nm} \equiv \mathcal{G}_0$, respectively. Eq. (5.8) can then be manipulated further:

$$\delta\Omega = \mathrm{tr}\ln\left(\left(\mathbf{1} - \hat{V}\hat{g}\right)\left(\mathbf{1} - (\mathbf{1} - \hat{V}\hat{g})^{-1}\hat{V}(\hat{\mathcal{G}}_0 - \hat{g})\right)\right)$$

$$= \underbrace{\mathrm{tr}\ln(\mathbf{1} - \hat{V}\hat{g})}_{\text{const.}} + \mathrm{tr}\ln\left(\mathbf{1} - \hat{T}(\hat{\mathcal{G}}_0 - \hat{g})\right), \qquad (5.9)$$

where the elements of $\hat{g}$ and $\hat{T}$ are defined by $(\hat{g})_{nm} \equiv g\delta_{nm}$ and $(\hat{T})_{nm} \equiv T_n\delta_{nm}$, respectively, where g is the free Green's function, i.e., the Green's function corresponding to the disorder-free system in the absence of the leads, and

$$T_n \equiv (\mathbf{1} - V_n g)^{-1}V_n = V_n + V_n g V_n + \ldots, \qquad n = 1, \ldots, N, \qquad (5.10)$$

are the T-matrix operators for the individual impurities. The first expression in Eq. (5.9) is constant in the sense that it does not depend on ϕ and therefore does not contribute to any transport observable. Using the series expansion of the logarithm, we obtain

$$\delta\Omega = \text{const.} - \sum_{k=1}^{\infty} \sum_{n_1, \ldots, n_k=1}^{N} \frac{1}{k}\mathrm{tr}\left(T_{n_1}(\mathcal{G}_0 - g\delta_{n_1 n_2})\ldots T_{n_k}(\mathcal{G}_0 - g\delta_{n_k n_1})\right).$$

Note that the trace still implies integrations over all internal position degrees of freedom. A key simplification now occurs for "point-like" impurities, i.e., if the individual impurity potentials are sufficiently localized in position space such that we may approximate the Green's functions to be constant within the domain of integration in the following way:

$$\mathcal{G}_0(\mathbf{r} \in \partial\mathbf{r}_n, \mathbf{r}' \in \partial\mathbf{r}_m) \approx \mathcal{G}_0(\mathbf{r}_n, \mathbf{r}_m), \qquad n \neq m,$$

$$(\mathcal{G}_0 - g)(\mathbf{r} \in \partial\mathbf{r}_n, \mathbf{r}' \in \partial\mathbf{r}_n) \approx (\mathcal{G}_0 - g)(\mathbf{r}_n, \mathbf{r}_n) \equiv \lim_{\mathbf{r} \to \mathbf{r}_n} (\mathcal{G}_0(\mathbf{r}_n, \mathbf{r}) - g(\mathbf{r}_n, \mathbf{r})), \qquad (5.11)$$

where $\mathbf{r}_n = (x_n, y_n)^\intercal$ denotes the position where V_n is centered, $\partial\mathbf{r}_n$ denotes the relevant domain of non-vanishing impurity potential around $\mathbf{r}_n$ that contributes to the integrals over position, and the impurity potentials are assumed to be non-overlapping in the sense that $\partial\mathbf{r}_n \cap \partial\mathbf{r}_m = \emptyset$ for $n \neq m$. Then, each integral over position only involves an individual T-matrix and the correction to the free energy in the presence of such point-like impurities

can be written as

$$\delta\Omega = \text{const.} + \text{tr} \ln \left(1 - \hat{\mathcal{T}}\hat{\mathcal{G}}_{\text{reg}}\right) \tag{5.12}$$

with the regularized Green's function matrix $\hat{\mathcal{G}}_{\text{reg}}$ with elements

$$(\hat{\mathcal{G}}_{\text{reg}})_{nm} \equiv \begin{cases} \mathcal{G}_0(\mathbf{r}_n, \mathbf{r}_m) & \text{if } n \neq m, \\ (\mathcal{G}_0 - g)(\mathbf{r}_n, \mathbf{r}_n) & \text{if } n = m, \end{cases} \tag{5.13}$$

and $(\hat{\mathcal{T}})_{nm} \equiv \mathcal{T}_n \delta_{nm}$, where

$$\mathcal{T}_n \equiv \int V_n(\mathbf{r}) \, d\mathbf{r} + \int \int V_n(\mathbf{r}) g(\mathbf{r}, \mathbf{r}') V_n(\mathbf{r}') \, d\mathbf{r} \, d\mathbf{r}' + \ldots, \qquad n = 1, \ldots, N, \tag{5.14}$$

are the integrated impurity T-matrices for the individual impurity potentials. The point-like character of the impurity potentials thus allows for a reduction of a microscopic calculation involving integrals over internal continuous position degrees of freedom, Eq. (5.7), to a simple $N \times N$ finite-size matrix algebra in the unfolded space, Eq. (5.12).

With Eq. (5.12), we have established a simple analytical expression from which the corrections to transport properties in the presence of point-like impurities can be obtained for a system geometry as shown in Fig. 5.1. The ingredients to this expression are:

- the free Green's function $g(\mathbf{r}, \mathbf{r}'; E) = g(\mathbf{r} - \mathbf{r}'; E)$ of the clean, homogeneous system, i.e., in the absence of impurities and in the absence of the leads,

- the unperturbed Green's function $\mathcal{G}_0$ for the impurity-free transport geometry shown in Fig. 5.1, i.e., in the absence of impurities but in the presence of the leads, and

- the integrated impurity T-matrix for each individual impurity, which is obtained from the impurity potential profile and the free Green's function according to Eq. (5.14).

Note that the assumption of point-like impurities does not restrict the type of disorder for which the theory remains valid to (atomically sharp) short-range scatterers but merely requires non-overlapping impurity potential profiles. Smooth long-range impurities, which do not lead to intervalley scattering, may as well be considered [Ost10, Tit10, Sch10b]; these are characterized by a T-matrix which is diagonal in valley space.

In the next section, we will apply the unfolded scattering formalism to graphene for the simple case of two individual impurities, and we will investigate the influence of their distribution over the particular sites of the honeycomb lattice. In the course of doing so, we will find that the graphene lattice exhibits a more subtle structure than the usual sublattice degree of freedom. Finally, in Section 5.3, we will provide an outlook on the transport properties in the case of finite impurity densities, when impurities are distributed in a specific way over the substructure revealed in Section 5.2.

5.2 Color-dependent conductance of graphene with adatoms

Controllable deposition of adatoms known as chemical functionalization is an efficient way to alter the electronic properties of graphene. Adatoms can change the orbital state of

the functionalized carbon atoms from sp^2 to sp^3 configuration removing electrons from the conduction band and transforming graphene into a semiconductor [Liu08, Eli09]. For instance, fully hydrogenated graphene, also called "graphane", is predicted to have a wide band gap of 3–14 eV [Leb09] in sharp contrast to clean graphene which has a gapless excitation spectrum [Nov04].

A small concentration of strongly bound adatoms or molecules, such as hydrogen or CH_3, is naturally present even in the cleanest graphene samples produced by exfoliation. The effect of vacancies, which can be thought of as infinitely strong on-site potential impurities, is essentially analogous to that of adatoms. Such impurities support electronic states at the Dirac point, leading to resonant scattering of Dirac quasiparticles [Eli09, Ost06, Sta07, Per08, Rob08, Ni10, Kat10a, Tit10, Ost10, Weh10, Yua10, Weh09].

From a theoretical point of view, the strong on-site impurities or vacancies preserve both time-reversal and chiral symmetries of the graphene Hamiltonian. The interplay of the symmetries prevents quantum localization at the Dirac point [Ost06] and gives rise to a quantum critical regime of charge transport at a sufficiently high impurity concentration. The conductivity of graphene in this regime is predicted to take on a constant value that depends on the distribution of adatoms among different sublattices of the graphene crystal [Ost10]. In this section, we describe an even more subtle sensitivity of transport quantities, not only to the sublattice but also to the type of impurity sites therein, that can be clearly seen even in the presence of only two scatterers.

The theory of quantum transport in disordered graphene is highly non-trivial in the vicinity of the Dirac point due to the breakdown of the quasiclassical approximation. An essentially exact and efficient approach, namely the unfolded scattering formalism, has been presented in the previous section. In addition, we perform here a detailed comparison of this formalism with numerical simulations based on the recursive Green's function technique within the Landauer–Büttiker formalism with no adjustable parameters. In particular, we calculate both numerically and analytically the conductance of graphene at the Dirac point in the presence of two vacancies. This quantity is shown to have a remarkable sensitivity to the "color" of the vacated sites, which is determined by the phase of the Bloch wavefunction and by the orientation of the crystal with respect to the transport direction and can take on one out of six possible values for a fixed orientation angle. We further use the analytic results in order to construct the first terms of the color-dependent virial expansion of the conductivity with respect to vacancy concentration and find that the conductivity is particularly sensitive to the crystal orientation if adatom sites have a preferred color.[7]

Model

An essential ingredient to the unfolded scattering formalism presented in the previous section is the single-impurity T-matrix, which is known for a variety of impurity types in graphene [Hen07, Nov07, Bas08] and carbon nanotubes [McC04]. Starting from the standard tight binding model on the honeycomb lattice, one can relate the on-site potential to the corresponding T-matrix and the free Green's function via Eq. (5.10); in the long-wavelength limit, at distances $|\mathbf{r}| \gg a_0$, where $\mathbf{r}$ is a vector connecting two lattice sites, the free

---

[7] The work presented in this section has also been published in Ref. [Sch11].

Green's function between sites of the same sublattice (i.e., if $\mathbf{r}$ is a lattice vector) behaves as $g \propto E H_0^{(1)}(|E\mathbf{r}|/(\hbar v_F))$ as a function of energy E and position $\mathbf{r}$, whereas it behaves as $g \propto E H_1^{(1)}(|E\mathbf{r}|/(\hbar v_F))$ between sites of different sublattices—apart from spatial variations on the lattice scale due to interference between the two valleys [Ben09a]; here, $H_{0,1}^{(1)}$ denote Hankel functions of the first kind. In particular, while the free Green's function remains finite between sites of different sublattices in the limit $E \to 0$, it vanishes as $E \ln E$ between sites of the same sublattice [Ost06]—a behavior that also holds on the atomic scale, i.e., for $|\mathbf{r}| \sim a_0$ [Bas08].

In graphene, the key simplification thus occurs in the limit $E \to 0$, i.e., at the Dirac point, since then the lowest order contribution of the series expansion (5.10) is already exact if the impurity potential vanishes on one sublattice. More specifically, for an impurity potential that is localized on a particular atomic site i_0 of the graphene lattice,

$$\langle i|V|j\rangle \equiv V_{ij} = V_0 \delta_{ij} \delta_{ii_0},$$

such as the vacancies considered in this section, the expression for the T-matrix takes on a particularly simple form in the limit $E \to 0$:

$$\begin{aligned}
\langle i|T|j\rangle &\equiv T_{ij} \\
&= V_{ij} + \sum_{k_1,k_2} V_{ik_1} g_{k_1 k_2} V_{k_2 j} + \sum_{k_1,\dots,k_4} V_{ik_1} g_{k_1 k_2} V_{k_2 k_3} g_{k_3 k_4} V_{k_4 j} + \dots = V_{ij},
\end{aligned}$$

where $g_{ij} \equiv \langle i|g|j\rangle$ is the free particle Green's function taken between the lattice sites i and j. Expressing this T-matrix in the valley–sublattice space of the Dirac Hamiltonian reveals a color scheme for the graphene lattice as described in the following.

The tight binding and effective mass models of ideal graphene have been introduced in Section 3.1 and here we follow the conventions chosen there. Again, the graphene lattice is oriented at an angle α as shown in Fig. 5.2, and we regard x as the transport direction. The tight binding wavefunction $\Psi(\mathbf{r})$ (see Eqs. (3.1) and (3.3)) and the four-component spinor of the effective mass model $|\Phi\rangle$ (see Eqs. (3.5) and (3.6)) are connected via $\Psi(\mathbf{r}) = \langle u(\mathbf{r})|\Phi\rangle$, where[8]

$$\langle u(\mathbf{r})| \equiv \sqrt{A} \begin{cases} (\mathrm{e}^{\mathrm{i}(\alpha+2\mathbf{Kr})/2}, 0, 0, \mathrm{e}^{-\mathrm{i}(\alpha-2\mathbf{Kr})/2}), & \zeta_{\mathbf{r}} = +, \\ (0, \mathrm{i}\mathrm{e}^{-\mathrm{i}(\alpha-2\mathbf{Kr})/2}, \mathrm{i}\mathrm{e}^{\mathrm{i}(\alpha-2\mathbf{Kr})/2}, 0), & \zeta_{\mathbf{r}} = -. \end{cases} \tag{5.15}$$

The projector $|u(\mathbf{r})\rangle\langle u(\mathbf{r})|$ thus describes a transition between the effective mass and tight binding models. Consequently, the representation in the effective mass model of the T-matrix of an on-site potential impurity of strength V_0 located at a position $\mathbf{r}$ ought to be written as

$$T = V_0 |u(\mathbf{r})\rangle\langle u(\mathbf{r})|. \tag{5.16}$$

The phase factors in Eq. (5.15) are responsible for a site classification that depends on the

---

[8] Note that H_0 (see Eq. (3.6)) and the derivatives ∂_x and ∂_y contained therein act on $|\Phi\rangle$ (see Eq. (3.5)) and the envelope wave functions $\phi_\pm$ and $\phi'_\pm$ contained therein, which depend on a continuous position variable that is suppressed in Eq. (3.5). They do not act on expressions such as Eq. (5.15), which contain a discrete position variable that can only take on values corresponding to the sites of the honeycomb lattice.
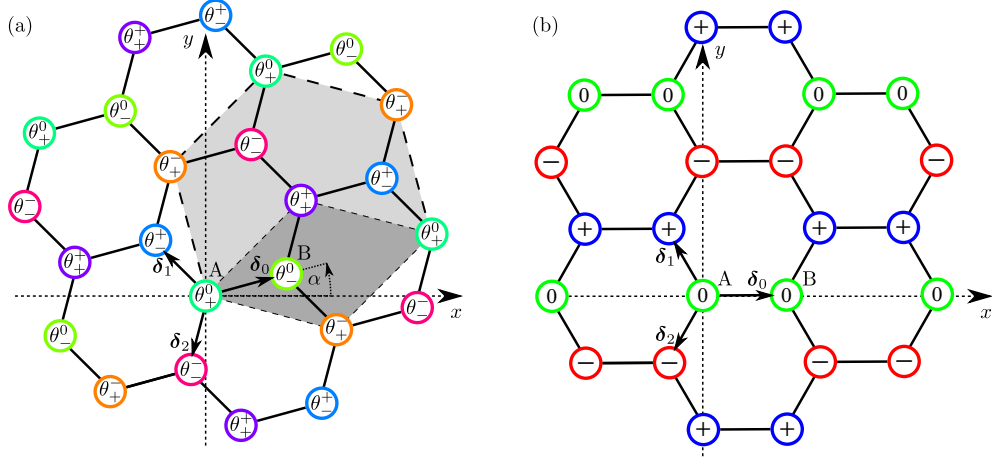
Figure 5.2: Color schemes for vacancies or resonant adatoms: (a) General color scheme: The impurity site is characterized by the phase $\theta_\pm^c \equiv \pm\alpha + 2\pi c/3$, where "$\pm$" refers to the sublattice (A $\widehat{=}$ + and B $\widehat{=}$ −) and $c \in \{-, 0, +\}$ denotes the colors (red, green, and blue, respectively). The color scheme depends on the transport direction x or, equivalently, on the orientation angle α and introduces a superlattice structure with six sites per supercell (light gray Wigner–Seitz cell) on top of the hexagonal lattice with two sites per unit cell (dark gray). The phases at A and B sites connected by the vector $\boldsymbol{\delta}_0$ differ most for $\alpha = \pi/6$. (b) Degenerate color scheme: The phases at A and B sites connected by the vector $\boldsymbol{\delta}_0$ are equal for $\alpha = 0$ (Figure adapted from Ref. [Sch11]).

orientation angle α. Using Eqs. (5.15) and (5.16), we represent the impurity T-matrix as

$$
T_+ = AV_0 \begin{pmatrix} 1 & 0 & 0 & e^{-i(\alpha+2\mathbf{Kr})} \\ 0 & 0 & 0 & 0 \\ 0 & 0 & 0 & 0 \\ e^{i(\alpha+2\mathbf{Kr})} & 0 & 0 & 1 \end{pmatrix}, \quad
T_- = AV_0 \begin{pmatrix} 0 & 0 & 0 & 0 \\ 0 & 1 & e^{i(\alpha-2\mathbf{Kr})} & 0 \\ 0 & e^{-i(\alpha-2\mathbf{Kr})} & 1 & 0 \\ 0 & 0 & 0 & 0 \end{pmatrix},
$$

for impurities located on sublattice A and B, respectively. In a more compact notation, we can rewrite

$$
T_\pm = 2\pi\hbar v\ell \frac{1 \pm \sigma_z\tau_z + \sigma_\mp\tau_- e^{i\theta_\pm} + \sigma_\pm\tau_+ e^{-i\theta_\pm}}{4}, \qquad \ell \equiv \frac{AV_0}{\pi\hbar v_F}, \tag{5.17}
$$

in accordance with previous derivations of this T-matrix [Ost06, Bas08, McC04, Sho98]; here, ℓ is called "scattering length" [Bas08], $\sigma_\pm \equiv (\sigma_x \pm i\sigma_y)/\sqrt{2}$, $\tau_\pm \equiv (\tau_x \pm i\tau_y)/\sqrt{2}$, and $\sigma_{x,y,z}$ and $\tau_{x,y,z}$ are the Pauli matrices in the sublattice and valley space, respectively. The phases $\theta_\pm$ in Eq. (5.17) are defined as $\theta_\pm \equiv \pm\alpha + 2\mathbf{Kr}$. Since $\mathbf{Kr}$ is an integer multiple of $2\pi/3$ for any lattice site, we encounter three possible values of the factor $e^{2i\mathbf{Kr}} = e^{-i\mathbf{Kr}} = e^{2\pi ic/3}$ with $c = 0, \pm 1$, assuming an A site at $\mathbf{r} = 0$ as in Fig. 5.2. Together with the sublattice index ζ, this yields six possible T-matrices for on-site impurities. In order to visualize this classification, in Fig. 5.2 we introduce a color scheme by assigning one out of six possible colors to each lattice site (three colors in each sublattice) corresponding to the phase factors $e^{i\theta_\pm^c} \equiv e^{\pm i\alpha + 2\pi ic/3}$. These colors define a superlattice with a period of three elementary unit

cells and with six atoms per supercell. For $\alpha = 0$, only three distinct phases remain yielding the same three colors in both sublattices.

Having established the particular form of the impurity T-matrix, we can calculate the correction to the conductance due to the presence of the impurities via Eqs. (5.5) and (5.12),

$$\delta G = 2 \times \frac{2e^2}{h} \frac{\mathrm{d}^2}{\mathrm{d}\phi^2} \ln \det \left(1 - \hat{\mathcal{T}}\hat{\mathcal{G}}_{\mathrm{reg}}\right)\big|_{\phi=0}, \tag{5.18}$$

where the additional factor 2 accounts for spin degeneracy. The regularized Green's function $\hat{\mathcal{G}}_{\mathrm{reg}}$ (see Eq. (5.13)) is obtained from the unperturbed Green's function $\mathcal{G}_0 = \check{G}$ (see Eq. (5.6)), which in a single valley and in the limit $W \to \infty$ is the solution to the equation (see Eq. (5.2))

$$\begin{pmatrix} \mu(x) - v_F\boldsymbol{\sigma} \cdot \mathbf{p} + \mathrm{i}0^+ & -\mathrm{i}\sinh(\phi/2)\hbar v_F\sigma_x\delta(x) \\ -\mathrm{i}\sinh(\phi/2)\hbar v_F\sigma_x\delta(x-L) & \mu(x) - v_F\boldsymbol{\sigma} \cdot \mathbf{p} - \mathrm{i}0^+ \end{pmatrix} \mathcal{G}_0(\mathbf{r}, \mathbf{r}') = \delta(\mathbf{r} - \mathbf{r}') \tag{5.19}$$

with $\mu(x) = \mu_\infty\Theta(|x - L/2| - L/2)$, $\mu_\infty \to \infty$, modeling the metallic character[9]—a high density of states—of the leads, where we chose $x_L = 0$ and $x_R = L$ without loss of generality, while transport in the region $0 < x < L$ occurs at the Dirac point; we further used that in graphene, Eq. (5.1) takes the form

$$\hat{\Gamma} = \mathrm{i}[v_F\boldsymbol{\sigma} \cdot \mathbf{p}, \hat{x}] = \hbar v_F\sigma_x.$$

The solution to Eq. (5.19) has first been derived in Ref. [Tit10] in the standard way via wavefunction matching of piecewise solutions, where μ_∞, the infinitesimal shift $\mathrm{i}0^+$, and the counting angle are incorporated into the boundary conditions. The final expression reads [Ost10]

$$\mathcal{G}_0(\mathbf{r}_n, \mathbf{r}_m) = \frac{\mathrm{i}}{4\hbar v_F L} U_{x_n}\Lambda\Sigma_z\mathrm{e}^{\mathrm{i}\Sigma_y(y_n - y_m)\phi/(2L)}R(\mathbf{r}_n, \mathbf{r}_m)\Lambda U_{x_m}^{-1}, \tag{5.20}$$

where $\Sigma_{x,y,z}$ are the Pauli matrices in RA space,

$$U_x \equiv \begin{pmatrix} \mathrm{i}\sinh\frac{\phi(x-L)}{2L} & \cosh\frac{\phi(x-L)}{2L} \\ \mathrm{i}\cosh\frac{\phi x}{2L} & -\sinh\frac{\phi x}{2L} \end{pmatrix}_{\mathrm{RA}} \quad \text{and} \quad \Lambda \equiv \begin{pmatrix} \mathbf{1} & 0 \\ 0 & \sigma_z \end{pmatrix}_{\mathrm{RA}}$$

are matrices in RA space, and

$$R(\mathbf{r}_n, \mathbf{r}_m) \equiv \begin{pmatrix} \sin^{-1}(z_n + z_m^*) & \sin^{-1}(z_n - z_m) \\ \sin^{-1}(z_n^* - z_m^*) & \sin^{-1}(z_n^* + z_m) \end{pmatrix}_\sigma, \qquad z_n \equiv \frac{\pi}{2L}(x_n + \mathrm{i}y_n),$$

is a matrix in sublattice space. According to Eq. (5.13), the off-diagonal elements of $\hat{\mathcal{G}}_{\mathrm{reg}}$ are then given by Eq. (5.20),

$$(\hat{\mathcal{G}}_{\mathrm{reg}})_{nm} = \mathcal{G}_0(\mathbf{r}_n, \mathbf{r}_m), \qquad n \neq m,$$

while for the diagonal elements, in addition the free Green's function of graphene at the

---

[9] Such a model was introduced earlier in Ref. [Two06].

Dirac point [Ben09a, Tit10, Ost10],

$$g(\mathbf{r}, \mathbf{r}') = g(\mathbf{r} - \mathbf{r}'), \qquad g(\mathbf{r}) = \frac{-\mathrm{i}\boldsymbol{\sigma} \cdot \mathbf{r}}{2\pi\hbar v_F r^2},$$

enters into Eq. (5.13); the final expression for the diagonal elements reads [Ost10]

$$(\hat{\mathcal{G}}_{\mathrm{reg}})_{nn} = \frac{\mathrm{i}}{4\hbar v_F L} U_{x_n} \Lambda \Sigma_z R_{\mathrm{reg}}(\mathbf{r}_n) \Lambda U_{x_n}^{-1}, \qquad R_{\mathrm{reg}}(\mathbf{r}) = \begin{pmatrix} \sin^{-1}(\pi x/L) & \Sigma_y \phi/\pi \\ -\Sigma_y \phi/\pi & \sin^{-1}(\pi x/L) \end{pmatrix}_\sigma.$$

With this, all ingredients to Eq. (5.18) have been established. Technical details and an efficient algorithm to evaluate Eq. (5.18) for an arbitrary number of impurities are further described in Ref. [Ost10]; in particular, for the case of two vacancies located at positions $\mathbf{r}_1$ and $\mathbf{r}_2$, respectively, corresponding to infinitely strong on-site potentials yielding a diverging scattering length, $\ell \to \infty$, the correction to the conductance takes the form [Sch11]

$$\delta G = \frac{4e^2}{h} \frac{\bar{y}^2}{L^2} \frac{\rho_{11}\rho_{22}\,\mathrm{Re}(\rho_{12}^2) - |\rho_{12}|^2(\mathrm{Re}\,\rho_{12})^2}{\left((\mathrm{Re}\,\rho_{12})^2 - \rho_{11}\rho_{22}\right)^2} \tag{5.21}$$

with $\bar{y} \equiv y_1 - y_2$ and

$$\rho_{ij} \equiv \mathrm{e}^{\mathrm{i}(\theta_i - \theta_j)/2} \csc \frac{\pi\left(\zeta_i x_i + \zeta_j x_j + \mathrm{i}(y_i - y_j)\right)}{2L},$$

where $\theta_i \equiv \alpha\zeta_i - \mathbf{K}\mathbf{r}_i$ is the T-matrix phase, which can take on one of six values $\theta_\pm^c \equiv \pm\alpha + 2\pi c/3$, $c = 0, \pm 1$, and $\zeta_i = \pm 1$ indicates the sublattice on which the vacancy is located (A $\hat{=} +1$ and B $\hat{=} -1$). The phase difference $\bar{\theta} \equiv \theta_1 - \theta_2$ encodes the dependence of the conductance on the colors of the vacancies and on the orientation angle α.

Results

To highlight the sensitivity of transport quantities to the colors of vacancy sites and in order to test the results obtained from the unfolded scattering formalism, we compute the conductance analytically from Eq. (5.21), which was obtained in the limit $W \to \infty$, as well as numerically in the usual nearest neighbor tight binding model (see Eq. (4.1)) for $W \gg L$ using the technique developed in Chapter 2 and the scheme for constructing the surface Green's functions of graphene leads exhibiting zigzag or armchair edges as outlined in Section 4.2. The lattice geometry used in the numerical calculation is schematically shown for armchair orientation ($\alpha = 0$) in Fig. 5.3(a). For the numerical simulations, we have chosen a sample length $L \approx 50a_0$ and a sample width $W \approx 600a_0$, and we consider two crystal orientations: $\alpha = 0$ (armchair) and $\alpha = \pi/6$ (zigzag). The metallic leads at $x < 0$ and $x > L$ are defined by a large chemical potential, $\mu_\infty^{\mathrm{num}} = 0.3t \approx 10\hbar v_F/L$, measured with respect to the Dirac point, which is chosen large enough to provide a sufficiently large number of propagating modes in the leads while still being within the validity regime of the low-energy approximation of graphene. Inside the sample ($0 < x < L$), the chemical potential is tuned to the close vicinity of the Dirac point, $\mu_0^{\mathrm{num}} = 0.001t$, avoiding numerical instabilities that occur directly at the Dirac point. In the absence of vacancies, the relative deviation of the
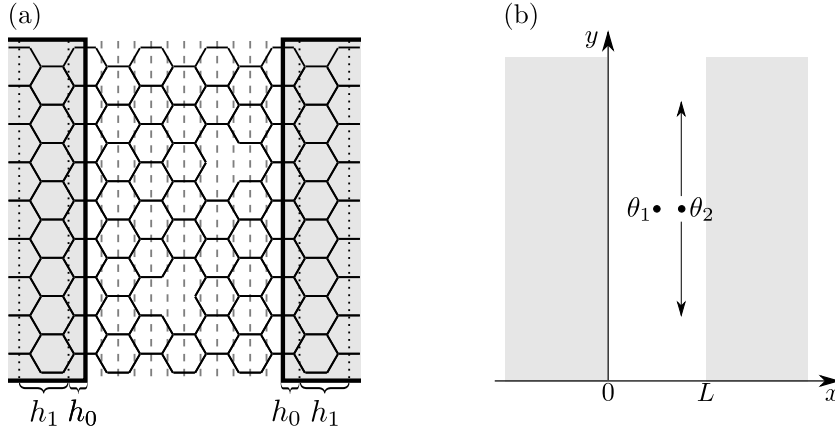
Figure 5.3: (a) Lattice geometry used in the numerical simulations, exemplary shown for armchair orientation ($\alpha = 0$). A vacancy site is created by setting all hopping matrix elements to or from this site to zero. The leads (shaded area) are defined according to Fig. 2.3 by the matrices h_0 and h_1 (as well as corresponding matrices h_{01} and h_{10} not indicated here). The layers used in the recursive scheme described in Section 2.4 are also indicated (dashed). (b) Setup for the plots shown in Figs. 5.4 and 5.5. One vacancy with phase θ_1 is kept fixed at the center of the sample while the second vacancy with phase θ_2 is shifted along y-direction for a given value of the x-coordinate.

conductivity from the theoretical minimal value $4e^2/(\pi h)$ (see Section 3.2) is found to be less than 1%. While a single vacancy has only a negligible effect on the numerically calculated ballistic conductance, a pair of vacancies leads to a finite correction δG. This behavior can be understood in terms of resonant tunneling via the bound states formed by vacancies. A single vacancy leads to a strong enhancement of the local density of states over the distance L from the vacancy due to formation of a resonant state at the Dirac point. Still, it does not produce any contribution to the conductance due to lack of coupling to the current-carrying states in the leads, owing to the interplay of spatial symmetry and the peculiar projective structure of the T-matrix, see Eq. (5.16). However, the symmetry of this state is, in general, broken in the presence of a second vacancy within a distance L due to hybridization with an energy splitting of order $\hbar v_F/L$ comparable to the width of the resonance. The resonant tunneling through this hybridized bound state provides an extra conducting channel hence yielding the L-independent correction $\delta G \sim e^2/h$ for $|\bar{y}| \sim L$, which we calculate numerically for different positions of one vacancy while keeping the second vacancy fixed in the center of the sample (see Fig. 5.3(b)).

The numerical and analytical results are compared in Figs. 5.4 and 5.5. One set of data is shown in Fig. 5.4 for $\alpha = 0$ and for vacancies of different type. One vacancy is kept fixed on sublattice A at position $\mathbf{r}_1 = (L/2, 0)$, a second vacancy is shifted along y-direction on sublattice B, $\mathbf{r}_2 = (x_2, y_2)$, where $x_2 \approx 2L/3$. The dependence of δG on all possible values of $\bar{y} = -y_2$ on the lattice is shown with the data points. The conductance switches between three different smooth curves which correspond to a certain difference $\bar{\theta} = \theta_1 - \theta_2$ of the T-matrix phase at the two vacated sites, $\bar{\theta} = 0$ and $\bar{\theta} = \pm 2\pi/3$, respectively. Similar data is plotted in Fig. 5.5(a) for the zigzag orientation of the crystal and for different transverse positions of the B vacancy at $x_2 \approx 0.45L$. Here, three other phase differences, $\bar{\theta} = \pi$ and
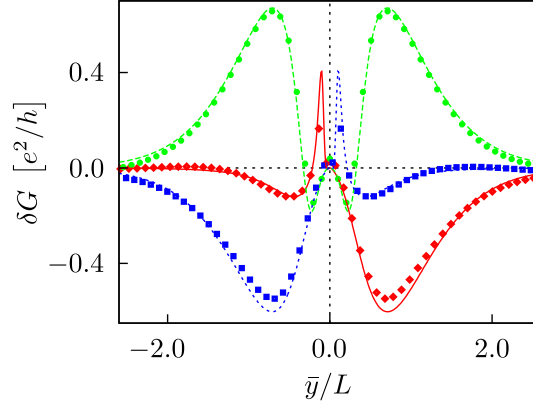
Figure 5.4: Conductance variation for an "armchair" ($\alpha = 0$) sample with two vacancies, one on each sublattice. By changing the distance in y-direction, $\bar{y}$, the conductance jumps on the atomic scale between three different smooth curves corresponding to $\bar{\theta} = 0$ (green disks), $\bar{\theta} = 2\pi/3$ (blue squares), and $\bar{\theta} = -2\pi/3$ (red diamonds), respectively. The numerical data agrees well with Eq. (5.21) as shown by the corresponding curves (Figure adapted from Ref. [Sch11]).
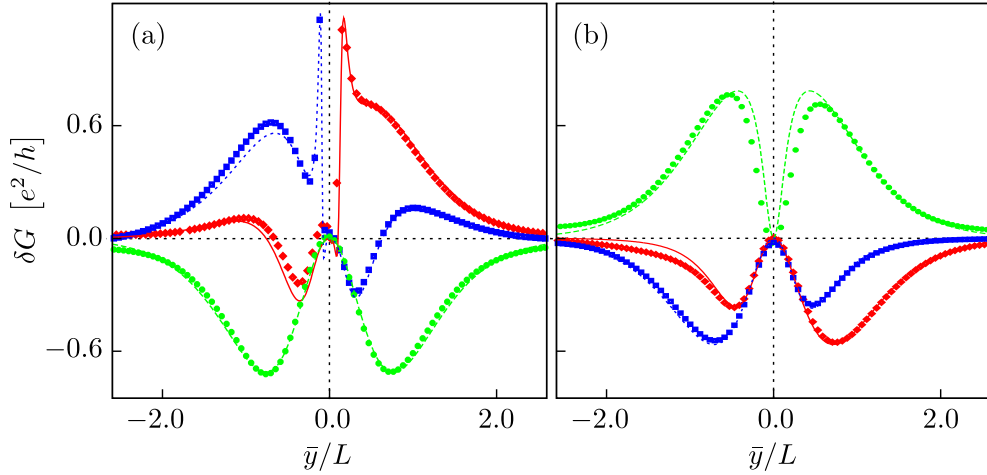

Figure 5.5: Conductance variation for a "zigzag" ($\alpha = \pi/6$) sample with two vacancies. (a) One vacancy on each sublattice; by changing $\bar{y}$, the conductance jumps on the atomic scale between different smooth curves corresponding to $\bar{\theta} = \pi$ (green disks), $\bar{\theta} = \pi/3$ (blue squares), and $\bar{\theta} = -\pi/3$ (red diamonds). (b) Both vacancies on sublattice A; here, the phase difference $\bar{\theta}$ is either 0 (green disks), $2\pi/3$ (blue squares), or $-2\pi/3$ (red diamonds). The numerical data agrees well with Eq. (5.21) as shown by the corresponding curves (Figure adapted from Ref. [Sch11]).

$\bar{\theta} = \pm\pi/3$, appear. In Fig. 5.5(b), both vacancies are chosen to belong to the A sublattice ($x_2 \approx L/3$, zigzag orientation). In this case, we find again $\bar{\theta} = 0$ and $\bar{\theta} = \pm 2\pi/3$ in agreement with the classification of site colors presented in Fig. 5.2.

Figs. 5.4 and 5.5 show a remarkable agreement between the numerical data obtained by the recursive Green's function technique and the analytical result, Eq. (5.21). The small deviations between analytical and numerical results are mainly due to the finite ratio W/L and the chosen finite chemical potential in the leads; a small detuning from the Dirac point within the sample, used in the simulations to avoid numerical instabilities as mentioned above, may also play a role. A good agreement with the theory is similarly obtained for other positions of the vacancies, except for deviations at $\bar{\theta} = 0$ in the limit $\mathbf{r}_2 \to \mathbf{r}_1$, where the approximation of non-overlapping impurities, Eq. (5.11), breaks down and Eq. (5.21) becomes indeterminate.

Virial expansion. In statistical mechanics, the partition function of a gas of interacting particles can in general not be obtained exactly. Instead, the partition function Z is decomposed into contributions Z_0, Z_1, Z_2, ... for 0, 1, 2, ... particles, and a perturbative treatment for low particle densities is employed in form of a so-called virial expansion. The virial expansion is an expansion of the equation of state of a gas of interacting particles in the particle density, where the zeroth order contribution is given by the equation of state of the ideal, non-interacting gas and the (virial) coefficients of higher order corrections are determined by the contributions Z_n, $n \in \mathbb{N}$ [Sch06].

Pseudodiffusive transport in the "short and wide" ($W \gg L$) geometry can be described by the mean conductivity $\sigma = G \times L/W$, and for a low concentration of vacancies, a corresponding expansion for σ in the impurity density can be established. The zeroth order term is given by the universal minimal value of the conductivity of graphene, $\sigma_{\min} = 4e^2/(\pi h)$. The first order correction is given by the effect of a single vacancy on the conductance, which in our case is absent as described above. The second order correction is given by the effect of two vacancies simultaneously present in the sample, which is non-trivial in our case. The lowest order term of this series is therefore of second order in impurity density and the series can be written in the form

$$\sigma = \frac{4e^2}{\pi h}\Bigg(1 + L^4 \sum_{c_1,c_2}\Big(\gamma_{\frac{2\pi}{3}(c_1-c_2)}\big(n_{Ac_1}n_{Ac_2} + n_{Bc_1}n_{Bc_2}\big)$$
$$+ 2\bar{\gamma}_{2\alpha + \frac{2\pi}{3}(c_1-c_2)}n_{Ac_1}n_{Bc_2}\Big) + \mathcal{O}(n^3 L^6)\Bigg), \quad (5.22)$$

where n_{Ac} and n_{Bc} with $c = 0, \pm 1$ are the impurity concentrations of the corresponding sites of the graphene superlattice (see Fig. 5.2) and $4e^2/(\pi h)$ is the universal minimal value of the conductivity at the Dirac point in the limit $W \gg L$ [Kat06a, Two06, Mia07, Dan08]. Performing numerical averaging over impurity positions in Eq. (5.21), we find the values $\gamma_0 \approx 0.2653$ and $\gamma_{\pm 2\pi/3} \approx -0.1197$, which are independent of the angle α. Both γ_χ and $\bar{\gamma}_\chi$ are even 2π-periodic functions of χ. The mean value of $\bar{\gamma}_\chi$ over the period is zero. In a sample with "armchair" orientation ($\alpha = 0$), relevant parameters are $\bar{\gamma}_0 \approx 0.1700$ and $\bar{\gamma}_{\pm 2\pi/3} \approx -0.0850$. In a "zigzag" sample ($\alpha = \pi/6$), we have $\bar{\gamma}_{\pm\pi/3} \approx 0.0843$ and

$\bar{\gamma}_\pi \approx -0.1686$. In each case, the sum of the three values is vanishingly small, $\sim 10^{-5}$. If impurities are distributed uniformly among the lattice sites, the conductivity is given by

$$\sigma = \frac{4e^2}{\pi h}(1 + \kappa n^2 L^4 + \mathcal{O}(n^3 L^6)), \tag{5.23}$$

where n is the impurity concentration and $\kappa \approx 0.0043$ exhibits tiny oscillations $\sim 10^{-5}$ as a function of α. However, the dependence of the (minimal) conductivity on the crystal orientation is substantial if the distribution of adatoms among sites of different colors is not uniform. Such a non-uniform distribution can originate from adatom correlations, for instance by electron-mediated interactions of on-site impurities, as described in Refs. [Shy09, Aba10a, Che09a]; the proposed color classification extends beyond zero energy and gives rise to interaction oscillations yielding a color scheme similar to that of Fig. 5.2. It is worth noting that Ref. [Shy09] addressed the problem in an infinite system, whereas the effective interaction of adatoms with the leads (encoded in Eq. (5.19)) may play an important role in a finite sample. Further, a strong on-site impurity of finite strength V_0 creates a resonance away from the Dirac point at energy t^2/V_0 and an imbalance in the distribution of such impurities over sublattices is predicted to open a gap in the vicinity of the Dirac point [Aba10b].

As a final remark, note that since the term linear in n vanishes in Eqs. (5.22) and (5.23) because scattering on a single vacancy is not sufficient to produce a correction to the conductivity, the finite correction shown in Figs. 5.4 and 5.5 is not to be interpreted as the sum of the (actually absent) effects of two independent scatterers but is rather a second order effect due to the presence of a dimer or pair of impurities. As a result, the leading correction to the conductivity of the disordered sample, Eq. (5.21), is of second order in the impurity concentration.

5.3 Summary and outlook

In the previous section, we theoretically proposed and numerically confirmed an extended classification of impurity sites in the graphene honeycomb lattice for the case of strongly bound adatoms or vacancies based on the unfolded scattering formalism developed in Section 5.1. The classification illustrated in Fig. 5.2 by assigning colors to the lattice sites gives rise to a color scheme with six inequivalent sites per supercell, three on each sublattice. The general analytical expression for the correction to the Dirac point conductance of a graphene sample with two resonant on-site impurities was given as a function of the impurity coordinates, see Eq. (5.21). The Dirac point conductivity of graphene with a small number of randomly distributed adatoms was shown to be sensitive to the relative concentration of impurities at the sites belonging to different sublattices and having different colors by means of a virial expansion. A non-uniform distribution of impurities within the color scheme is expected to cause a substantial dependence of the conductivity on the transport direction.

Potential future work may be concerned with the extension of the color classification beyond zero energy, where a non-uniform distribution of finite-energy resonant scatterers is predicted to open a gap [Aba10b]. Another topic is the analysis of the color dependence for the case of higher impurity concentrations beyond the validity of the virial expansion, whose lowest order term was inferred in the previous section solely on the basis of the two-vacancy
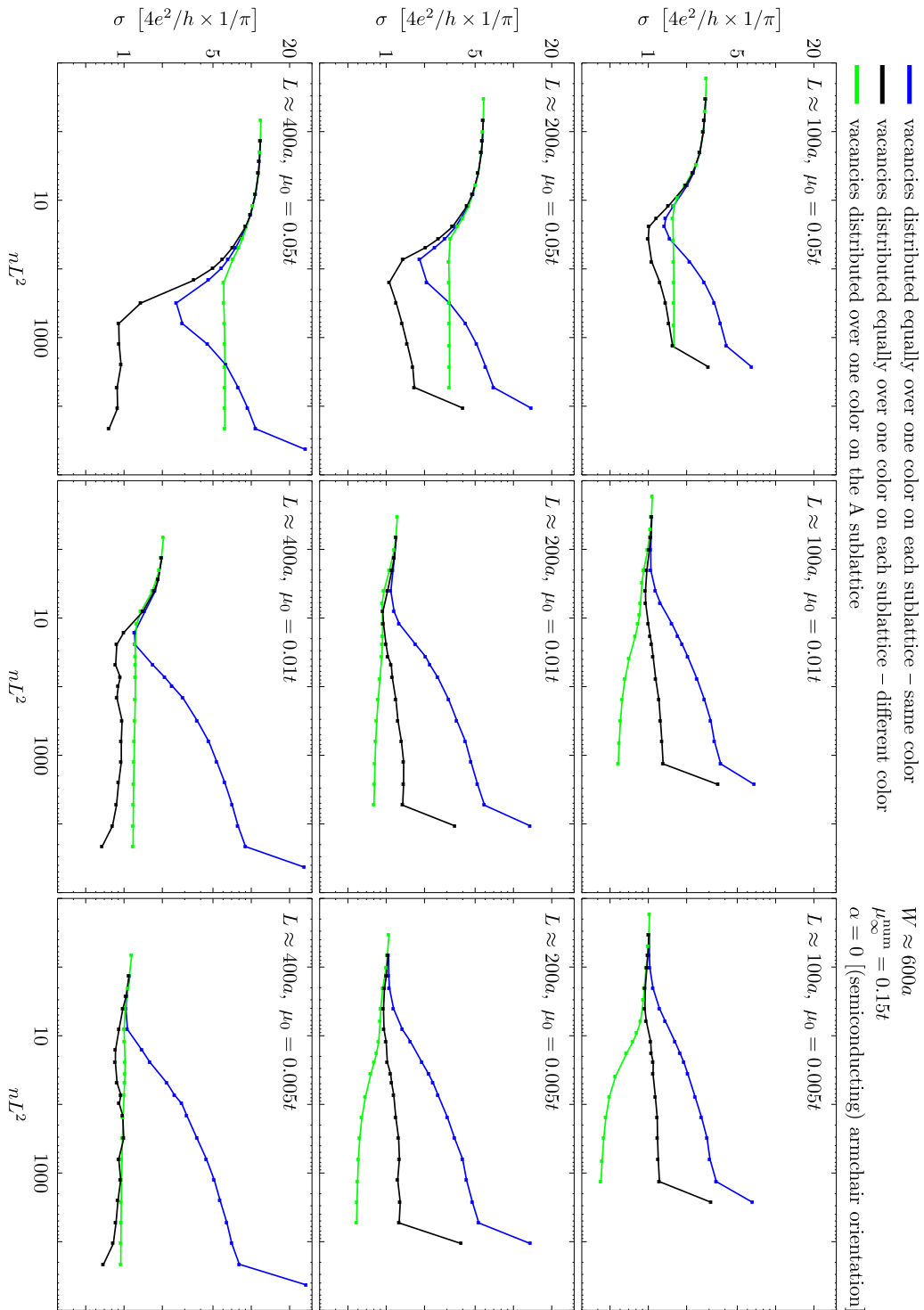
Figure 5.6: Dependence of the conductivity on the impurity density for different values of the length L and the chemical potential μ_0 in the region $0 < x < L$.
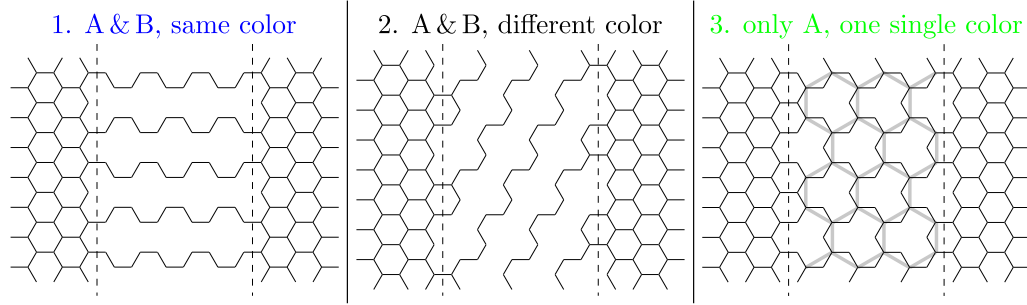
Figure 5.7: Lattice structures that emerge in the extreme case of maximum vacancy density for the three different impurity distributions shown in Fig. 5.6.

result, Eq. (5.21); in Fig. 5.6, we show preliminary numerical results on the behavior of the conductance in the presence of a finite impurity density for different distributions of impurities over sublattices and colors in (semiconducting) armchair orientation ($\alpha = 0$). The conductivity σ is shown in units of $4e^2/(\pi h)$ as a function of $nL^2 = N/(W/L)$, where N is the total number of impurities, so that n is the total impurity density. $W \approx 600a_0$ is the width of the sample, the chemical potential in the leads is $\mu_L = 0.15t$, and the chemical potential in the sample μ_S as well as the length L are as indicated in the individual plots. Each data point is averaged over 100 disorder realizations in the following three different disorder configurations:

1. Vacancies are distributed equally over a single color on each sublattice with equal colors on sublattices A and B (blue).

2. Vacancies are distributed equally over a single color on each sublattice with different colors on sublattices A and B (black).

3. Vacancies are distributed over a single color on sublattice A (green).

In Fig. 5.7, we also show the regular lattice structures that emerge in the extreme case of maximum impurity concentration, where transport is again ballistic as in the impurity-free case except for some contact resistance at the interfaces towards the leads. In configuration 1 (blue), an array of independent one-dimensional conducting channels connecting the leads emerges, and the number of channels increases linearly with the sample width W, while it is independent of the sample length L. In the plots shown in Fig. 5.6, the width W is kept constant and so is the number of channels and thus the conductance G, explaining the linear increase of the saturation value of the conductivity $\sigma = G \times L/W$ with increasing length at maximum impurity concentration. In configuration 2 (black), a similar array of independent one-dimensional conducting channels appears. However, these channels are tilted by an angle of 60°, so that there may be disconnected channels that do not connect the two leads. Hence, the number of conducting channels between the leads not only depends on the length but also explicitly on the width of the sample (and not only on the ratio W/L). While in configuration 1, there are $2W/(3\sqrt{3})$ channels in the system, the number of channels is $W/(3\sqrt{3})$ in configuration 2 if the length is sufficiently small so that there are no disconnected channels. Thus, the number of conducting channels connecting the

leads is always smaller at least by a factor of 2 compared to the same system geometry in configuration 1, and it decreases with increasing length explaining the saturation value of the conductivity of the black curves in Fig. 5.6 for maximum impurity concentration with respect to the corresponding blue curves.

Such a simple analysis is not possible for configuration 3 (green); however, note that in this case, the lattice structure that emerges at maximum impurity concentration can be considered as an effective honeycomb lattice with a nearest neighbor distance $\tilde{a}_0 = a_0\sqrt{3}$ in zigzag orientation which is connected to conventional graphene leads in armchair orientation (see Fig. 5.7). This consideration might help in the interpretation of the green curves in Fig. 5.6. A detailed theory and understanding of the behavior shown in Fig. 5.6, especially in the crossover regime of intermediate impurity concentration, has yet to be developed.

Chapter 6

Conclusion

The interplay between the peculiar electronic properties of graphene and the fundamental concepts of electronic transport in mesoscopic systems, namely quantum interference and disorder effects, formed the focus of the present work. In this chapter, we recapitulate the main findings obtained in the previous chapters and give a brief outlook on open questions.

Electronic transport in graphene, or in mesoscopic systems in general, involves many particles in a non-equilibrium situation. The first part of this thesis was concerned with the formulation of an appropriate language and a computational scheme for the description of quantum transport and the calculation of observables of interest. In Chapter 1, we introduced a very general field-theoretic non-equilibrium formalism capable of adequately expressing the problem at hand. This rather formal approach reduced to an intuitive picture for the case of (effectively) non-interacting systems, which we considered throughout this work. In Chapter 2, we outlined in detail an efficient computational scheme for the numerical evaluation of transport observables in terms of the single-particle Green's function as obtained in Chapter 1. In the second part of this thesis, we applied this scheme to graphene after giving a general introduction to this material in Chapter 3, highlighting the essential concepts and phenomena relevant for the subsequent analysis of graphene-specific effects in typical transport geometries. In particular, in Chapter 4, we focused on the Aharonov–Bohm geometry and, after providing a general overview of recent developments in the field, concentrated on the interplay with either of two fundamental phenomena specific to graphene, namely Klein tunneling and specular Andreev reflection. Introducing Klein tunneling into a ring-shaped system by applying a gate voltage to one of the ring arms and thus creating a *npn*-junction changes the amplitude of the magnetoconductance oscillations, with a considerable dependence on the smoothness of the junction. This behavior is in accordance with a previous analysis on the transmission properties of a *np*-junction in an infinite graphene sheet [Che06]. Introducing Andreev reflection by means of a superconducting contact, where electron–hole conversion may take place, leads to different dominant magnetoconductance oscillation periods of h/e for specular Andreev reflection—which is exclusive to graphene—and $h/(2e)$ for conventional retro reflection, depending on the ratio of Fermi energy and excitation energy (or applied bias). This signature of specular vs. retro reflection proves to be very robust due to the topological nature of the underlying detection mechanism. A second transport geometry, a strip of graphene in a two-terminal setup, was considered in Chapter 5, and the effect of disorder on the universal transport properties of ballistic graphene was studied. The particular kind of disorder under consideration have been vacancies in the graphene lattice, modeling the effect of strongly bound short-range scatterers such as adatoms or molecules, that support electronic states at zero energy and thus represent resonant scatterers

for the Dirac quasiparticles. The point-like character of these impurities allowed for an analytical treatment in the framework of the Dirac equation, in addition to a numerical analysis utilizing the tight binding model. Both descriptions show a remarkable agreement on the results, which led to the construction of a non-trivial color scheme explaining the surprising dependence of the conductance on the particular locations of the vacancies within a supercell containing in general six inequivalent sites, three per sublattice. The origin of this classification is quantum interference between the two valleys of the graphene dispersion. The conductivity is further found to exhibit a dependence on the transport direction, which is strongly enhanced if the distribution among the sites of the lattice is not uniform.

The effect of resonant scatterers has been extensively studied for the case of two vacancies that are present in the system. Preliminary results on the situation at finite impurity concentration have also been given in Section 5.3. Although some of the features shown there can be easily understood by a consideration of the lattice structures that emerge at extreme impurity concentrations, further analysis is required for a detailed understanding, especially for the situation at intermediate impurity concentration. Since the energy states created at the Dirac point by the presence of resonant scatterers exhibit a finite width of the resonance, it is also instructive to analyze the energy dependence of the conductivity in a vicinity around the charge neutrality point. Another interesting aspect is given by less strongly bound impurities, which shift the resonance to finite energies, in which case a gap is predicted to open [Aba10b]. Concerning the Aharonov–Bohm effect in graphene, we have identified unresolved issues in recent measurements as well as theoretical considerations not yet confirmed by corresponding experiments. In Ref. [Rus08], a seemingly linear relation between conductance and magnetooscillation amplitude has been observed and remains to be explored; the same experiment also showed an yet unexplained increase of the oscillation amplitude at high field strengths. The two transport setups discussed theoretically in Chapter 4 should in general be accessible to an experimental realization, and indeed, the setup considered in Section 4.2 has just recently been realized experimentally [Smi12]. In this setup, an unusual increase of the oscillation amplitude with increasing magnetic field strength was observed in some—but not all—cases, when the lower ring arm was tuned toward the charge neutrality point; this phenomenon could not be explained. We also note that experimentally, the electrostatic Aharonov–Bohm effect may be utilized instead of the application of a magnetic field, which might prove useful especially in the setup discussed in Section 4.3 due to the presence of a superconducting lead; also note that in this system, the electron–hole pair is spatially separated in the case of specular Andreev reflection, so that its entangled property may be utilized in (spin) entanglement devices based on graphene; for such applications, graphene proves to be a prime material anyway due to its low spin–orbit and hyperfine interactions and a correspondingly large spin coherence length [Tra07].

Appendix A

Explicit solutions to the Dyson equation

The two forms of the Dyson equation read

$$g + gVG = G = g + GVg.$$

Two-layer case

For

$$G = \begin{pmatrix} G_1 & G_{12} \\ G_{21} & G_2 \end{pmatrix}, \qquad g = \begin{pmatrix} g_1 & \mathbf{0} \\ \mathbf{0} & (E-H)^{-1} \end{pmatrix}, \qquad V = \begin{pmatrix} \mathbf{0} & T \\ T^\dagger & \mathbf{0} \end{pmatrix},$$

the two forms of the Dyson equation can be written in components

$$
\begin{aligned}
g_1 + g_1 T G_{21} = G_1 &= g_1 + G_{12} T^\dagger g_1, \\
g_1 T G_2 = G_{12} &= G_1 T (E-H)^{-1}, \\
(E-H)^{-1} T^\dagger G_1 = G_{21} &= G_2 T^\dagger g_1, \\
(E-H)^{-1}(\mathbf{1} + T^\dagger G_{12}) = G_2 &= (\mathbf{1} + G_{21} T)(E-H)^{-1},
\end{aligned}
$$

and analogous to the derivation of Eq. (2.7) (or directly solving for G_2), we find

$$G_2 = (E - H - T^\dagger g_1 T)^{-1},$$

or, if G_1 is known instead of g_1 (as in the derivation of Eq. (2.18)), we can write

$$G_2 = g_2 + g_2 T^\dagger G_1 T g_2, \tag{A.1}$$

where we defined $g_2 = (E-H)^{-1}$.

Three-layer case

For

$$G = \begin{pmatrix} G_1 & G_{12} & G_{13} \\ G_{21} & G_2 & G_{23} \\ G_{31} & G_{32} & G_3 \end{pmatrix}, \quad g = \begin{pmatrix} g_1 & g_{12} & \mathbf{0} \\ g_{21} & g_2 & \mathbf{0} \\ \mathbf{0} & \mathbf{0} & (E-H)^{-1} \end{pmatrix}, \quad V = \begin{pmatrix} \mathbf{0} & \mathbf{0} & T \\ \mathbf{0} & \mathbf{0} & h \\ T^\dagger & h^\dagger & \mathbf{0} \end{pmatrix},$$

the two forms of the Dyson equation can be written in components

$$
\begin{aligned}
g_1 + (g_1 T + g_{12} h) G_{31} = G_1 &= g_1 + G_{13}(T^\dagger g_1 + h^\dagger g_{21}), \\
g_{12} + (g_1 T + g_{12} h) G_{32} = G_{12} &= g_{12} + G_{13}(T^\dagger g_{12} + h^\dagger g_2), \\
(g_1 T + g_{12} h) G_3 = G_{13} &= (G_1 T + G_{12} h)(E - H)^{-1}, \\
g_{21} + (g_{21} T + g_2 h) G_{31} = G_{21} &= g_{21} + G_{23}(T^\dagger g_1 + h^\dagger g_{21}), \\
g_2 + (g_{21} T + g_2 h) G_{32} = G_2 &= g_2 + G_{23}(T^\dagger g_{12} + h^\dagger g_2), \\
(g_{21} T + g_2 h) G_3 = G_{23} &= (G_{21} T + G_2 h)(E - H)^{-1}, \\
(E - H)^{-1}(T^\dagger G_1 + h^\dagger G_{21}) = G_{31} &= G_3(T^\dagger g_1 + h^\dagger g_{21}), \\
(E - H)^{-1}(T^\dagger G_{12} + h^\dagger G_2) = G_{32} &= G_3(T^\dagger g_{12} + h^\dagger g_2), \\
(E - H)^{-1}(\mathbf{1} + T^\dagger G_{13} + h^\dagger G_{23}) = G_3 &= (\mathbf{1} + G_{31} T + G_{32} h)(E - H)^{-1},
\end{aligned}
$$

where the equations not used in Section 2.4 are shaded gray, and analogous to the derivation of Eq. (2.7) (or directly solving for G_3), we find

$$
G_3 = \left(E - H - (T^\dagger g_1 T + T^\dagger g_{12} h + h^\dagger g_{21} T + h^\dagger g_2 h) \right)^{-1}.
$$

Bibliography

[Aba10a] D. Abanin and L. Levitov. *Spatial Ordering of Defects and Conductivity of Functionalized Graphene* (2010). `arXiv:1008.1424v1`.

[Aba10b] D. A. Abanin, A. V. Shytov, and L. S. Levitov. *Peierls-Type Instability and Tunable Band Gap in Functionalized Graphene*. Phys. Rev. Lett. **105**, 086802 (2010).

[Abe08] D. S. L. Abergel, V. M. Apalkov, and T. Chakraborty. *Interplay between valley polarization and electron-electron interaction in a graphene ring*. Phys. Rev. B **78**, 193405 (2008).

[Abe11] N. Abedpour, R. Asgari, and F. Guinea. *Strains and pseudomagnetic fields in circular graphene rings*. Phys. Rev. B **84**, 115437 (2011).

[Aha59] Y. Aharonov and D. Bohm. *Significance of Electromagnetic Potentials in the Quantum Theory*. Phys. Rev. **115**, 485 (1959).

[Aha61] Y. Aharonov and D. Bohm. *Further Considerations on Electromagnetic Potentials in the Quantum Theory*. Phys. Rev. **123**, 1511 (1961).

[Akh08a] A. R. Akhmerov, J. H. Bardarson, A. Rycerz, and C. W. J. Beenakker. *Theory of the valley-valve effect in graphene nanoribbons*. Phys. Rev. B **77**, 205416 (2008).

[Akh08b] A. R. Akhmerov and C. W. J. Beenakker. *Boundary conditions for Dirac fermions on a terminated honeycomb lattice*. Phys. Rev. B **77**, 085423 (2008).

[And64] A. F. Andreev. *Thermal conductivity of the intermediate state of superconductors*. Sov. Phys. JETP **19**, 1228 (1964).

[And98] T. Ando, T. Nakanishi, and R. Saito. *Berry's Phase and Absence of Back Scattering in Carbon Nanotubes*. J. Phys. Soc. Jpn. **67**, 2857 (1998).

[And09] T. Ando. *The electronic properties of graphene and carbon nanotubes*. NPG Asia Mater. **1**, 17 (2009).

[Ang07] L. Angers, E. Zakka-Bajjani, R. Deblock, S. Guéron, H. Bouchiat, A. Cavanna, U. Gennser, and M. Polianski. *Magnetic-field asymmetry of mesoscopic dc rectification in Aharonov-Bohm rings*. Phys. Rev. B **75**, 115309 (2007).

[Ash76] N. Ashcroft and N. Mermin. *Solid state physics*. Harcourt (1976).

[Bac99] A. Bachtold, C. Strunk, J.-P. Salvetat, J.-M. Bonard, L. Forro, T. Nussbaumer, and C. Schönenberger. *Aharonov-Bohm oscillations in carbon nanotubes.* Nature **397**, 673 (1999).

[Bah09] D. A. Bahamon, A. L. C. Pereira, and P. A. Schulz. *Inner and outer edge states in graphene rings: A numerical investigation.* Phys. Rev. B **79**, 125414 (2009).

[Bas08] D. M. Basko. *Resonant low-energy electron scattering on short-range impurities in graphene.* Phys. Rev. B **78**, 115432 (2008).

[Bee91] C. W. J. Beenakker and H. van Houten. *Quantum Transport in Semiconductor Nanostructures.* Solid State Phys. **44**, 1 (1991).

[Bee06] C. W. J. Beenakker. *Specular Andreev Reflection in Graphene.* Phys. Rev. Lett. **97**, 067007 (2006).

[Bee08a] C. W. J. Beenakker. *Colloquium: Andreev reflection and Klein tunneling in graphene.* Rev. Mod. Phys. **80**, 1337 (2008).

[Bee08b] C. W. J. Beenakker, A. R. Akhmerov, P. Recher, and J. Tworzydło. *Correspondence between Andreev reflection and Klein tunneling in bipolar graphene.* Phys. Rev. B **77**, 075409 (2008).

[Ben09a] C. Bena. *Green's functions and impurity scattering in graphene.* Phys. Rev. B **79**, 125427 (2009).

[Ben09b] C. Bena and G. Montambaux. *Remarks on the tight-binding model of graphene.* New J. Phys. **11**, 095003 (2009).

[Blo29] F. Bloch. *Über die Quantenmechanik der Elektronen in Kristallgittern.* Z. Phys. A **52**, 555 (1929).

[Bol08] K. Bolotin, K. Sikes, Z. Jiang, M. Klima, G. Fudenberg, J. Hone, P. Kim, and H. Stormer. *Ultrahigh electron mobility in suspended graphene.* Solid State Commun. **146**, 351 (2008).

[Boy73] T. H. Boyer. *Classical Electromagnetic Deflections and Lag Effects Associated with Quantum Interference Pattern Shifts: Considerations Related to the Aharonov-Bohm Effect.* Phys. Rev. D **8**, 1679 (1973).

[Bre06a] L. Brey and H. A. Fertig. *Edge states and the quantized Hall effect in graphene.* Phys. Rev. B **73**, 195408 (2006).

[Bre06b] L. Brey and H. A. Fertig. *Electronic states of graphene nanoribbons studied with the Dirac equation.* Phys. Rev. B **73**, 235411 (2006).

[Bre07] L. Brey and H. A. Fertig. *Elementary electronic excitations in graphene nanoribbons.* Phys. Rev. B **75**, 125434 (2007).

[Bro12]   M. Brookes. *The Matrix Reference Manual* (2011; URL last accessed: May 3, 2012).
URL `http://www.ee.imperial.ac.uk/hp/staff/dmb/matrix/intro.html`

[Büt85]   M. Büttiker, Y. Imry, R. Landauer, and S. Pinhas. *Generalized many-channel conductance formula with application to small rings.* Phys. Rev. B **31**, 6207 (1985).

[Che06]   V. V. Cheianov and V. I. Fal'ko. *Selective transmission of Dirac electrons and ballistic magnetoresistance of n-p junctions in graphene.* Phys. Rev. B **74**, 041403 (2006).

[Che09a]   V. V. Cheianov, O. Syljuåsen, B. L. Altshuler, and V. Fal'ko. *Ordered states of adatoms on graphene.* Phys. Rev. B **80**, 233409 (2009).

[Che09b]   S.-G. Cheng, Y. Xing, J. Wang, and Q.-F. Sun. *Controllable Andreev Retroreflection and Specular Andreev Reflection in a Four-Terminal Graphene-Superconductor Hybrid System.* Phys. Rev. Lett. **103**, 167003 (2009).

[Che11]   S.-G. Cheng, H. Zhang, and Q.-F. Sun. *Effect of electron-hole inhomogeneity on specular Andreev reflection and Andreev retroreflection in a graphene-superconductor hybrid system.* Phys. Rev. B **83**, 235403 (2011).

[CN09]   A. H. Castro Neto, F. Guinea, N. M. R. Peres, K. S. Novoselov, and A. K. Geim. *The electronic properties of graphene.* Rev. Mod. Phys. **81**, 109 (2009).

[Cra68]   R. A. Craig. *Perturbation Expansion for Real-Time Green's Functions.* J. Math. Phys. **9**, 605 (1968).

[Dan08]   R. Danneau, F. Wu, M. F. Craciun, S. Russo, M. Y. Tomi, J. Salmilehto, A. F. Morpurgo, and P. J. Hakonen. *Shot Noise in Ballistic Graphene.* Phys. Rev. Lett. **100**, 196802 (2008).

[Dat05]   S. Datta. *Electronic transport in mesoscopic systems.* Cambridge University Press (2005).

[Dav93]   J. H. Davies, S. Hershfield, P. Hyldgaard, and J. W. Wilkins. *Current and rate equation for resonant tunneling.* Phys. Rev. B **47**, 4603 (1993).

[Dev76]   J. Devreese and V. Doren. *Linear and nonlinear electron transport in solids.* Plenum Press (1976).

[DiC08]   L. DiCarlo, J. R. Williams, Y. Zhang, D. T. McClure, and C. M. Marcus. *Shot Noise in Graphene.* Phys. Rev. Lett. **100**, 156801 (2008).

[Dre02]   M. S. Dresselhaus and G. Dresselhaus. *Intercalation compounds of graphite.* Adv. Phys. **51**, 1 (2002).

[DS11]   S. Das Sarma, S. Adam, E. H. Hwang, and E. Rossi. *Electronic transport in two-dimensional graphene.* Rev. Mod. Phys. **83**, 407 (2011).

[Du08] X. Du, I. Skachko, and E. Y. Andrei. *Towards ballistic transport in graphene.* Int. J. Mod. Phys. B **22**, 4579 (2008).

[Ehr49] W. Ehrenberg and R. E. Siday. *The Refractive Index in Electron Optics and the Principles of Dynamics.* Proc. Phys. Soc. B **62**, 8 (1949).

[Eli09] D. C. Elias, R. R. Nair, T. M. G. Mohiuddin, S. V. Morozov, P. Blake, M. P. Halsall, A. C. Ferrari, D. W. Boukhvalov, M. I. Katsnelson, A. K. Geim, and K. S. Novoselov. *Control of Graphene's Properties by Reversible Hydrogenation: Evidence for Graphane.* Science **323**, 610 (2009).

[Fer06] A. C. Ferrari, J. C. Meyer, V. Scardaci, C. Casiraghi, M. Lazzeri, F. Mauri, S. Piscanec, D. Jiang, K. S. Novoselov, S. Roth, and A. K. Geim. *Raman Spectrum of Graphene and Graphene Layers.* Phys. Rev. Lett. **97**, 187401 (2006).

[Fer10] H. A. Fertig and L. Brey. *Nanophysics in graphene: neutrino physics in quantum rings and superlattices.* Philos. T. Roy. Soc. A **368**, 5483 (2010).

[Fey39] R. P. Feynman. *Forces in Molecules.* Phys. Rev. **56**, 340 (1939).

[Fis81] D. S. Fisher and P. A. Lee. *Relation between conductivity and transmission matrix.* Phys. Rev. B **23**, 6851 (1981).

[Fuj96] M. Fujita, K. Wakabayashi, K. Nakada, and K. Kusakabe. *Peculiar Localized State at Zigzag Graphite Edge.* J. Phys. Soc. Jpn. **65**, 1920 (1996).

[Gei07] A. K. Geim and K. S. Novoselov. *The rise of graphene.* Nat. Mater. **6**, 183 (2007).

[Gei09] A. K. Geim. *Graphene: Status and Prospects.* Science **324**, 1530 (2009).

[Gen99] P. G. de Gennes. *Superconductivity Of Metals And Alloys.* Westview Press (1999).

[gra12] Graphene Industries Ltd. (2007; URL last accessed: May 3, 2012). URL http://grapheneindustries.com/

[Gup06] A. Gupta, G. Chen, P. Joshi, S. Tadigadapa, and Eklund. *Raman Scattering from High-Frequency Phonons in Supported n-Graphene Layer Films.* Nano Lett. **6**, 2667 (2006).

[Hau96] H. Haug and A. Jauho. *Quantum kinetics in transport and optics of semiconductors.* Springer (1996).

[Hau10] H. Haugen, D. Huertas-Hernando, A. Brataas, and X. Waintal. *Crossed Andreev reflection versus electron transfer in three-terminal graphene devices.* Phys. Rev. B **81**, 174523 (2010).

[Hee07] H. B. Heersche, P. Jarillo-Herrero, J. B. Oostinga, L. M. K. Vandersypen, and A. F. Morpurgo. *Bipolar supercurrent in graphene.* Nature **446**, 56 (2007).

[Hel37] H. Hellmann. *Einführung in die Quantenchemie.* F. Deuticke (1937).

[Hen07] M. Hentschel and F. Guinea. *Orthogonality catastrophe and Kondo effect in graphene.* Phys. Rev. B **76**, 115407 (2007).

[Hob53] J. P. Hobson and W. A. Nierenberg. *The Statistics of a Two-Dimensional, Hexagonal Net.* Phys. Rev. **89**, 662 (1953).

[Hol32] R. Holm and W. Meissner. *Messungen mit Hilfe von flüssigem Helium. XIII.* Z. Phys. A **74**, 715 (1932).

[Hov53] L. van Hove. *The Occurrence of Singularities in the Elastic Frequency Distribution of a Crystal.* Phys. Rev. **89**, 1189 (1953).

[Hue09] M. Huefner, F. Molitor, A. Jacobsen, A. Pioda, C. Stampfer, K. Ensslin, and T. Ihn. *Investigation of the Aharonov–Bohm effect in a gated graphene ring.* Phys. Status Solidi B **246**, 2756 (2009).

[Hue10] M. Huefner, F. Molitor, A. Jacobsen, A. Pioda, C. Stampfer, K. Ensslin, and T. Ihn. *The Aharonov–Bohm effect in a side-gated graphene ring.* New J. Phys. **12**, 043054 (2010).

[Kad62] L. Kadanoff and G. Baym. *Quantum statistical mechanics: Green's function methods in equilibrium and nonequilibrium problems.* W.A. Benjamin (1962).

[Kat06a] M. I. Katsnelson. *Zitterbewegung, chirality, and minimal conductivity in graphene.* Eur. Phys. J. B **51**, 157 (2006).

[Kat06b] M. I. Katsnelson, K. S. Novoselov, and A. K. Geim. *Chiral tunnelling and the Klein paradox in graphene.* Nat. Phys. **2**, 620 (2006).

[Kat10a] J. Katoch, J.-H. Chen, R. Tsuchikawa, C. W. Smith, E. R. Mucciolo, and M. Ishigami. *Uncovering the dominant scatterer in graphene sheets on SiO_2.* Phys. Rev. B **82**, 081417 (2010).

[Kat10b] M. I. Katsnelson. *Aharonov-Bohm effect in undoped graphene: Magnetotransport via evanescent waves.* Eur. Phys. Lett. **89**, 17001 (2010).

[Kel65] L. V. Keldysh. *Diagram technique for nonequilibrium processes.* Sov. Phys. JETP **20**, 1018 (1965).

[Kit96] C. Kittel. *Introduction to Solid State Physics.* Wiley (1996).

[Kle29] O. Klein. *Die Reflexion von Elektronen an einem Potentialsprung nach der relativistischen Dynamik von Dirac.* Z. Phys. A **53**, 157 (1929).

[Krs02] P. S. Krstić, X.-G. Zhang, and W. H. Butler. *Generalized conductance formula for the multiband tight-binding model.* Phys. Rev. B **66**, 205319 (2002).

[Lan57] R. Landauer. *Spatial Variation of Currents and Fields Due to Localized Scatterers in Metallic Conduction.* IBM J. Res. Dev. **1**, 223 (1957).

[Lan72] D. C. Langreth and J. W. Wilkins. *Theory of Spin Resonance in Dilute Magnetic Alloys.* Phys. Rev. B **6**, 3189 (1972).

[Lat09] Y. Latyshev, A. Latyshev, A. Orlov, A. Shchekin, V. Bykov, P. Monceau, K. van der Beck, M. Kontsikovskii, and I. Monnet. *Field-periodic magnetoresistance oscillations in thin graphite single crystals with columnar defects.* JETP Lett. **90**, 480 (2009).

[Lat10] Y. U. I. Latyshev, A. P. Orlov, E. G. Shustin, N. V. Isaev, W. Escoffier, P. Monceau, C. J. van der Beek, M. Konczykowski, and I. Monnet. *Aharonov-Bohm effect on columnar defects in thin graphite and graphene.* J. Phys.: Conf. Ser. **248**, 012001 (2010).

[Leb09] S. Lebègue, M. Klintenberg, O. Eriksson, and M. I. Katsnelson. *Accurate electronic band gap of pure and functionalized graphane from GW calculations.* Phys. Rev. B **79**, 245117 (2009).

[Lee81a] D. H. Lee and J. D. Joannopoulos. *Simple scheme for surface-band calculations. II. The Green's function.* Phys. Rev. B **23**, 4997 (1981).

[Lee81b] P. A. Lee and D. S. Fisher. *Anderson Localization in Two Dimensions.* Phys. Rev. Lett. **47**, 882 (1981).

[Lev93] L. S. Levitov and G. B. Lesovik. *Charge distribution in quantum shot noise.* JETP Lett. **58**, 230 (1993).

[Liu08] L. Liu, S. Ryu, M. R. Tomasik, E. Stolyarova, N. Jung, M. S. Hybertsen, M. L. Steigerwald, L. E. Brus, and G. W. Flynn. *Graphene Oxidation: Thickness-Dependent Etching and Strong Chemical Doping.* Nano Lett. **8**, 1965 (2008).

[Luo09] T. Luo, A. P. Iyengar, H. A. Fertig, and L. Brey. *Effective time-reversal symmetry breaking and energy spectra of graphene armchair rings.* Phys. Rev. B **80**, 165310 (2009).

[Ma09] M. M. Ma, J. W. Ding, and N. Xu. *Odd-even width effect on persistent current in zigzag hexagonal graphene rings.* Nanoscale **1**, 387 (2009).

[Ma10] M. Ma and J. Ding. *Geometry dependence of persistent currents in diamond-like graphene rings.* Solid State Commun. **150**, 1196 (2010).

[Mac85] A. MacKinnon. *The calculation of transport properties and density of states of disordered solids.* Z. Phys. B **59**, 385 (1985).

[McC04] E. McCann and V. I. Fal'Ko. *Symmetry Properties of Impurities in Metallic Single-Wall Carbon Nanotubes.* Int. J. Mod. Phys. B **18**, 3195 (2004).

[McC06] E. McCann, K. Kechedzhi, V. I. Fal'ko, H. Suzuura, T. Ando, and B. L. Altshuler. *Weak-Localization Magnetoresistance and Valley Symmetry in Graphene.* Phys. Rev. Lett. **97**, 146805 (2006).

[Mei92] Y. Meir and N. S. Wingreen. *Landauer formula for the current through an interacting electron region.* Phys. Rev. Lett. **68**, 2512 (1992).

[Mes09] A. Mesaros, D. Sadri, and J. Zaanen. *Berry phase of dislocations in graphene and valley conserving decoherence.* Phys. Rev. B **79**, 155111 (2009).

[Mia07] F. Miao, S. Wijeratne, Y. Zhang, U. C. Coskun, W. Bao, and C. N. Lau. *Phase-Coherent Transport in Graphene Quantum Billiards.* Science **317**, 1530 (2007).

[Moo65] G. E. Moore. *Cramming more components onto integrated circuits.* Electronics **38** (1965).

[Mos09] A. S. Moskalenko and J. Berakdar. *Light-induced valley currents and magnetization in graphene rings.* Phys. Rev. B **80**, 193407 (2009).

[Mun11] J. Munárriz, F. Domínguez-Adame, and A. V. Malyshev. *Toward graphene-based quantum interference devices.* Nanotech. **22**, 365201 (2011).

[Nak96] K. Nakada, M. Fujita, G. Dresselhaus, and M. S. Dresselhaus. *Edge state in graphene ribbons: Nanometer size effect and edge shape dependence.* Phys. Rev. B **54**, 17954 (1996).

[Naz94] Y. V. Nazarov. *Limits of universality in disordered conductors.* Phys. Rev. Lett. **73**, 134 (1994).

[Naz95] Y. V. Nazarov. *Weak localization and the transmission matrix.* Phys. Rev. B **52**, 4720 (1995).

[Ni10] Z. H. Ni, L. A. Ponomarenko, R. R. Nair, R. Yang, S. Anissimova, I. V. Grigorieva, F. Schedin, P. Blake, Z. X. Shen, E. H. Hill, K. S. Novoselov, and A. K. Geim. *On Resonant Scatterers As a Factor Limiting Carrier Mobility in Graphene.* Nano Lett. **10**, 3868 (2010).

[Nik01] B. K. Nikolić. *Deconstructing Kubo formula usage: Exact conductance of a mesoscopic system from weak to strong disorder limit.* Phys. Rev. B **64**, 165303 (2001).

[Nol05] W. Nolting. *Grundkurs Theoretische Physik 7: Viel-Teilchen-Theorie.* Springer (2005).

[Nov04] K. S. Novoselov, A. K. Geim, S. V. Morozov, D. Jiang, Y. Zhang, S. V. Dubonos, I. V. Grigorieva, and A. A. Firsov. *Electric Field Effect in Atomically Thin Carbon Films.* Science **306**, 666 (2004).

[Nov05] K. S. Novoselov, A. K. Geim, S. V. Morozov, D. Jiang, M. I. Katsnelson, I. V. Grigorieva, S. V. Dubonos, and A. A. Firsov. *Two-dimensional gas of massless Dirac fermions in graphene.* Nature **438**, 197 (2005).

[Nov07] D. S. Novikov. *Elastic scattering theory and transport in graphene.* Phys. Rev. B **76**, 245435 (2007).

[Nov11] K. S. Novoselov. *Nobel Lecture: Graphene: Materials in the Flatland.* Rev. Mod. Phys. **83**, 837 (2011).

[Ost06] P. M. Ostrovsky, I. V. Gornyi, and A. D. Mirlin. *Electron transport in disordered graphene.* Phys. Rev. B **74**, 235443 (2006).

[Ost10] P. M. Ostrovsky, M. Titov, S. Bera, I. V. Gornyi, and A. D. Mirlin. *Diffusion and Criticality in Undoped Graphene with Resonant Scatterers.* Phys. Rev. Lett. **105**, 266803 (2010).

[Pei33] R. Peierls. *Zur Theorie des Diamagnetismus von Leitungselektronen.* Z. Phys. A **80**, 763 (1933).

[Per06] V. M. Pereira, F. Guinea, J. M. B. Lopes dos Santos, N. M. R. Peres, and A. H. Castro Neto. *Disorder Induced Localized States in Graphene.* Phys. Rev. Lett. **96**, 036801 (2006).

[Per08] V. M. Pereira, J. M. B. Lopes dos Santos, and A. H. Castro Neto. *Modeling disorder in graphene.* Phys. Rev. B **77**, 115109 (2008).

[Por95] D. Porezag, T. Frauenheim, T. Köhler, G. Seifert, and R. Kaschner. *Construction of tight-binding-like potentials on the basis of density-functional theory: Application to carbon.* Phys. Rev. B **51**, 12947 (1995).

[Pot09] P. Potasz, A. D. Güçlü, and P. Hawrylak. *Electronic Shells of Dirac Fermions in Graphene Quantum Rings in a Magnetic Field.* Acta Phys. Pol. A **116**, 832 (2009).

[Pot10] P. Potasz, A. D. Güçlü, and P. Hawrylak. *Spin and electronic correlations in gated graphene quantum rings.* Phys. Rev. B **82**, 075425 (2010).

[Pra07] E. Prada, P. San-Jose, B. Wunsch, and F. Guinea. *Pseudodiffusive magnetotransport in graphene.* Phys. Rev. B **75**, 113407 (2007).

[Rai09] D. Rainis, F. Taddei, F. Dolcini, M. Polini, and R. Fazio. *Andreev reflection in graphene nanoribbons.* Phys. Rev. B **79**, 115131 (2009).

[Ram07] J. Rammer. *Quantum field theory of non-equilibrium states.* Cambridge University Press (2007).

[Rec07] P. Recher, B. Trauzettel, A. Rycerz, Y. M. Blanter, C. W. J. Beenakker, and A. F. Morpurgo. *Aharonov-Bohm effect and broken valley degeneracy in graphene rings.* Phys. Rev. B **76**, 235404 (2007).

[Reu00] K. Reuter, P. de Andres, F. Garcia-Vidal, D. Sestovic, F. Flores, and K. Heinz. *Green's function calculation of Ballistic Electron Emission Microscopy currents (BEEM v2.1).* Comp. Phys. Commun. **127**, 327 (2000).

[Rob08] J. P. Robinson, H. Schomerus, L. Oroszlány, and V. I. Fal'ko. *Adsorbate-Limited Conductivity of Graphene.* Phys. Rev. Lett. **101**, 196803 (2008).

[Roc06] A. R. Rocha, V. M. García-Suárez, S. Bailey, C. Lambert, J. Ferrer, and S. Sanvito. *Spin and molecular electronics in atomically generated orbital landscapes.* Phys. Rev. B **73**, 085414 (2006).

[Rom12] I. Romanovsky, C. Yannouleas, and U. Landman. *Patterns of the Aharonov-Bohm oscillations in graphene nanorings.* Phys. Rev. B **85**, 165434 (2012).

[Run08] I. Rungger and S. Sanvito. *Algorithm for the construction of self-energies for electronic transport calculations based on singularity elimination and singular value decomposition.* Phys. Rev. B **78**, 035407 (2008).

[Rus08] S. Russo, J. B. Oostinga, D. Wehenkel, H. B. Heersche, S. S. Sobhani, L. M. K. Vandersypen, and A. F. Morpurgo. *Observation of Aharonov-Bohm conductance oscillations in a graphene ring.* Phys. Rev. B **77**, 085413 (2008).

[Ryc07] A. Rycerz, J. Tworzydlo, and C. W. J. Beenakker. *Valley filter and valley valve in graphene.* Nat. Phys. **3**, 172 (2007).

[Ryc09] A. Rycerz. *Aharonov-Bohm Effect and Valley Polarization in Nanoscopic Graphene Rings.* Acta Phys. Pol. A **115**, 322 (2009).

[Ryc10] A. Rycerz. *Magnetoconductance of the Corbino disk in graphene.* Phys. Rev. B **81**, 121404 (2010).

[Ryu07] S. Ryu, C. Mudry, A. Furusaki, and A. W. W. Ludwig. *Landauer conductance and twisted boundary conditions for Dirac fermions in two space dimensions.* Phys. Rev. B **75**, 205344 (2007).

[Sai98] R. Saito, G. Dresselhaus, and S. Dresselhaus. *Physical Properties of Carbon Nanotubes.* Imperial College Press (1998).

[Sai00] R. Saito, G. Dresselhaus, and M. S. Dresselhaus. *Trigonal warping effect of carbon nanotubes.* Phys. Rev. B **61**, 2981 (2000).

[San99] S. Sanvito, C. J. Lambert, J. H. Jefferson, and A. M. Bratkovsky. *General Green's-function formalism for transport calculations with* spd *Hamiltonians and giant magnetoresistance in Co- and Ni-based magnetic multilayers.* Phys. Rev. B **59**, 11936 (1999).

[Sas06] K. Sasaki, S. Murakami, and R. Saito. *Stabilization mechanism of edge states in graphene.* Appl. Phys. Lett. **88**, 113110 (2006).

[Sch61] J. Schwinger. *Brownian Motion of a Quantum Oscillator.* J. Math. Phys. **2**, 407 (1961).

[Sch06] F. Schwabl. *Statistische Mechanik.* Springer (2006).

[Sch08] F. Schwabl. *Advanced quantum mechanics.* Springer (2008).

[Sch09] A. Schuessler, P. M. Ostrovsky, I. V. Gornyi, and A. D. Mirlin. *Analytic theory of ballistic transport in disordered graphene.* Phys. Rev. B **79**, 075405 (2009).

[Sch10a] J. Schelter, D. Bohr, and B. Trauzettel. *Interplay of the Aharonov-Bohm effect and Klein tunneling in graphene.* Phys. Rev. B **81**, 195441 (2010).

[Sch10b] A. Schuessler, P. M. Ostrovsky, I. V. Gornyi, and A. D. Mirlin. *Full counting statistics in disordered graphene at the Dirac point: From ballistics to diffusion.* Phys. Rev. B **82**, 085419 (2010).

[Sch11] J. Schelter, P. M. Ostrovsky, I. V. Gornyi, B. Trauzettel, and M. Titov. *Color-Dependent Conductance of Graphene with Adatoms.* Phys. Rev. Lett. **106**, 166806 (2011).

[Sch12a] J. Schelter, P. Recher, and B. Trauzettel. *The Aharonov–Bohm effect in graphene rings.* Solid State Commun. (2012). doi:10.1016/j.ssc.2012.04.039.

[Sch12b] J. Schelter, B. Trauzettel, and P. Recher. *How to Distinguish between Specular and Retroconfigurations for Andreev Reflection in Graphene Rings.* Phys. Rev. Lett. **108**, 106603 (2012).

[Sch12c] C. Schönenberger. *Bandstructure of Graphene and Carbon Nanotubes: An Exercise in Condensed Matter Physics* (2000; URL last accessed: May 3, 2012). URL www.nanoelectronics.ch/education/Nanotubes/LCAO-NT.pdf

[She08] T. Shen, Y. Q. Wu, M. A. Capano, L. P. Rokhinson, L. W. Engel, and P. D. Ye. *Magnetoconductance oscillations in graphene antidot arrays.* Appl. Phys. Lett. **93**, 122102 (2008).

[She12] K. G. Shenoy. *The derivation of Sylvester's Determinant Theorem* (2011; URL last accessed: May 03, 2012). URL www.ee.iitb.ac.in/spann/sylvester.pdf

[Sho98] N. H. Shon and T. Ando. *Quantum Transport in Two-Dimensional Graphite System.* J. Phys. Soc. Jpn. **67**, 2421 (1998).

[Shy09] A. V. Shytov, D. A. Abanin, and L. S. Levitov. *Long-Range Interaction between Adatoms in Graphene.* Phys. Rev. Lett. **103**, 016806 (2009).

[Smi12] D. Smirnov, H. Schmidt, and R. J. Haug. *Aharonov-Bohm effect in an electron-hole graphene ring system* (2012). arXiv:1204.6281.

[Sta07] T. Stauber, N. M. R. Peres, and F. Guinea. *Electronic transport in graphene: A semiclassical approach including midgap states.* Phys. Rev. B **76**, 205423 (2007).

[Sta09] N. Stander, B. Huard, and D. Goldhaber-Gordon. *Evidence for Klein Tunneling in Graphene p-n Junctions.* Phys. Rev. Lett. **102**, 026807 (2009).

[Sto88] S. D. Stone and A. Szafer. *What is measured when you measure a resistance?—The Landauer formula revisited.* IBM J. Res. Dev. **32**, 384 (1988).

[Tan07] Y.-W. Tan, Y. Zhang, H. L. Stormer, and P. Kim. *Temperature dependent electron transport in graphene.* Eur. Phys. J. – Spec. Top. **148**, 15 (2007).

[Tho81] D. J. Thouless and S. Kirkpatrick. *Conductivity of the disordered linear chain.* J. Phys. C **14**, 235 (1981).

[Tit07a] M. Titov. *Impurity-assisted tunneling in graphene.* Eur. Phys. Lett. **79**, 17004 (2007).

[Tit07b] M. Titov, A. Ossipov, and C. W. J. Beenakker. *Excitation gap of a graphene channel with superconducting boundaries.* Phys. Rev. B **75**, 045417 (2007).

[Tit10] M. Titov, P. M. Ostrovsky, I. V. Gornyi, A. Schuessler, and A. D. Mirlin. *Charge Transport in Graphene with Resonant Scatterers.* Phys. Rev. Lett. **104**, 076802 (2010).

[Tod94] T. N. Todorov and G. A. D. Briggs. *Effects of compositional impurities and width variation on the conductance of a quantum wire.* J. Phys.: Cond. Mat. **6**, 2559 (1994).

[Tol10] J. R. Toland and C. P. Search. *Electron Sagnac gyroscope in an array of mesoscopic quantum rings.* Phys. Lett. A **374**, 923 (2010).

[Tra07] B. Trauzettel, D. V. Bulaev, D. Loss, and G. Burkard. *Spin qubits in graphene quantum dots.* Nat. Phys. **3**, 192 (2007).

[Two06] J. Tworzydło, B. Trauzettel, M. Titov, A. Rycerz, and C. W. J. Beenakker. *Sub-Poissonian Shot Noise in Graphene.* Phys. Rev. Lett. **96**, 246802 (2006).

[Wal47] P. R. Wallace. *The Band Theory of Graphite.* Phys. Rev. **71**, 622 (1947).

[Was86] S. Washburn and R. A. Webb. *Aharonov-Bohm effect in normal metal quantum coherence and transport.* Adv. Phys. **35**, 375 (1986).

[Was87] S. Washburn, H. Schmid, D. Kern, and R. A. Webb. *Normal-metal Aharonov-Bohm effect in the presence of a transverse electric field.* Phys. Rev. Lett. **59**, 1791 (1987).

[Web85] R. A. Webb, S. Washburn, C. P. Umbach, and R. B. Laibowitz. *Observation of h/e Aharonov-Bohm Oscillations in Normal-Metal Rings.* Phys. Rev. Lett. **54**, 2696 (1985).

[Weh09] T. O. Wehling, M. I. Katsnelson, and A. I. Lichtenstein. *Impurities on graphene: Midgap states and migration barriers.* Phys. Rev. B **80**, 085428 (2009).

[Weh10] T. O. Wehling, S. Yuan, A. I. Lichtenstein, A. K. Geim, and M. I. Katsnelson. *Resonant Scattering by Realistic Impurities in Graphene.* Phys. Rev. Lett. **105**, 056802 (2010).

[Wen08] L. Weng, L. Zhang, Y. P. Chen, and L. P. Rokhinson. *Atomic force microscope local oxidation nanolithography of graphene.* Appl. Phys. Lett. **93**, 093107 (2008).

[Wic50] G. C. Wick. *The Evaluation of the Collision Matrix.* Phys. Rev. **80**, 268 (1950).

[Wim09a] M. Wimmer. *Quantum transport in nanostructures: From computational concepts to spintronics in graphene and magnetic tunnel junctions.* Ph.D. thesis, Regensburg (2009).

[Wim09b] M. Wimmer and K. Richter. *Optimal block-tridiagonalization of matrices for coherent charge transport.* J. Comp. Phys. **228**, 8548 (2009).

[Wit10] C. S. Withers and S. Nadarajah. *log det A = tr log A.* Int. J. Math. Edu. Sci. Tech. **41**, 1121 (2010).

[Wu10] Z. Wu, Z. Z. Zhang, K. Chang, and F. M. Peeters. *Quantum tunneling through graphene nanorings.* Nanotech. **21**, 185201 (2010).

[Wur10] J. Wurm, M. Wimmer, H. U. Baranger, and K. Richter. *Graphene rings in magnetic fields: Aharonov–Bohm effect and valley splitting.* Semicond. Sci. Tech. **25**, 034003 (2010).

[Xu08] H. Xu, T. Heinzel, M. Evaldsson, and I. V. Zozoulenko. *Magnetic barriers in graphene nanoribbons: Theoretical study of transport properties.* Phys. Rev. B **77**, 245401 (2008).

[Xu12] N. Xu, J. Ding, B. Wang, D. Shi, and H. Sun. *Transport properties of mesoscopic graphene rings.* Physica B **407**, 335 (2012).

[Yan10] C.-H. Yan and L.-F. Wei. *Size effects in Aharonov–Bohm graphene rings.* J. Phys.: Cond. Mat. **22**, 295503 (2010).

[Yoo10] J. S. Yoo, Y. W. Park, V. Skakalova, and S. Roth. *Shubnikov–de Haas and Aharonov Bohm effects in a graphene nanoring structure.* Appl. Phys. Lett. **96**, 143112 (2010).

[You09] A. F. Young and P. Kim. *Quantum interference and Klein tunnelling in graphene heterojunctions.* Nat. Phys. **5**, 222 (2009).

[Yua10] S. Yuan, H. De Raedt, and M. I. Katsnelson. *Modeling electronic structure and transport properties of graphene with resonant scattering centers.* Phys. Rev. B **82**, 115448 (2010).

[Zar09] M. Zarenia, J. M. Pereira, F. M. Peeters, and G. A. Farias. *Electrostatically Confined Quantum Rings in Bilayer Graphene.* Nano Lett. **9**, 4088 (2009).

[Zar10a] M. Zarenia, J. M. Pereira, A. Chaves, F. M. Peeters, and G. A. Farias. *Erratum: Simplified model for the energy levels of quantum rings in single layer and bilayer graphene [Phys. Rev. B 81, 045431 (2010)].* Phys. Rev. B **82**, 119906 (2010).

[Zar10b] M. Zarenia, J. M. Pereira, A. Chaves, F. M. Peeters, and G. A. Farias. *Simplified model for the energy levels of quantum rings in single layer and bilayer graphene.* Phys. Rev. B **81**, 045431 (2010).

[Zha05] Y. Zhang, Y.-W. Tan, H. L. Stormer, and P. Kim. *Experimental observation of the quantum Hall effect and Berry's phase in graphene.* Nature **438**, 201 (2005).

Acknowledgments / Danksagung

This thesis and the work presented herein, which is the result of several years of research, development, and intellectual exchange and discussions, could not have been realized without the help and support from a number of friends and colleagues, to whom I like to express my most sincere gratitude. I first want to thank all past and present members of our group TP4; it has been nice to watch this group, which initially started as "AG Mesoskopische Physik" with only three members, grow over the years by the addition of a bunch of colleagues with exceptional professional as well as social skills, the latter especially crystallizing in—but not being restricted to—the numerous birthday & PRL cake, evening project, and barbecue events, which became a tradition over the years, as well as the overall warm, friendly, and cooperative atmosphere, which is the foundation of a productive working environment. In particular, I want to thank Dietrich, Rolf, and our former group member Moritz Lenz for a number of fruitful discussions about numerics, as well as Jan, from whose strong analytical skills and comprehensive understanding for the world of physics I had the opportunity to benefit a lot. It is also quite satisfying to know that the work on the numerical toolkit developed over the past years is taken over and pursued further by Hans, who shows a quick grasp for the underlying concepts. I also want to thank Patrik, not only for guiding me through our joint work on the "Andreev ring", but also for always having an open door and taking the time for discussions, allowing me to benefit from his experience. Very cordial thanks I want to express to Nelly, for always taking great care of the group in her pleasant, provident style, and for keeping things running smoothly.

People I owe a debt of gratitude not only include members of our group. "Non-local" thanks go to Dan Bohr, who originally introduced me to the basics of the numerical method used in this work, provided and explained to me his implementation of the method I subsequently extended, and thus made a significant contribution to this work, not only to our joint project on the "Klein ring". I also thank Michael Wimmer, who is an expert (not only) on this numerical method and its application to graphene, for his advice and expertise on multiple occasions. I was also very fortunate having been able to work together with Mikhail "Misha" Titov and his colleagues Pavel "Pasha" Ostrovsky and Igor Gornyi; our most enjoyable joint work on the color-dependent conductance allowed me to learn a new powerful analytical method from the experts on the field, which not only formed the basis of our joint publication but also nicely complements the assembly of this thesis. Pasha and Misha, whom I bombarded with an extensive number of questions on the matter, both showed great patience in answering them.

The person from my scientific environment I am most deeply indebted to is my advisor Prof.Dr. Björn Trauzettel, who encouraged me to put into practice and further develop my interests and skills in a highly interesting scientific field of strong dynamics and relevance. With his remarkably deliberate, patient, and balanced style of guidance, he controlled and kept track of my progress in various projects while also giving me the freedom and motivating

me to autonomously bring in, develop, and pursue my own ideas. Besides practicing a "politics of open doors", thus always taking the time for discussions and providing helpful suggestions, he provided me with opportunities for attending and participating in various schools and conferences as well as scientific exchange on a number of visits, and he helped me developing my skills in various directions, for instance by entrusting me with responsibilities such as the coaching of diploma and bachelor students or by providing me insights into the work as a referee.

Ein wesentliches Element auf dem langwierigen und oftmals anstrengenden Weg zur Fertigstellung einer wissenschaftlichen Arbeit ist zudem die Unterstützung aus dem familiären Umfeld, zu dem ich nicht nur meine Eltern, Geschwister und Tanja, sondern auch Karl, Sieglinde und Simone zähle, denen ich für ihren Rückhalt und ihren Zuspruch sehr dankbar bin. Ein besonderer Dank gilt hierbei meinen Eltern Harald und Regina, die die Grundlagen für den Weg gelegt haben, den ich gegangen bin, sowie Tanja, die mich während der letzten Jahre stets anspornte und mir ein unerschöpfliches Maß an Geduld entgegenbrachte.

List of publications

The following articles have appeared in peer-reviewed journals:

1. Jörg Schelter, Patrik Recher, and Björn Trauzettel.
   The Aharonov–Bohm effect in graphene rings.
   Solid State Commun. (2012), doi:10.1016/j.ssc.2012.04.039.

2. Jörg Schelter, Björn Trauzettel, and Patrik Recher.
   How to distinguish between specular and retroconfigurations for Andreev reflection in graphene rings.
   Phys. Rev. Lett. **108**, 106603 (2012).

3. Jörg Schelter, Pavel Ostrovsky, Igor Gornyi, Björn Trauzettel, and Mikhail Titov.
   Color-dependent conductance of graphene with adatoms.
   Phys. Rev. Lett. **106**, 166806 (2011).

4. Jörg Schelter, Dan Bohr, and Björn Trauzettel.
   Interplay of the Aharonov–Bohm effect and Klein tunneling in graphene.
   Phys. Rev. B **81**, 195441 (2010).

5. Johannes Fuchs, Jörg Schelter, Francesco Ginelli, and Haye Hinrichsen.
   Local persistence in the directed percolation universality class.
   J. Stat. Mech.: Theor. Exp. P04015 (2008).

Erklärung

Die vorliegende Dissertation wurde am Lehrstuhl für Theoretische Physik IV am Institut für Theoretische Physik und Astrophysik der Fakultät für Physik und Astronomie an der Bayerischen Julius-Maximilians-Universität Würzburg angefertigt und von Prof. Dr. Björn Trauzettel betreut. Hiermit versichere ich, Jörg Alexander Jürgen Schelter, geboren am 6. Oktober 1981 in Fürth, an Eides statt, dass ich die vorliegende Dissertation eigenständig, d. h. insbesondere selbstständig und ohne Hilfe eines kommerziellen Promotionsberaters angefertigt und keine anderen als die angegebenen Quellen und Hilfsmittel benutzt habe. Ich erkläre außerdem, dass die vorliegende Dissertation weder in gleicher noch in anderer Form in einem anderen Prüfungsfach vorgelegen hat, und dass ich außer den mit dem Zulassungsgesuch urkundlich vorgelegten Graden keine weiteren akademischen Grade erworben oder zu erwerben versucht habe.

Würzburg, den . . . .

. . . .
(Jörg Schelter)